学位論文

X-ray timing spectroscopy of narrow line Seyfert I galaxies with *NuSTAR*

(*NuSTAR* を用いた狭輝線 I 型セイファート銀河の X 線スペクトル変動)

平成 29 年 12 月博士 (理学) 申請

東京大学大学院理学系研究科

物理学専攻

三宅 克馬

Abstract

An active galactic nucleus (AGN), which is a supermassive black hole at the center of a galaxy, efficiently convert gravitational energy of accreting materials into emission. The materials first form an accretion disk which emits optical and ultraviolet photons, then turn into hot plasma flow called a corona, and finally swallowed into the black hole. The photons from the disk are Compton scattered by the corona, to form primary X-ray continuum from $\lesssim$ 1 keV to $\gtrsim$ 100 keV. However, these X-ray spectra of AGNs are relatively featureless, so that it was difficult to separate the primary component from various secondary X-ray components, which are produced when the primary X-rays are reprocessed by surrounding materials.

To overcome this difficulty, Noda (2013) and Noda et al. (2011a, 2013b, 2014) developed a novel method of variability-assisted spectral decomposition, and discovered that X-ray spectra of Type-I Seyfert AGNs (Seyfert 1s) consist of two distinct primary components. One is softer with a photon index $\Gamma \sim 2.2$, and the other is harder with $\Gamma \sim 1.5$. In addition, they proposed that the hot corona producing the harder primary is an radiatively inefficient accretion flow (RIAF) which may form inside the accretion disk. However, the source of the softer primary still has remained a mystery.

In the present thesis, our target is another class of AGNs, narrow line Seyfert I galaxies (NLS1s), which have higher accretion rates, possibly lower black-hole masses, and narrower optical Hβ lines than Seyfert 1s. Because NLS1s have softer X-ray spectra, their X-rays can be used for probing the soft primary. Our purposes are to confirm that the Noda's paradigm is also applicable to NLS1s, to identify the emitting region of the soft primary, to strengthen the Noda's suggestion that the softer primary becomes more dominating toward higher accretion rate, and to examine why NLS1s has the narrow optical lines based on X-ray knowledge. Because wide-band spectra are required to separate different spectral components (i.e., the two primaries and the reprocessed ones), we used public data obtained with the *NuSTAR* (covering the 3–79 keV band) and *Suzaku* (0.5–45 keV) satellites. We selected 11 (*NuSTAR*) and 4 (*Suzaku*) observations with high statistics and variability of four NLS1s, Swift J2127.4+5654, Mrk 766, Ark 564, and NGC 4051.

Mainly using the difference spectrum method, we successfully decomposed the X-ray spectra into variable and stationary components. In two less-luminous NLS1s, Swift J2127.4+5654 and NGC 4051, it was discovered that their spectra also consist of a softer PL with $\Gamma \sim 2.2$,

a harder PL with $\Gamma \sim 1.5$, and their reflection. The soft PL mainly carried their intensity variations, while the hard PL is less variable. These results are consistent with those obtained from Seyfert 1s, confirmed by Noda (2013) and Noda et al. (2011a, 2013b, 2014). The consistency suggests that NLS1s are not extremely different from Seyfert 1s.

In the other two NLS1s with higher accretion rates, Mrk 766 and Ark 564, their spectra can be explained by a model consisting of a softer PL and its reflection. The harder PL is not required and the upper limit on the hard PL flux was obtained.

By comparing the present results from those on Seyfert 1s, it has become clear that the flux carried by the softer primary increases progressively toward higher accretion rate, whereas that of harder primary saturate, and cannot exceed luminosity ratio $\eta = 0.03$–0.1 to the Eddington value. This is explained by considering that the hard PL is generated in the RIAF region inside the accretion disk, and the inner radius of the disk becomes smaller at high η. This result quantitatively confirms the suggestion by Noda et al. (2014).

Interesting differences were found in the properties of the reflection component between the low-accretion-rate NLS1s and those with higher rate. In the former two objects, the reflection component did not vary, and the associated Fe-K line was narrow. In the latter two sources, the Fe-K line was broadened, and the reflection continuum varied at least in Mrk 766. These are considered to be because the disk edge extends inside when the source is bright, and the reprocessing region becomes smaller. These results further support the RIAF picture of the hard primary.

The corona emitting the soft primary is suggested to be located upstream to that emitting the hard primary. As a result, the soft primary source is considered to be a patchy corona on the accretion disk.

The results obtained so far also allow us to answer the origin of the defining property of NLS1s in the optical; the optical emission lines from their broad line region (BLR) is less broadened than those in Seyfert 1s. NLS1s generally have a higher accretion rate, and hence are dominated by the soft primary, which is more efficiently generated from accreting mass than the hard primary. If materials in the BLR also accretes to the black hole, they are exposed to stronger irradiation in such an efficient system. As a result, the BLR goes away from the black hole, and the emission line from the ionized gas becomes narrower because of its slow Keplerian velocity.

By the analyses of the NLS1s, we reinforced and improved the new AGN paradigm by Noda (2013) and Noda et al. (2011a, 2013b, 2014). In addition, we successfully obtained the explanation of the optical property of NLS1s.

Contents

List of Figures

List of Tables

Chapter 1

INTRODUCTION

Almost all galaxies are considered to harbor, at their centers, a supermassive black hole (SMBH) with a mass of $10^{6-10} M_{\odot}$, where $M_{\odot}$ is the solar mass. When materials accrete onto a SMBH, they release their gravitational energies and emit photons from the close vicinity of the SMBH with luminosities of 10^{43-47} erg s^{-1}. These bright cores of galaxies are called active galactic nuclei (AGNs). The material accreting onto an AGN, fist forming a dusty torus and then an accretion disk, is considered to be gradually heated, and finally become a bright X-ray source, as confirmed over the past 4 decades. With X-rays, we can hence probe "AGN central engines" which converts the gravitational energy with high efficiency into radiation. So far, many X-ray satellites were launched to observe such emission from AGNs and other objects, including Japanese ones, *Temma* (1983), *Ginga* (1987), *ASCA* (1993), *Suzaku* (2007), and *Hitomi* (2016).

Figure 1.1 shows a typical X-ray spectral model of an AGN together with a schematic view of its central engine. The primary X-ray radiation from an AGN is thus considered to arise via inverse Compton scattering, in which photons are up-scattered to higher energies by a hot electron cloud (corona) with temperature of $\sim 10^8$ K (Haardt et al. 1994). The produced component is power law (PL) shaped with a photon index $\Gamma \sim 2$, and produce X-ray continuum in energies typically from ~ 1 keV to ~ 100 keV. A fraction of the primary radiation is reprocessed by surrounding materials via combination of photo-absorption and Compton down-scattering (George & Fabian 1991), to form several secondary components. One of them is "distant" reflection component which consists of a continuum, Fe K lines, and an Fe K edge. Another secondary emission is "relativistic" reflection, formed by these primary photons which are reflected by materials located near the SMBH, in which the Fe-K line at 6.4 keV is broadened by relativistic effects and extends from ~ 4 keV to ~ 7 keV. Apart from these genuine secondary components, a part of the primary PL photons experi-

ence strong absorption by surrounding materials, and produce a highly absorbed subsidiary continuum with an Fe-K edge; this condition is called partial covering absorption (Holt et al. 1980).

Although X-ray spectra from AGNs are considered to be a superposition of a few different components, they are relatively featureless except the Fe lines and edges. As a result, it has been difficult to unambiguously distinguish the primary continuum from the secondary components without any assumption. In fact, the same spectrum can be explained by different models with different physical implications (Cerruti et al. 2011). This kind of "model degeneracy" manifest itself most clearly how to explain the positive excess signals that appear at 6–7 keV and $\gtrsim$ 20 keV of a spectrum above the $\Gamma \sim 2$ PL (figure 1.1). One popular interpretation (e.g. Nandra et al. 2007) regards this excess entirely as a secondary component, and attributes it to the relativistic reflection process. Another widely discussed view (e.g. Miyakawa et al. 2009) assumes that the excess is due to the partial covering absorption of the $\Gamma \sim 2$ primary. Yet a third view, proposed by Noda et al. (2011a), attributes the excess features to an additional new primary component, which is very hard and heavily absorbed to exhibit an Fe-K absorption edge. These three alternatives predict similar spectral shapes, but their implications are very different. We therefore need to clarify, from observational aspects, which of them is most appropriate as the unified view of the AGN central engine. In the present thesis, we adopt the third alternative among them (the softer and harder primaries) as our working hypothesis, and attempt to observationally reinforce it. In doing so, we touch also on the other two alternatives, to see whether either of them can provide better interpretations of the observational results.

To discriminate among the different spectral interpretations and hence solve the model degeneracy, timing information is useful because different components are considered to differ in their variation characteristics, including in particular the time scales. Therefore, we use variations of X-ray spectra as a clue to the central engine. To disentangle the model degeneracy, timing analyses have been performed (e.g. Taylor et al. 2003). The harder primary was discovered by using timing information, and have been identified in many AGNs by Noda (2013) and Noda et al. (2011a,b, 2013a,b, 2014). In these works, a new analysis method called "Count-Count Correlation with Positive Offset" (C3PO) method (Noda et al. 2013a) was developed in order to separate different spectral components in representative AGNs with the least amount of assumptions. By this model-independent method, they revealed for the first time that many such AGNs host two distinct primary continuum components in their X-ray spectra (Noda et al. 2011a, 2013b, 2014). Both are PL shaped, and one is softer with $\Gamma \sim 2.3$ and highly variable, while the other is harder with

$\Gamma \sim 1.4$ and less variable. The former is dominant when the source is relatively luminous, while the latter becomes dominant when the source becomes dimmer which is considered to be reflecting lower accretion rates. Essentially all previous X-ray spectral studies of AGNs have mixed up these two components, and hence all previous theoretical studies of AGNs have incorrectly assumed a single X-ray continuum with a PL of $\Gamma \sim 2.0$.

In the present thesis, we focus on a particular subclass of AGNs called narrow line Seyfert I AGNs (NLS1s). They have smaller black hole masses than more ordinary Seyfert I AGNs, which were extensively studied by Noda et al. (2011a,b, 2013a,b, 2014) with *Suzaku*, and show violent variability with large amplitude on short time scales of ~ 1 ks, because objects with lower masses show faster variability in general. We first examine whether the multiple corona view can explain spectral shapes and variations of NLS1s. If yes, we try to constrain geometrical locations of these multiple coronae, and then build a self consistent picture of the central engine. Since this high variability of NLS1 is ideal for the timing-assisted spectroscopy (including the C3PO method), these objects are expected to provide us with much better information as to the two primary continua, and enable us to constrain their origins which have remained inconclusive.

In the following Chapters, we first review basic knowledge of AGNs (§2) and the instruments used for data acquisition (§3). The observations and data reduction are described in §4. In §5 and §6, we conduct timing spectroscopy using the difference spectrum method. The obtained results are discussed in §7, to constract our view of the AGN central engine. Finally our conclusion is presented in §8.

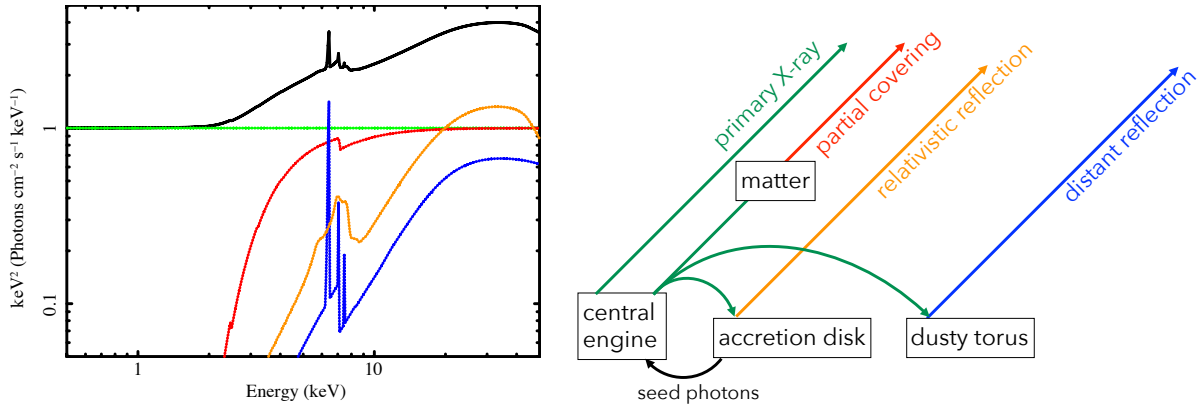

Figure 1.1: A typical X-ray spectrum of AGNs (left) and a schematic diagram of the AGN central engine (right). The colors specify individual radiation components. "The hard PL primary" is not shown here.

Chapter 2

REVIEW

2.1 Active Galactic Nuclei (AGNs)

Several percent of galaxies emit strong radiation from their extremely small central regions, and they are called active galactic nuclei (AGNs). The luminosity of an AGN, 10^{43-47} erg s^{-1}, is comparable to, or sometimes higher than the sum of those of other regions of the host galaxy, as shown in figure 2.1. AGNs usually emit in very broad electromagnetic frequencies, from radio to sometimes even TeV gamma-rays, with a surface brightness which is $\gtrsim 2$ orders of magnitude higher than those of galaxy bulges. Because of these extraordinary properties, AGNs have been attracting astrophysicists for a long time.

2.1.1 History

Although Seyfert Galaxies and quasars are representative classes of AGNs, they were discovered in different ways. Seyfert (1943) detected high-excitation optical emission lines from the central regions of some spiral galaxies. These emission lines showed high variability and were broadened to an equivalent Doppler velocities reaching several thousand km s^{-1}. Woltjer (1959) pointed out that these bright nuclei in Seyfert galaxies must be small with scales of the order of 100 pc. Assuming that the luminosity of such a nucleus were made up of an assembly of individual stars, the masses of these nuclei were estimated as $\sim 10^8 M_\odot$ from the steller mass-luminosity relation. The results mean that an extremely small and luminous core exists at the center of each Seyfert galaxy, because the typical number of stars in a 100 pc cubic region of a galaxy is $\sim 10^6$ or less.

Quasars were first identified as radio sources in the late 1950's. In the early 1960's, some of them were optically identified. Although these optical counterparts appeared point-like

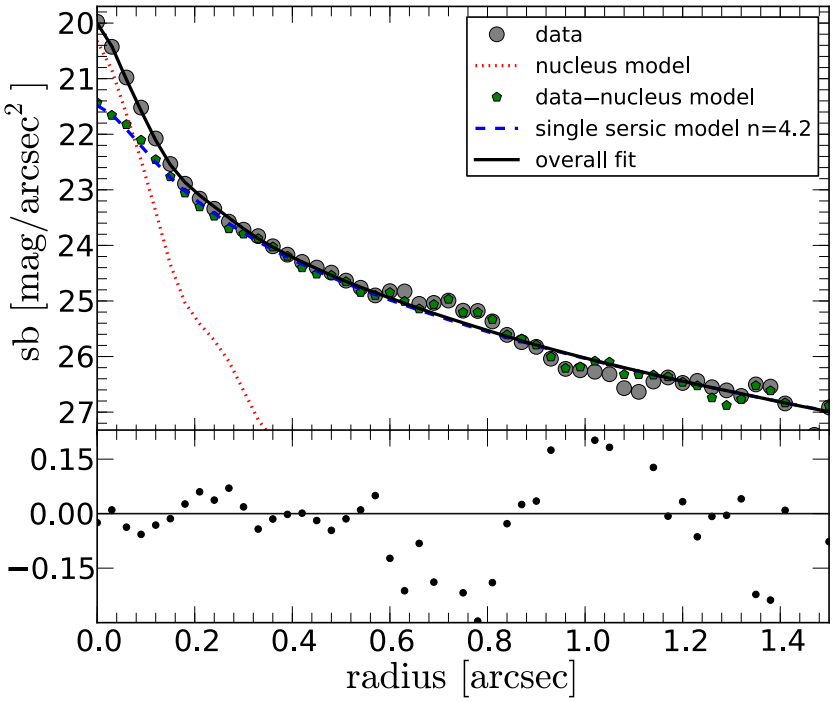

Figure 2.1: A surface brightness profile of the AGN, ID-158 (Schramm & Silverman 2013).

rather than extended, their optical spectra had broad emission lines, and were completely different from those of stars. Furthermore, the wavelengths of these emission lines were puzzling, because they did not agree with those of any optical transitions known in the laboratory. Finally, Schmidt (1963) successfully identified the emission lines in a spectrum of 3C 273 with Balmer series that are redshifted by a surprisingly (at that time) large factor, $z = 0.158$. In 1964, Hong-Yee Chiu named them "quasi-stellar radio sources", or "quasars". Later, the high redshifts of quasars became considered as due to their cosmological distances in the expanding universe.

Although quasars at first appeared as isolated point-like objects, Hutchings et al. (1984) detected faint nebulosity around many quasars. It was hence became clear that quasars are also bright nuclei of distant galaxies. In this way, Seyfert nuclei and quasars have been found to represent the same phenomenon, except that the former objects have lower redshifts (e.g., $z < 0.1$) than the latter ones ($z = 0.05$–7). These luminous cores in galaxies, including Seyfert nuclei and quasars, became collectively called "active galactic nuclei".

The energy source and the emission mechanisms of AGNs remained a big mystery. Theoretical models proposed in the 1970's to explain the AGN phenomenon included a su-

permassive star (Hoyle & Fowler 1963), a dense stellar cluster (Colgate 1967), and even matter-antimatter annihilation (Unno & Fujimoto 1974). Meantime, the presence of black holes became plausible, triggered by the discovery of rapid X-ray flaring from the Galactic X-ray source Cygnus X-1 (Oda et al. 1971). As a result, another explanation of AGNs, in terms of mass-accreting SMBH, became a new trend (e.g. Shakura & Sunyaev 1976; Lynden-Bell 1978). Finally, Rees (1984) pointed out that any dense star cluster or supermassive star inevitably becomes a black hole at the end, and proposed the famous "Rees diagram" which is cited in figure 2.2. It has become a consensus that AGNs are mass-accreting SMBH ($10^{6-9}M_{\odot}$), which convert gravitational energy into radiation, even though the formation scenario of such objects still remains a big mystery at present.

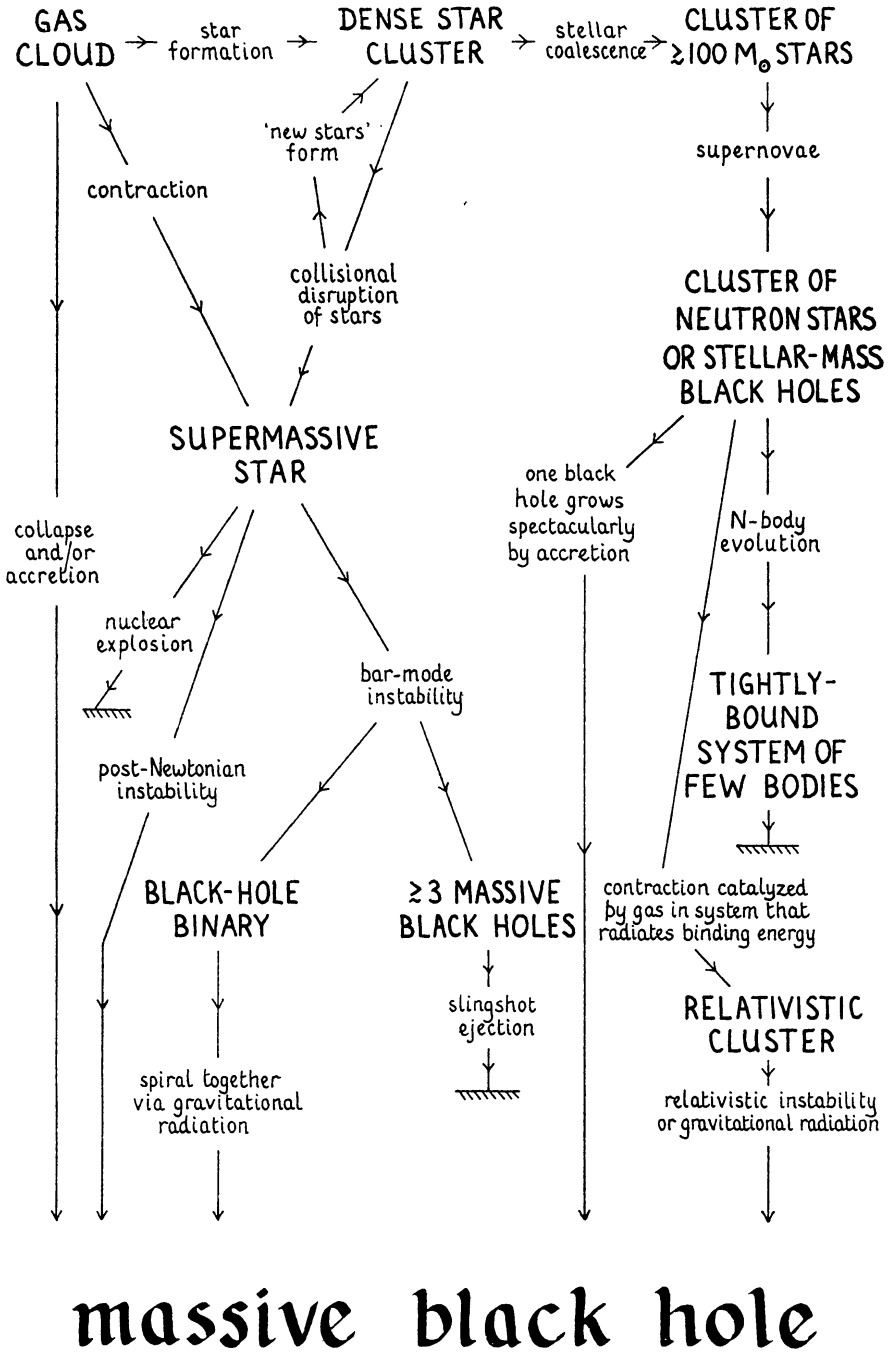

Figure 2.2: The Rees diagram which explains eventual formation of SMBHs at galactic nuclei (Rees 1984).

2.1.2 Classification

Although AGNs exhibit a wide variety of properties, they can be classified by a relatively small number of parameters, including their mass, accretion rate, and radio-loudness, as well as emission lines in their optical spectra. The product of the first two parameters is equivalent to the luminosity. Figure 2.3 shows distribution of each AGN class on the two parameters.

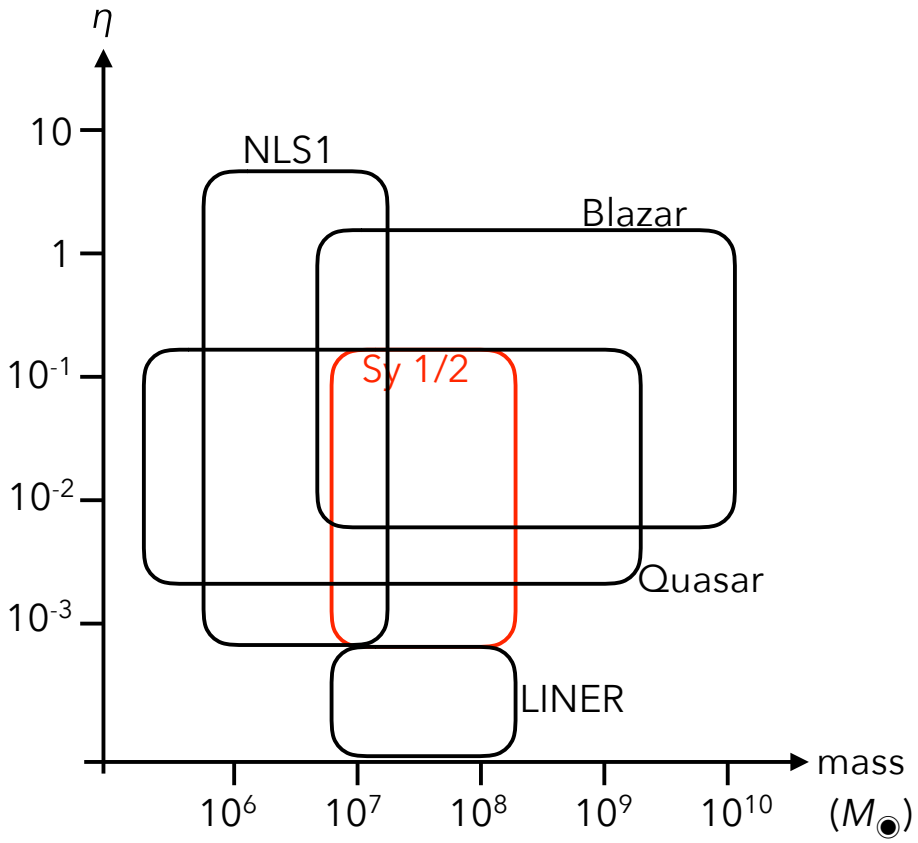

Figure 2.3: Distribution of each AGN class. The horizontal axis is the SMBH mass, and the vertical one is the accretion rate in the unit of Eddington ratio (see §2.1.6).

Seyfert galaxies

Seyfert galaxies are radio-quiet, relatively dim AGNs with X-ray luminosity of 10^{41-44} erg s^{-1}. They satisfy absolute B-magnitude of $M_{\rm B} > -21.5+5\log h_0$, where h_0 is the Hubble constant in units of 100 km s^{-1} Mpc^{-1}. Probably because of their modest luminosity, Seyfert galaxies

have mainly been discovered in our vicinity, with redshifts of $z < 0.1$. Their host galaxies are mostly spiral. The typical mass of the central SMBH is $10^{7-8} M_\odot$.

As shown in 2.4, optical spectra of Seyfert galaxies exhibit a series of high-excitation ionized emission lines. According to the profiles of these optical emission lines, Seyfert galaxies are classified into two subclasses, Type I and Type II (Khachikyan & Weedman 1971). As represented by NGC 4151 in figure 2.4, Type I Seyfert galaxies (Seyfert 1s) show both narrow ($\sim 10^2$ km s^{-1}) and broad ($\sim 10^4$ km s^{-1}) line components, whereas Type II Seyfert galaxies (Seyfert 2s) have only narrow lines as in NGC 4941. However, as presented in figure 2.5, the missing broad wing of Balmer lines and Fe II lines were discovered in a polarized spectrum of the prototypical Seyfert 2, NGC 1068 (Antonucci & Miller 1985). This discovery revealed that the emission region of broad lines, or broad line region (BLR), is also present in Seyfert 2s but is hidden from our line of sight by optically thick materials. The common presence of the narrow line components in both types of Seyferts can be understood by considering that the narrow line region (NLR) can be seen from any direction. X-ray observation of Seyfert 2s reinforced this view because their X-ray spectra taken with *Ginga* were strongly absorbed by nearly neutral materials with hydrogen column densities $N_{\rm H} \gtrsim 10^{24}$ cm^{-2} (Koyama et al. 1989, 1992; Awaki et al. 1990, 1991).

Narrow line Seyfert 1 galaxies

Narrow line Seyfert 1 galaxies (NLS1s) form a subclass of Seyfert 1. Figure 2.6 shows an optical spectrum of the NLS1, Ark 564, where the optical lines (except forbidden ones) clearly exhibit broad wings, but still not as broad as these of typical Seyfert 1's. In the most common definition of NLS1s, the width of Hβ line of Balmer series should be narrower than 2000 km s^{-1}, and O III emission lines be weak with its flux < 3 times that of Hβ (Osterbrock & Pogge 1985). NLS1s typically show strong Fe II emission lines. The origin of the smaller widths of the broad line components of NLS1s is not yet understood well.

In the *INTEGRAL* IBIS AGN catalog (Malizia et al. 2012), the number of NLS1 is 14, while that of Seyfert 1 is 73. The X-ray spectra of NLS1s in 0.5–10 keV are relatively steeper with $\Gamma \sim 2.2$ than those of Seyfert 1s often showing $\Gamma \sim 2.0$. Their X-ray intensity varies typically by a factor of 2 in ~ 100 s. The faster variability suggests that the SMBHs of NLS1s have rather low masses, typically $10^{6-7} M_\odot$. NLS1s are estimated to have high accretion rates reaching 0.3 times the Eddington limit (see §2.1.6). The high accretion rates and their small mass suggest that NLS1s are in an early stage of AGN growth (e.g. Mathur 2000).

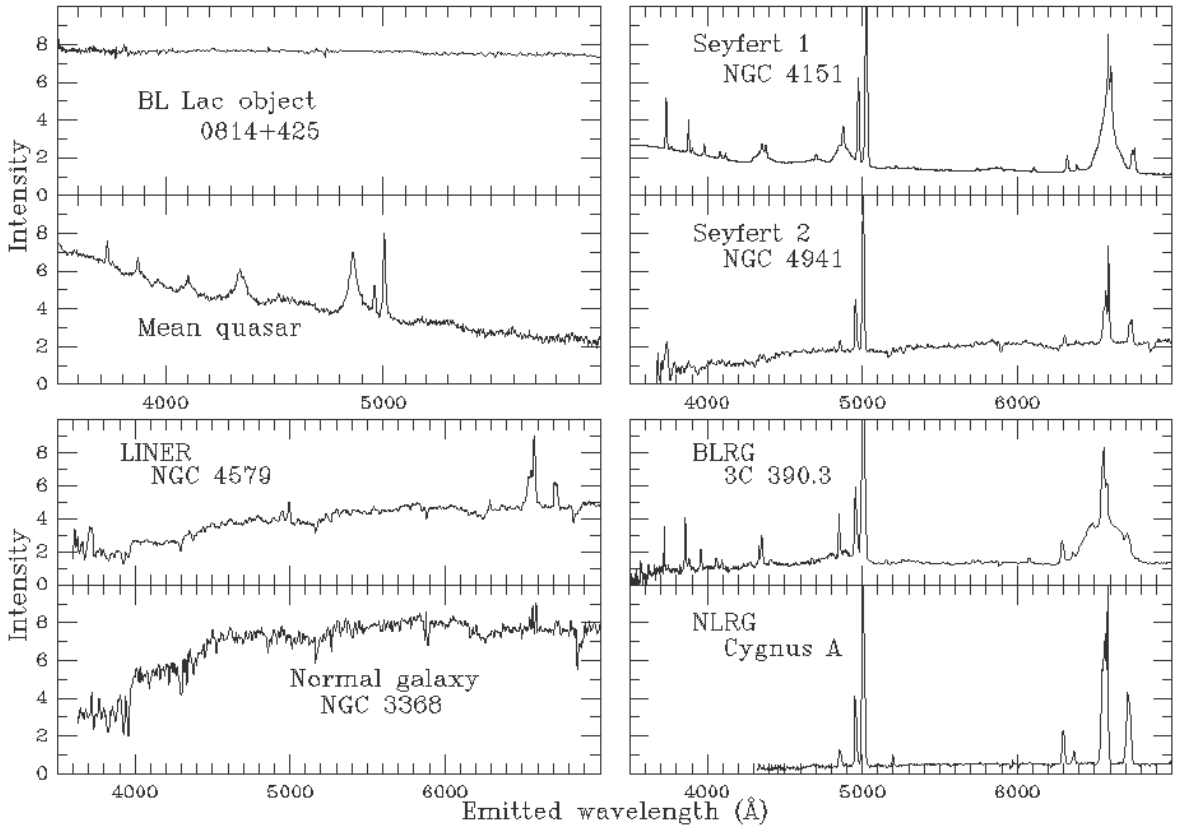

Figure 2.4: Optical spectra of various classes of AGNs, taken from the Bill Keel's slide set (URL: http://www.astr.ua.edu/keel/agn/spectra.html).

Quasars

Distributed at rather high redshifts of $z = 0.05$–7, quasars are the most luminous class of AGNs with $M_{\rm B} < -21.5 + 5 \log h_0$ and X-ray luminosities of 10^{44-48} erg s^{-1}. Strong radio emission, confirmed in 5–10% of them, mainly originates via synchrotron radiation from their radio lobes and jets. These radio-loud quasars are likely hosted in elliptical galaxies, while radio-quiet ones in spiral. Optical spectra of quasars are similar to those of Seyfert galaxies, and broad lines are relatively strong. Their intensity varies by a factor of 2–3 sometimes on a time scales of a few days.

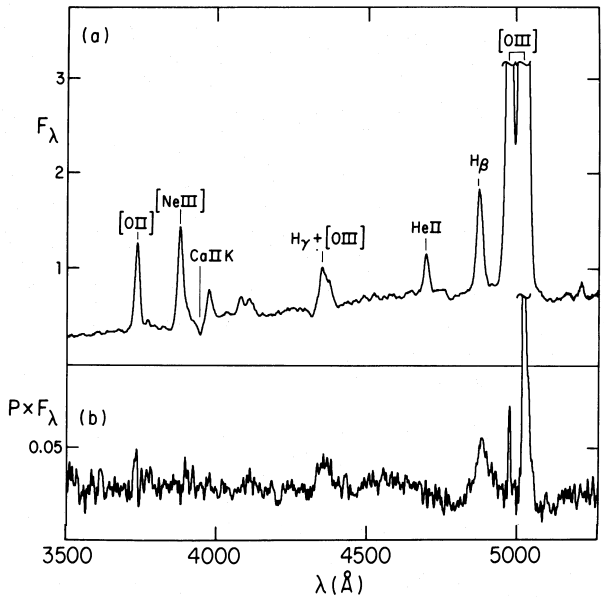

Figure 2.5: Optical spectra of NGC 1068 taken in (a) the total flux and (b) polarized flux (Antonucci & Miller 1985). The Hβ line in (b) is much broader than in (a). They are in the same arbitrary units.

Radio galaxies

Radio galaxies exhibit strong radio emission with the radio luminosity reaching 10^{46} erg s^{-1}, which is comparable to those of quasars. Most of their host galaxies are elliptical. Figure 2.7 shows a radio image of the radio galaxy, 3C 348, where we clearly observe radio lobes and a pair of jets. These jets, collimated in opposite directions, are considered to result from ejection and collimation of a small fraction of the matters accreting onto the SMBH (Begelman et al. 1984). In addition to radiation pressure and thermal energy, one of the best ways to collimate the jets is magnetic fields. When the accretion disk is threaded by magnetic field lines, an electric potential arises (Lovelace 1976). Blandford & Znajek (1977) applied it to AGNs and proposed that a high black hole spin leads to a very efficient production of such electric potentials, and hence to the jet formation.

Like Seyfert galaxies, radio galaxies are classified into two types by their appearance of broad and narrow optical emission lines. Type I radio galaxies are called broad-line radio galaxies, and Type II ones are narrow-line radio galaxies.

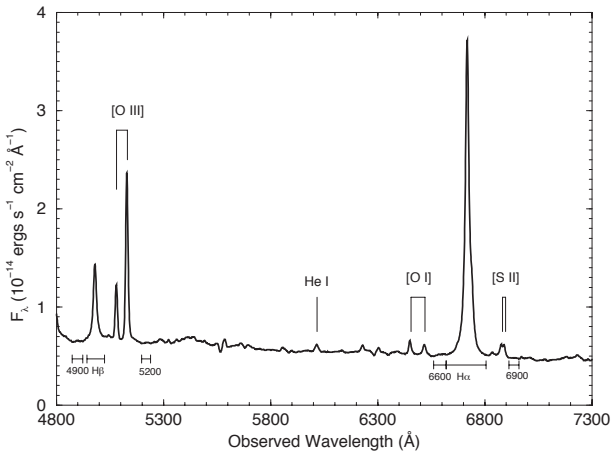

Figure 2.6: An optical spectrum of the NLS1, Ark 564 (Shemmer et al. 2001).

LINERs

Low luminosity AGNs with emission lines from low ionized gasses are called LINERs (Low-Ionization Nuclear Emission-line Regions; Heckman 1980). Their optical spectra are similar to those of Seyfert 2 except the presence of low-ionization emission lines. Compared to the spectrum of Seyfert 2, O II (3727 Å), O I (6300 Å), N II (6584 Å), and S II (6717, 6731 Å) are strong, while O III (5007 Å), Ne III (3869 Å), and He II (4686 Å) are weak. About half of spiral galaxies are reported to be LINERs.

The LINER NGC 4258 emits intense water-MASER signals from its nucleus. Utilizing the high spatial- and spectral-resolutions of the VLBI radio observation, Miyoshi et al. (1995) discovered that the emission arises from a small gas disk, which rotates, just according to the Kepler's law, around a massive object with a mass of $3.6 \times 10^7 M_\odot$. This is nothing but a SMBH. With *ASCA*, Makishima et al. (1994) discovered a strongly absorbed X-ray source, to be identified with the same SMBH, at the center of NGC 4258. The 2–10 keV luminosity was 4×10^{40} erg s^{-1} after removing absorption, and the Eddington ratio (see §2.1.6) was 1×10^{-4}. Including this and other cases (Iyomoto et al. 1998a,b), LINERs are likely to be descendants of AGNs that used to be more active in the past, and to have low luminosities because of reduced accretion rates.

BL Lac objects and Optical Violent Variables

The former objects were named after BL Lacertae, the representative example. As shown in figure 2.4, their optical spectra lack strong emission lines, either in emission or absorption.

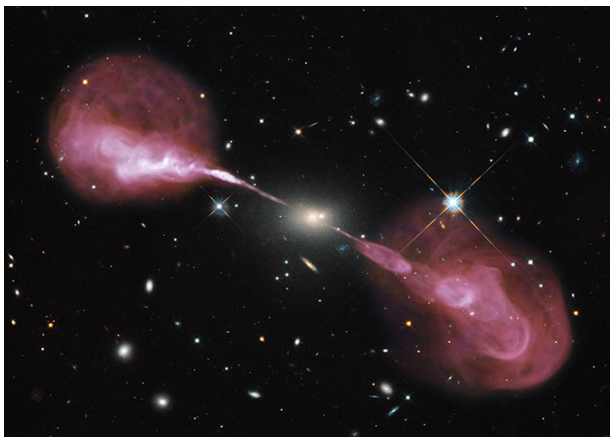

Figure 2.7: Radio (red) and optical (white and yellow) images of the radio galaxy 3C 348. Credit: NASA, ESA, S. Baum and C. O'Dea (RIT), R. Perley and W. Cotton (NRAO/AUI/NSF), and the Hubble Heritage Team (STScI/AURA)

Optical Violent Variables (OVVs) show high variability of $\sim 50\%$ in optical within a day. Their polarization also varies in both amplitude and azimuth. BL Lac objects and OVVs are considered to be AGNs that launch relativistically beamed jets along the line of sight. These two types of AGNs are collectively called blazars.

Figure 2.8 shows a broadband spectral energy distribution (SED) of the blazar, PKS 0420−01. It consists of two peaks, one at infrared (IR) and the other at gamma-rays. The former is considered as synchrotron emission by relativistic electrons in the jets, whereas the latter as inverse-Compton emission in which the synchrotron photons are boosted again by the same population of relativistic electrons (synchrotron-self-Compton process). Because of the strong continuum, blazar spectra do not exhibit any line.

2.1.3 Wide-band continuum radiation from AGNs

As schematically shown in figure 2.9, continuum radiation from AGNs without jet dominance extend from radio to gamma-rays, although not to such high energies as that of blazars (figure 2.8). The SED is flat except in radio frequencies, and can be approximated by a PL as $\nu F_\nu \propto \nu^{-(\alpha-1)}$, where the energy index α is about 0–1. In X-ray astrophysics, the photon index $\Gamma = \alpha + 1$ is conventionally used. Since the PL shape cannot be explained as thermal emission with small number of temperatures, the overall SED is likely to be a composite of multiple components that differ both in the emission region and the emission mechanism.

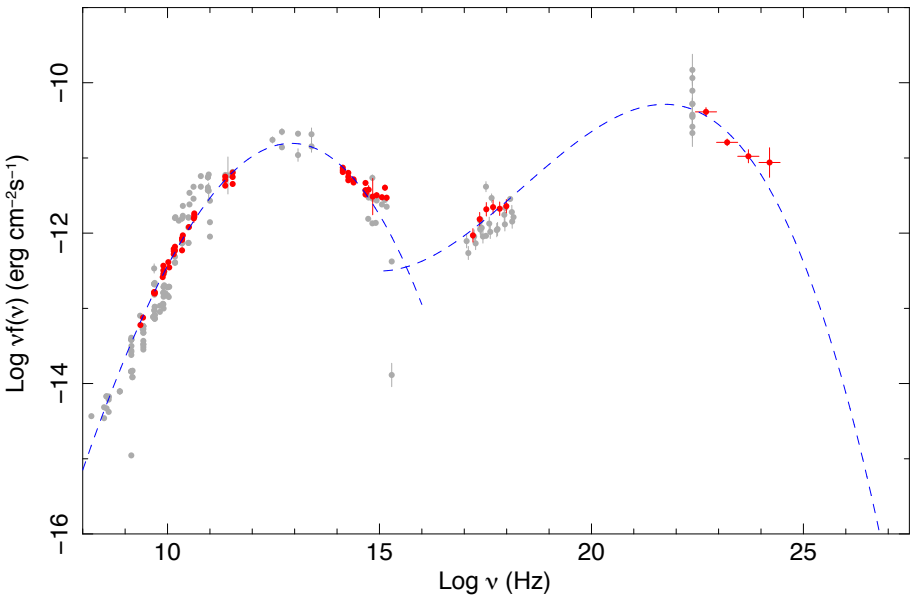

Figure 2.8: The SED of the blazar, PKS 0420-01, with the jet-related two peaks (Abdo et al. 2010).

Around 1000 Å, a bump structure, called big blue bump, is seen. This bump is considered to originate as thermal emission, especially black body emission, from an accretion disk. It is considered to extend to soft X-ray band and contribute to a soft excess in the X-ray band. Another bump around 10 μm, called IR bump, is attributed to thermal emission from warm dusts with temperature $T \lesssim 2000$ K. This bump of radio-quiet quasars falls at $\gtrsim 100$ μm, and the fall is called submillimeter break. The radio emission is considered to be synchrotron emission from jets (and lobes in some objects), with the luminosity differing by as much as 3 orders of magnitude between radio-loud and radio-quiet objects.

X-ray emission from AGNs contributes $\sim$ 10% to their bolometric luminosity (Lusso et al. 2012). Figure 2.10 shows the bolometric correction factor $f_{\rm bol}$ as a function of X-ray luminosity $L_{\rm X}$ for type I AGNs. From the observed parameters of z and the X-ray flux $F_{\rm X}$, the bolometric luminosity $L_{\rm bol}$ is calculated as

$$\begin{aligned} L_{\rm bol} &= f_{\rm bol} L_{\rm X} \\ &= f_{\rm bol}(4\pi D^2 F_{\rm X}) \\ &= 4\pi f_{\rm bol} \left(\frac{cz}{H_0}\right)^2 F_{\rm X}, \end{aligned} \tag{2.1}$$

where D, and $H_0 = 67.15$ km s^{-1} Mpc^{-1} are the comoving distance, and the Hubble con-

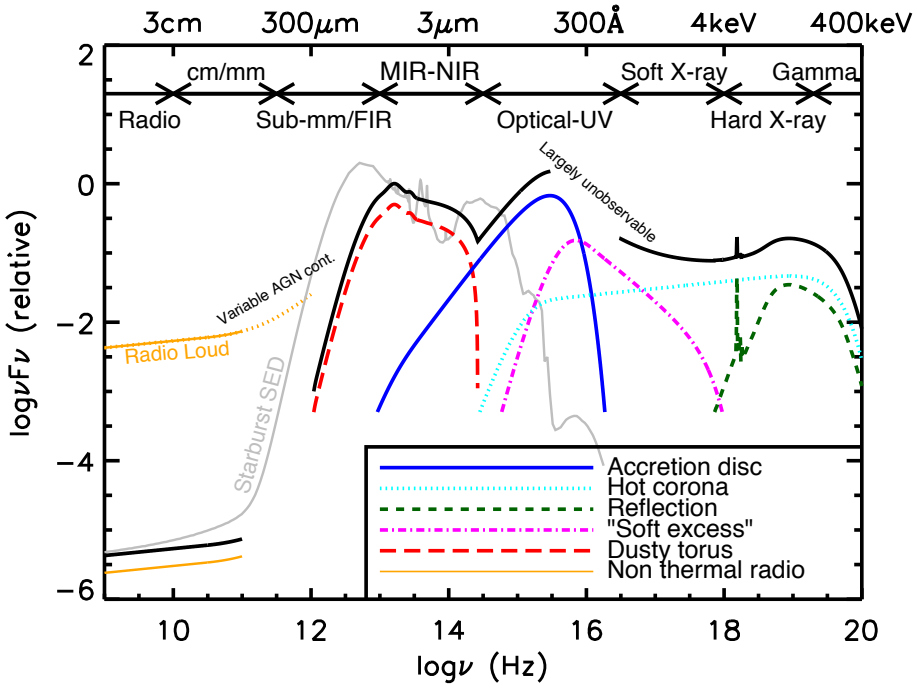

Figure 2.9: A schematic SED of an AGN that is not dominated by jet emission (Harrison 2014).

stant. The PL-shaped X-ray emission is considered to arise by inverse Compton scattering of photons from the accretion disk by a Maxellian-distributed cloud of electrons, often called corona, with a temperature of a few times of 100 keV.

2.1.4 The unified model

As explained in §2.1.2, optical spectra of AGNs exhibit strong emission lines. The narrow lines appear in the spectra of both Type I and II AGNs, while the broad lines are seen only in Type I AGNs and are hidden in Type II AGNs (§2.1.2). This fact suggests that the BLR in Type II AGNs is covered with optically thick materials. On the other hand, the NLR can be seen from any direction. From variability in each energy band and the widths of the broad ($\sim 10^4$ km s^{-1}) and narrow ($\sim 10^2$ km s^{-1}) lines, an AGN is considered to comprise a hot corona (emitting X-rays), a BLR, an accretion disk (ultraviolet and optical), a dusty torus (IR), and an NLR, in the order of increasing distance from the central SMBH. Along the rotation axis of the accreting materials, radio-emitting jets are also considered to blow out. Figure 2.11 shows a schematic configuration of these emission regions, arranged to explain

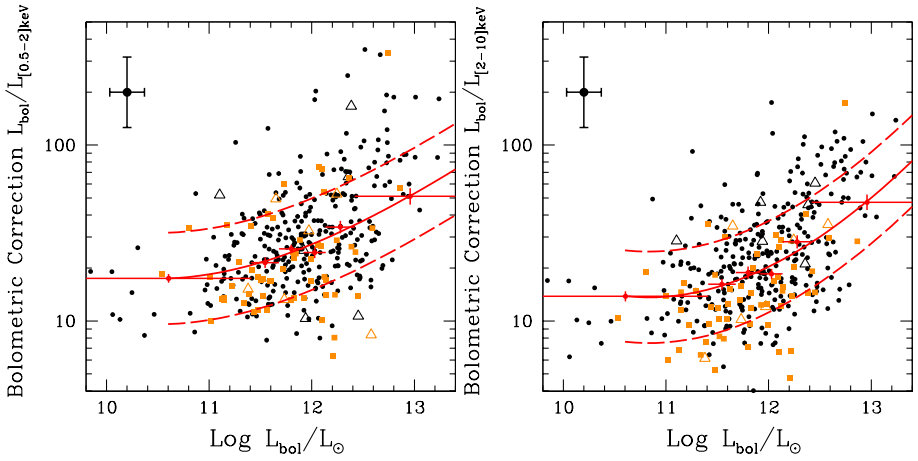

Figure 2.10: Bolometric correction factors as a function of the corrected bolometric luminosity in 0.5–2 keV (left panel) and 2–10 keV (right panel) bands for type I AGNs (Lusso et al. 2012). (black) spectro-z. (orange) photometric-z. Sources with open triangles were upper limits.

the spectral features and the variability (Antonucci 1993). This is the picture called "unified AGN model", which explains the differences between Type I and Type II AGNs in terms of viewing angles (Urry & Padovani 1995). For a typical SMBH with a mass of $10^8 M_\odot$, of which the Schwartzshild radius R_S is 3×10^{13} cm, the innermost region of the accretion disk is located at 1–30×10^{14} cm (3–$100 R_S$) from the SMBH along the equatorial plane, the BLR at 2–20×10^{16} cm (700–$7000 R_S$), and the inner radius of the torus at $\sim 10^{17}$ cm ($\sim 1000 R_S$). In the perpendicular direction, the NLR is 10^{18}–10^{20} cm (10^4–$10^6 R_S$) away from the SMBH.

Let us review recent results on the structures surrounding SMBHs. The size of the NLR can be measured using O III image. Some of AGNs show an extended NLR (ENLR), which has a conical or bi-conical shape with a size of 15–20 kpc. Because the distance of the BLR is too small to optically resolve, it has been determined by the reverberation mapping (Blandford & McKee 1982) (detail in §2.1.5). Using the high-angular-resolution VLBI imaging, the BLR in the quasar 3C 273 has been found to locate at a distance of 1000 light days, or 3×10^{17} cm (Petrov et al. 2012).

The dust torus is best studied in IR, because of the hot dust temperature of ~ 1300 K in the torus. By fitting the clumpy torus model to near-IR/mid-IR (MIR) (Alonso-Herrero et al. 2011) and ALMA data of the Seyfert 2, NGC 1068, with a mass of $8.0 \times 10^6 M_\odot$ (Lodato & Bertin 2003), the torus radius was estimated as 20^{+6}_{-10} pc ($\sim 6 \times 10^{19}$ cm) (García-Burillo et al. 2014). Furthermore, MIR interferometry revealed parsec-sized dust emission elongated

in the polar direction in five AGNs (López-Gonzaga et al. 2016). The polar dust emission is expected to constrain the torus models. Although the torus is smooth in figure 2.11, the idea of clumpy torus, which consists of many clumps of dust clouds, was proposed by Krolik & Begelman (1988). The idea has been supported by numerical simulations (Nenkova et al. 2002), and properties of silicate emission/absorption lines in their IR spectra (Roche et al. 1991).

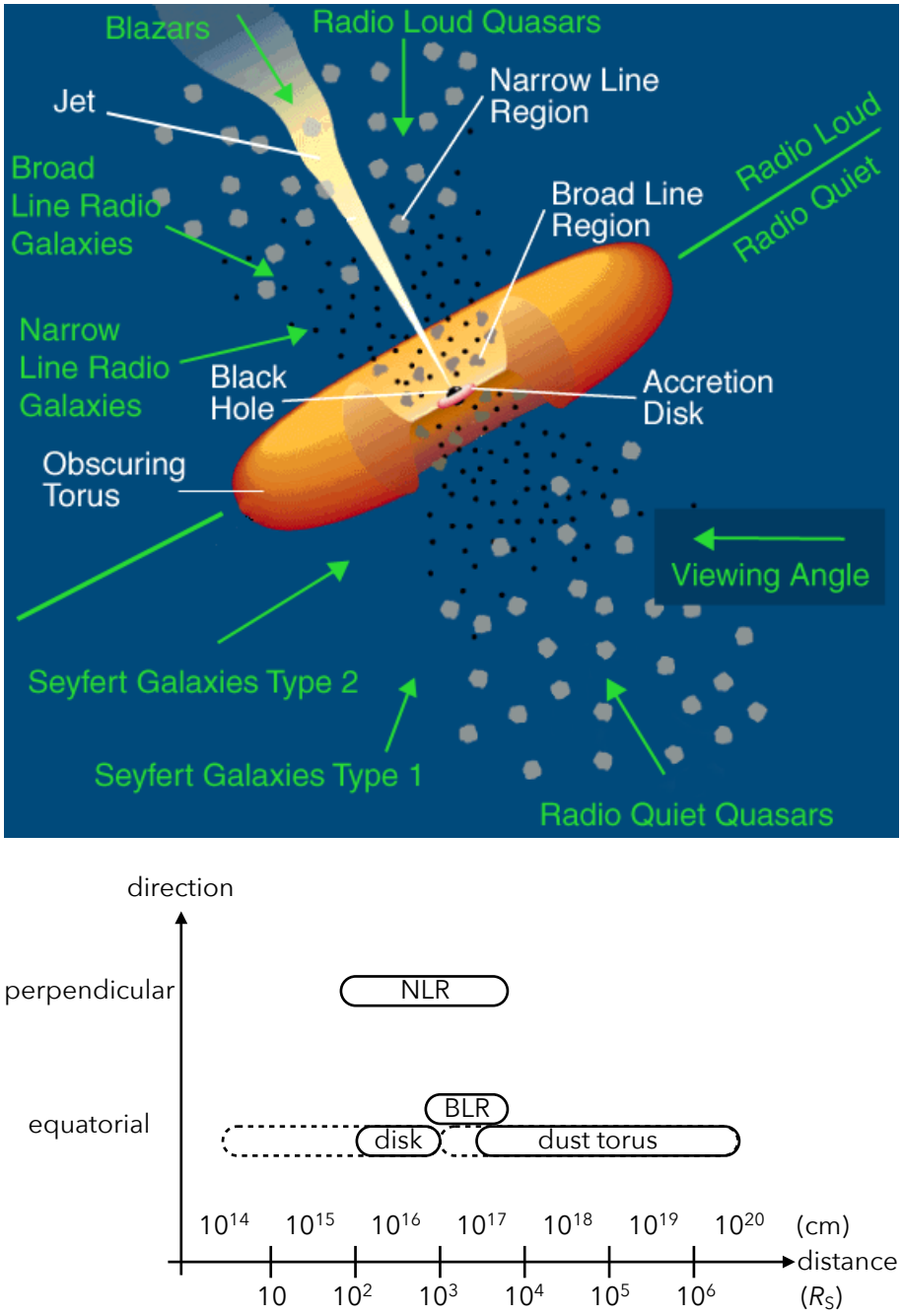

Figure 2.11: (top) A schematic diagram of the AGN unified model proposed by Urry & Padovani (1995). This figure is from ASTRO-H White Paper. (bottom) Locations of accreting materials.

2.1.5 Black hole masses of AGNs

The mass $M_{\rm BH}$ of a SMBH is an extremely important parameter to normalize its size scales to the gravitational radius $r_{\rm g} = GM_{\rm BH}/c^2$, where G is the gravitational constant. Similarly, various variations of the AGN may be scaled to $r_{\rm g}/c$, where c is the light speed. Strong gravity dominates motion of stars and gasses near the SMBH. When we measure Keplerian velocity v at a distance r from the SMBH, $M_{\rm BH}$ can be estimated as rv^2/G. We can easily obtain v from the width of emission and absorption lines, but r is difficult to measure.

Dressler & Richstone (1988) measured IR absorption lines of M31 and M32 to determine the stellar rotation and the associated velocity dispersion in these nearest galaxies. The rapid rotation around their central region together with the resolved galactocentric distance, supported the presence of massive nuclei. From the data, they estimated that M31 and M32 harbored SMBHs with masses of 3–7 $\times 10^7 M_\odot$ and $\sim 8 \times 10^6 M_\odot$, respectively. In 1994, the mass of M87 was obtained as $3 \times 10^9 M_\odot$ by the velocity dispersion of stars (van der Marel 1994), as well as the kinematics of an ionized gas disk (Ford et al. 1994; Harms et al. 1994). By accurately chasing the motion of stars around our Galactic center over a decade, Ghez et al. (2008) measured the SMBH mass therein as $4.5 \times 10^6 M_\odot$.

Interferometers with the high spatial- and spectral- resolution are also useful to measure a pair of r and v in some AGNs. As explained in §2.1.2, Miyoshi et al. (1995) performed mass estimation of NGC 4258 using water masers in the surrounding region.

Davis et al. (2013) conducted mass measurements using interferometric observations of CO emission from a cold molecular disk. By observation of NGC 4526 with CARMA observatory, the SMBH mass was obtained as $4.5^{+4.2}_{-3.0} \times 10^8 M_\odot$ (3σ confidence limit). This method was applied to data observed with the ALMA interferometer (Barth et al. 2016), and the SMBH mass of NGC 1332 was measured as $M = 6.64^{+0.65}_{-0.63} \times 10^8 M_\odot$.

Another mass estimation is done by using the technique called reverberation mapping, which is the method to determine the distance of the BLR from the SMBH. The emission lines from the BLR show time delay Δt after the continuum variation from the central compact region. The distance between the BLR and the center of the AGN is estimated as $r = c\Delta t$. As shown in 2.12, masses of 50 AGNs, including Seyfert 1s, NLS1s, and quasars with high variabilities, were well determined with the reverberation mapping, and listed in the AGN Black Hole Mass Database (Bentz & Katz 2015). As shown in figure 2.13, Magorrian et al. (1998) showed corelation between the masses of SMBHs and those of galactic bulges. This is called Magorrian relation. Gebhardt et al. (2000) deepened this idea, and showed that the SMBH mass is tightly correlated with the stellar velocity dispersion. These facts indicate that the SMBH mass is strongly related with the host galaxy's bulge, and are considered to

be evidence of coevolution of the SMBH and the bulge.

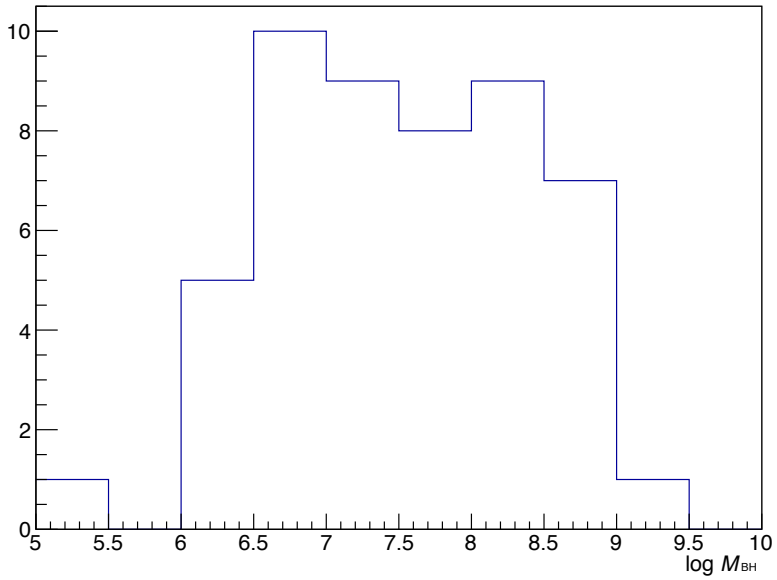

Figure 2.12: AGN mass distribution. The masses are from the AGN Black Hole Mass Database (Bentz & Katz 2015).

2.1.6 Luminosities of AGNs

The AGN luminosities are distributed over a wide range of 10^{43-47} erg s^{-1}, from distant quasars to nearby LINERs. The AGN luminosity is often normalized by the Eddington luminosity, $L_{\rm Edd}$, which is the luminosity when radiative pressure balances the gravity. The equation of balance for a material with volume V is given as

$$V n_{\rm e} \sigma_{\rm T} \frac{L_{\rm Edd}}{4\pi r^2 c} = V n_{\rm B} m_{\rm B} \frac{G M_{\rm BH}}{r^2}. \tag{2.2}$$

This yields

$$\begin{aligned} L_{\rm Edd} &= \frac{4\pi c G M m_{\rm B}}{\sigma_{\rm T}} \left(\frac{n_{\rm B}}{n_{\rm e}}\right), \\ &= 1.26 \times 10^{46} \left(\frac{M}{10^8 M_\odot}\right) \left(\frac{n_{\rm B}}{n_{\rm e}}\right) \text{ erg s}^{-1}, \end{aligned} \tag{2.3}$$

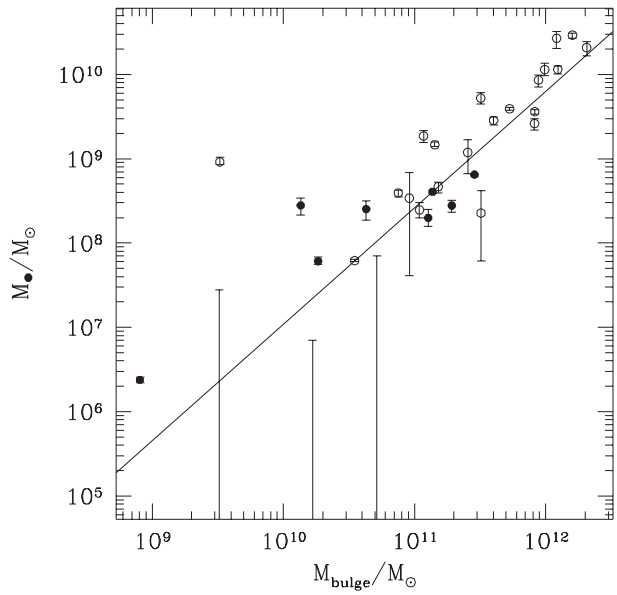

Figure 2.13: The Magorrian relation (Magorrian et al. 1998). The SMBH mass measured with the reverberation mapping is shown as a function of the bulge mass of the host galaxy.

where $\sigma_{\rm T}$, $m_{\rm B}$, $n_{\rm B}$, and $n_{\rm e}$ are the Thomson cross section, the baryon mass, the number of baryons, and the number of electrons, respectively. Corresponding Eddington limit $\dot{M}_{\rm Edd}$ of mass accretion rate, is defined as

$$L_{\rm Edd} = \zeta \dot{M}_{\rm Edd} c^2 \tag{2.4}$$

$$\dot{M}_{\rm Edd} = 1.39 \times 10^{25} \left(\frac{M}{10^8 M_\odot} \right) \zeta^{-1} \ {\rm g \ s^{-1}}, \tag{2.5}$$

where ζ is the radiation efficiency. In the case of the standard accretion disk (see §2.1.7), ζ equals 1/12 because the innermost stable circular orbit (ISCO) is $6r_{\rm g}$ for Schwarzshild black holes. The Eddington ratio η of an AGN with the luminosity L and the mass accretion rate $\dot{M}$ is defined as

$$\eta = \frac{L}{L_{\rm Edd}} = \frac{\dot{M}}{\dot{M}_{\rm Edd}}. \tag{2.6}$$

We can calculate η with the observed parameters of z, $M_{\rm BH}$, and the X-ray flux $F_{\rm X}$, using equation 2.1 and 2.4. Hereafter, η of AGNs is given as explained above using X-ray data.

Many of Seyfert 1s have relatively low accretion rates with $\eta \lesssim 0.01$. Even the most luminous Seyfert 1s, MCG−6-30-15 and IC 4329A, reaches only $\eta \sim 0.1$. On the other hand, many NLS1s have $\eta \gtrsim 0.1$, and even $\eta > 1$ (super Eddington). It means that the motion

of the accreting materials are probably not Keplerian, and extensive gas outflows from the central region of the AGN with velocities of $\sim 0.1c$.

2.1.7 Standard accretion disks

In general, the accreting materials have angular momentum. If it is not reduced, the materials eventually reach the limiting radius where centrifugal force balances the gravity, and the accretion stops. The matter then achieves a condition of nearly Keplerian rotation. However, in that case, the angular rotation frequency increases inwards. Therefore, due to viscosity, inner-region materials with faster rotation drag outer-region materials with slower rotation. In this way, the angular momentum is transported outwards, and the matter can gradually fall to the center. The viscosity also works in heating the accreting materials by efficiently converting the kinetic energy to thermal energy. Taking the viscosity effects into account, Shakura & Sunyaev (1973) proposed the concept of a standard accretion disk, which is geometrically thin and optically thick.

In a standard accretion disk, the materials slowly fall to the SMBH while keeping the near-Kepler motion. According to the virial theorem, half the released gravitational energy is converted to radiation energy. Assuming that the viscous dissipation of the gravitational energy is radiated away as local blackbody radiation, the energy flux of radiation from unit surface of the disk at a radius of r in a unit time is given as

$$F \equiv \sigma T^4 = \frac{3}{8\pi} \frac{G M_{\rm BH} \dot{M}}{r^3} \left(1 - \sqrt{\frac{r_{\rm in}}{r}} \right), \tag{2.7}$$

where σ, T, and $r_{\rm in}$ are Stefan-Boltzmann constant, temperature at r, and an inner disk radius, respectively. Figure 2.14 shows the temperature distribution of equation 2.7, with $M_{\rm BH} = 10^8 M_\odot$, $\eta = 0.1$, and $r_{\rm in} = 6 r_{\rm g}$. The maximum temperature appears in the ultraviolet band near the innermost region of the disk, and seed photons for inverse Compton scattering is generated there.

2.1.8 Radiatively inefficient accretion flow

When $\dot{M}$ is low, the radiative cooling becomes inefficient and the accreting gaseous materials becomes hot. The increased viscosity of the hot gas makes angular momentum transfer more efficient, so that the gas motion becomes more radial rather than circular, and the released gravitational energy is "advected" inwards. Such an accretion flow, called radiatively inefficient accretion flow (RIAF), is geometrically thick and optically thin because the gas

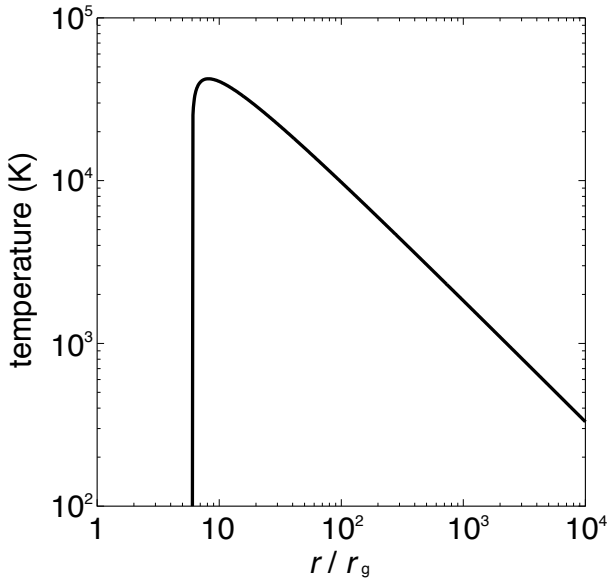

Figure 2.14: The temperature distribution in a standard accretion disk of an AGN with $M_{\rm BH} = 10^8 M_\odot$ and $\eta = 0.1$.

pressure can no longer be neglected. Therefore, the RIAF does not emit black body radiation, but can produce photons via inverse Compton scattering, synchrotron radiation, and other processes. Because of the feature, the RIAF is considered to be a candidate of corona.

A corona, emitting the PL-shaped primary X-ray, is considered to have the electron temperature of ~ 100 keV and the optical depth of $\tau \sim 1$. From its fast variability, the corona should be compact with the size scales of $\lesssim 1000 r_{\rm g}$. However, we have not reached definitive consensus on the position nor the origin of the corona. Therefore, we worked on spectroscopy focusing on the X-ray continuum in the present paper.

2.2 X-ray Emission from Seyfert Galaxies

2.2.1 Primary PL continuum

The PL continuum is considered to be primary X-rays generated by inverse Compton scattering in a corona near the SMBH. This component has a cutoff at the electron temperature $T_{\rm e}$, and its photon-number spectrum is expressed as

$$\propto E^{-\Gamma} \exp\left(-E/k_{\rm B}T_{\rm e}\right), \tag{2.8}$$

where $k_{\rm B}$ is Boltzmann constant. The photon index Γ is approximately expressed as

$$\Gamma = -\frac{1}{2} + \sqrt{\frac{9}{4} + \frac{4}{y}}, \tag{2.9}$$

where y is the Compton y parameter defined with the electron mass $m_{\rm e}$ as

$$y \equiv \max(\tau, \tau^2) \times \frac{4k_{\rm B}T_{\rm e}}{m_{\rm e}c^2}. \tag{2.10}$$

The photon indices and cutoff energies of Seyfert galaxies have been found to be ~ 1.9 and several hundreds keV, respectively (e.g. Beckmann et al. 2009). As a result, $T_{\rm e} \sim 10^9$ K, $y \sim 1$, and $\tau \sim 1$ are derived.

Actually, the geometry of the corona has not yet been determined uniquely by observations. Figure 2.15 shows several possible models proposed so far (Reynolds & Nowak 2003). The top panel shows the simplest model, in which the corona lies on the accretion disk. However, this model predicts a softer PL spectrum than observed because the corona is effectively cooled by Comptonization. The remaining three panels show "photon starved geometries" which was proposed to explain the observed hard X-ray spectra. The middle two panels in figure 2.15 shows models in which a relatively spherical corona is located within the inner edge of the accretion disk, and less effectively cooled. If the corona is patchy like the bottom panel in figure 2.15 and a small fraction of disk emission is intercepted by the corona, the Compton cooling does not work effectively, either. These photon starved geometries can explain the observed hard X-ray spectra (Dove et al. 1997), but it is not yet clear whether any of these pictures is real, and if so, which is correct.

2.2.2 Reflection component

When a part of primary X-rays are reflected, the reprocessed component is characterized by the Fe-K line, the Fe-K edge, a hard X-ray hump and a drop in a soft X-ray band, and

so-called reflection component. Reflection occurs in ionized gasses as well as cool materials, such as the dusty torus. The accreting gas can be ionized by strong illumination by the primary X-ray emission. The ionization parameter ξ is defined as

$$\xi \equiv \frac{L}{nr^2}(\text{erg cm s}^{-1}), \tag{2.11}$$

where L, n, and r are the illuminating luminosity, the gas density, and the distance from the illumination source to the ionized gas. Figure 2.16 shows spectra reprocessed by the ionized gasses. At $\log \xi \sim 2$, the spectrum have many lines from various ionization states of elements. When ξ becomes higher and the number of bound electrons in light elements decreases, the spectral shape becomes continuum-like because the effect of photoabsorption diminishes, the effects of Compton scattering by the ionized matter increased, and the lines are broadened by Compton scattering.

When the reflection component is produced in a region very close to the SMBH, the spectral shape is affected by special and general relativistic effects. Figure 2.17 shows the line profile affected by these effects. Because the accreting materials near the SMBH is rotating fast and moving toward and against the observer, the Fe Kα line is blue- and red-shifted by longitudinal Doppler effect. Further considering transverse Doppler effect, the line profile is redshifted in the second panel from the top in figure 2.17. Relativistic beaming increases the apparent luminosity from materials moving toward the observer, and the blueshifted line becomes stronger. Finally, gravitational redshift affects the line profile. As a total of these effects, the emission line is broadened and acquires a low energy tail.

The relativistically smeared Fe line has been apparently detected in X-ray spectra of very large number of Seyfert 1's, begining with the bright Seyfert I galaxy, MCG−6-30-15 with the *ASCA* satellite (Tanaka et al. 1995). Figure 2.18 shows the Fe K line observed from MCG−6-30-15 fitted with the relativistic line model in figure 2.17. This Fe feature was also detected with *Suzaku* as shown in figure 2.18 (Miniutti et al. 2007). The relativistic reflection component had a strong hard X-ray hump in the 15–30 keV. Many AGNs have strong excesses in 5–7 keV and hard X-rays to produce by the "normal" relativistic reflection. To explain these features, Miniutti & Fabian (2004) proposed a light bending model, in which the optical path is bended by strong gravity and larger fraction of the source flux is reflected in the inner disk region. Using this model, the spectrum required the inner disk radius $< 2.2r_{\rm g}$. In Schwarzshild black holes, their ISCO is $6r_{\rm g}$, while spinning black holes, Kerr black holes, can have smaller ISCOs. In a spinning black hole, the spin parameter a is defines as

$$a = \frac{cJ}{GM_{\rm BH}^2}, \tag{2.12}$$

where J is the angular momentum of the SMBH. When $a = 0$ the SMBH does not rotate, and when $a = 1$ it maximally rotates. The *Suzaku* spectrum of MCG−6-30-15 required $a > 0.917$, and the many AGNs were inferred to be highly spinning (e.g. Nandra et al. 2007). However, such a highly relativistically smeared Fe line is mixed in the PL-shaped continuum. Therefore, the 5–7 keV range and hard X-ray excesses can be interpreted as the partial covering absorption, effects of an absorption line of the outflow (see §2.2.3), or the other primary PL.

2.2.3 Absorption

X-rays from AGNs are not only reflected but also photoabsorbed by surrounding materials. If we simply assume the absorber to have 1 solar abundance, the absorption can be specified by two parameters, the column density $N_{\rm H}$ and the ionization parameter ξ. Figure 2.19 shows spectral shapes when a $\Gamma = 2.0$ PL is absorbed by neutral absorbers of various $N_{\rm H}$, and ionized absorbers of different ξ. When the gas becomes dense, softer X-ray flux drastically decreases and absorption edges becomes deeper. When ξ increases, the spectrum becomes softer, and the energies of the absorption edges higher. These tendencies are the same as that in the ionized reflection. When the absorber partially covers the X-ray source, a part of its emission is absorbed while the rest is not. This situation is called partial covering absorption.

Spectra of NLS1s show absorption features by ionized gasses, called warm absorbers (WAs), which are considered to originate from the outflows. A candidate of the outflows is a disk wind blowing from the accretion disk, which is ionized by X-ray illumination. Figure 2.20 shows spectra of the NLS1, 1H0707−495. Hagino et al. (2016) discovered the X-ray spectra to harbor a broad Fe absorption line, while they had been convinced to be dominated by the relativistic reflection.

2.3 Multi-zone Comptonization View

For decades, the primary PL component had been considered to be single. Although X-ray spectra of AGNs are known to become harder when the sources are fainter, all of them had been ascribed to the partial covering absorption. Another mystery is that X-rays of AGNs are or are not correlated with optical emission. The Seyfert 1, NGC 3516, did not show any correlation when the source was bright (Maoz et al. 2002), while X-rays were strongly correlated with optical fluxes when the source was faint (Noda et al. 2016).

Noda et al. (2011a) discovered that the X-ray spectra of MCG−6-30-15 harbor another hard primary PL emission, by the C3PO method. This method enables us to decompose a spectrum into a variable component and a stationary one, when the shape of the variable component is constant in the observation. When the variable component has a constant shape in an observation, count-count plots (CCPs) show linearity. In the C3PO method, we make CCPs between an arbitrary band and a reference band, in which the stationary component is negligible. Figure 2.21 shows a CCP of MCG−6-30-15, fitted with a straight line of $y = ax + b$. The count rate y can be decomposed into a variable part, ax_0, and a stationary part, b, where x_0 is the average count rate in the reference band. Collections of ax_0 and b form the variable and stationary components, respectively.

By the C3PO method, many Seyfert 1s have been revealed to have two primary PL components in their X-ray spectra (Noda et al. 2011a,b, 2013a,b, 2014; Miyake et al. 2016). In many of the Seyfert 1s, one PL is softer with $\Gamma \sim 2.0$ and rapidly variable, while the other is harder with $\Gamma \sim 1.4$ and slowly variable.

The spectral picture, called multi-zone Comptonization (MZC), clearly explained the spectral transition of AGNs. The soft PL is dominant and highly variable when the source is bright, while the hard PL is dominant and variable when the source is faint (e.g. Noda et al. 2014). In NGC 3516, only the hard PL is correlated with the optical emission, but the soft PL is not (Noda et al. 2016). From the correlation with the disk optical emission, a corona generating the hard PL is considered to be located near the disk. The best candidate of the hard PL source is a RIAF, which is considered to be dominant when the source is dim.

The soft PL makes a huge contribution to X-ray spectra of AGNs, and their variability. However, the position of the source of the soft primary X-rays is hardly understood. In the present thesis, we approach this remaining mystery by analysis of NLS1s. This type of AGNs exhibit softer X-ray spectra and violent variability. By extraction of the variable radiation component using the timing analysis, we can obtain much information about the soft PL source.

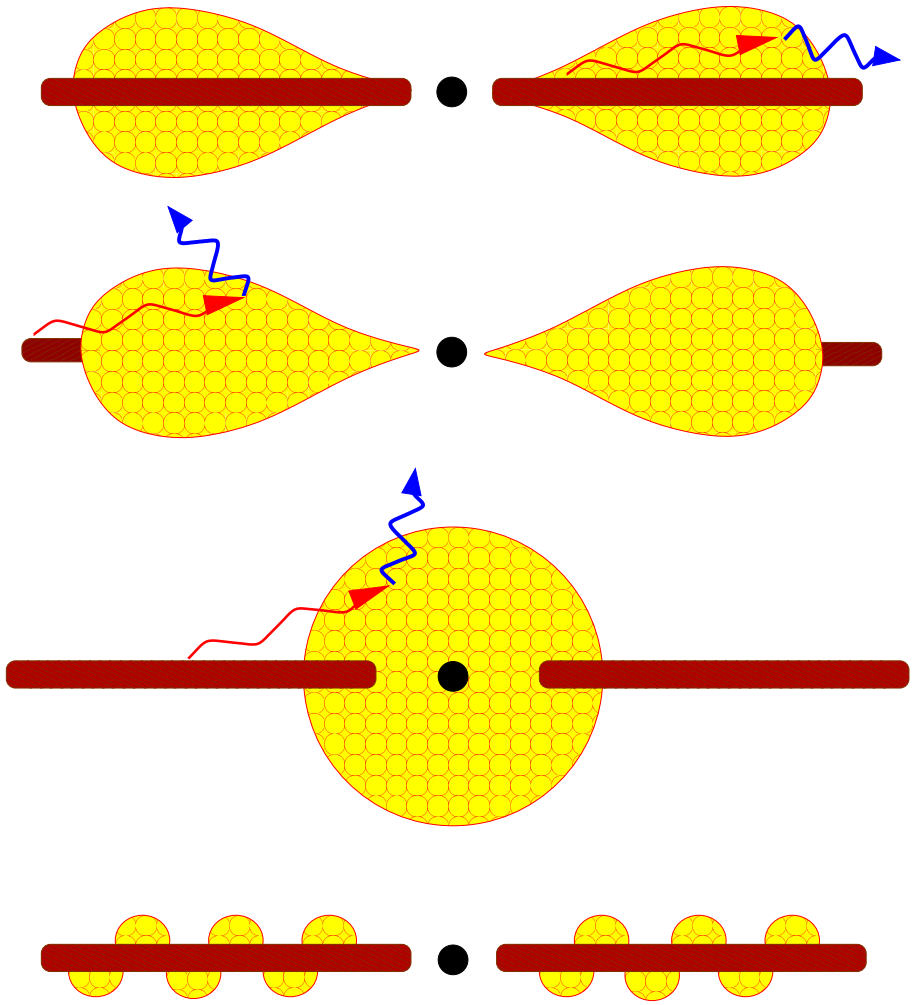

Figure 2.15: Possible geometries of the Comptonizing corona (yellow), relative to the SMBH (black) and the accretion disk (brown) (Reynolds & Nowak 2003). The top panel shows a "slab" or "sandwich" geometry, the middle two panels "sphere+disk geometries" view, and the bottom "patchy corona" or "pill box" model.

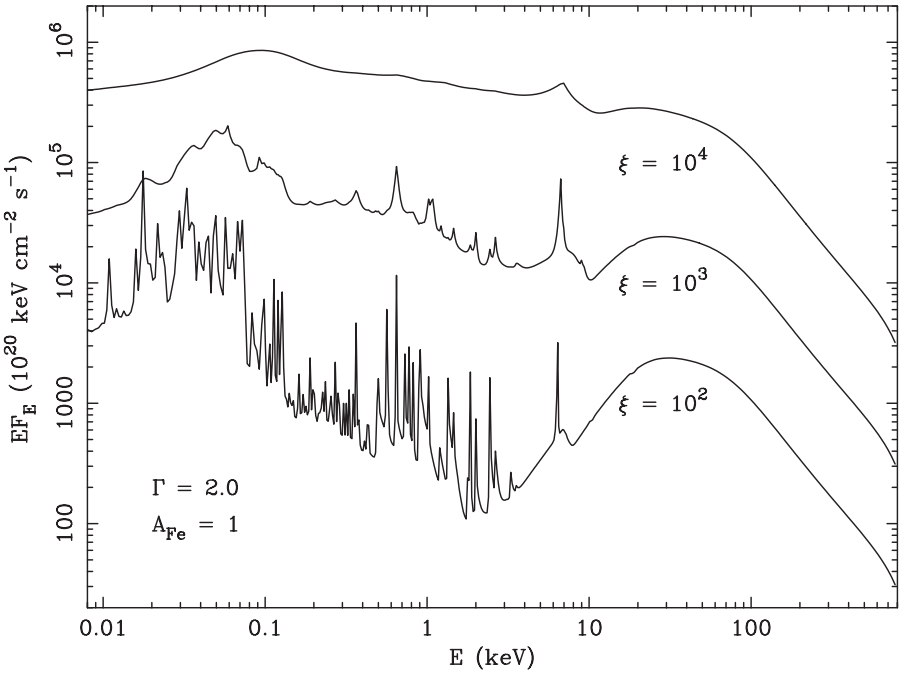

Figure 2.16: Spectra of the ionized reflection component with $\xi = 10^2$, 10^3, and 10^4 (Ross & Fabian 2005). The incident spectrum has $\Gamma = 2.0$, and the reflector is assumed to have one-solar Fe abundance.

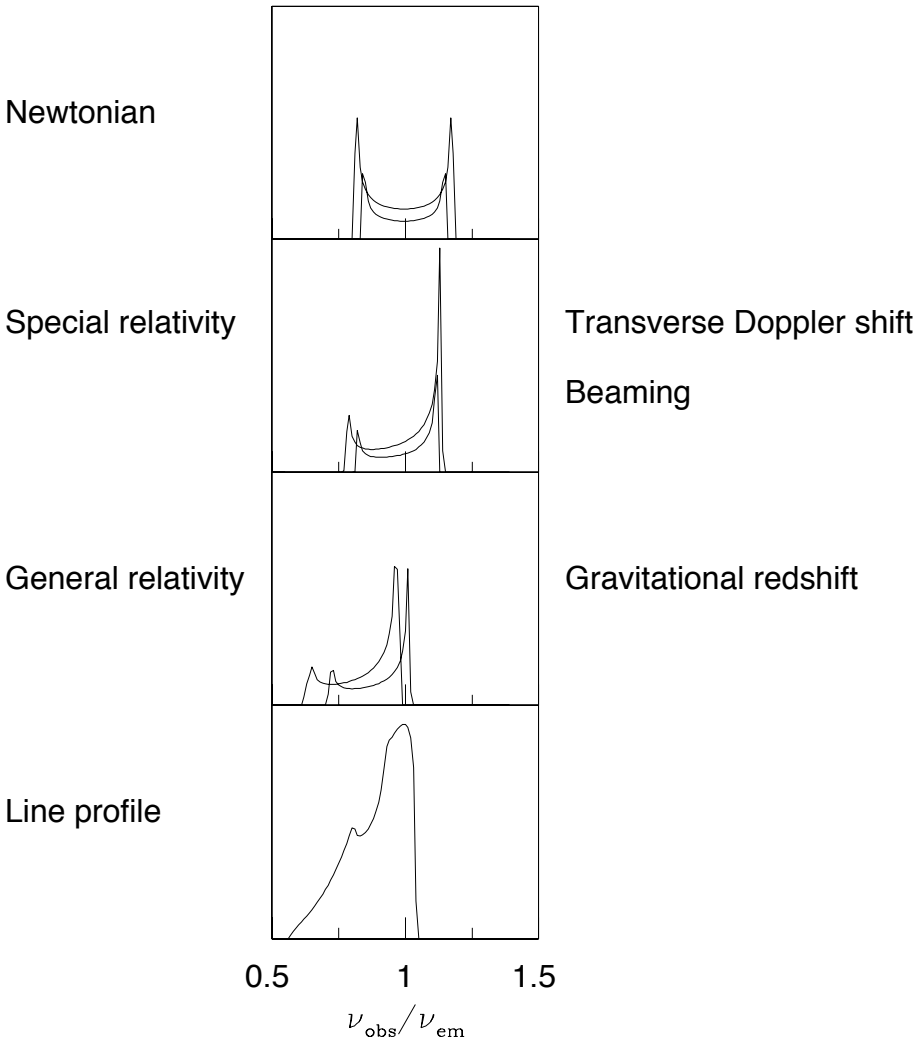

Figure 2.17: The Fe-K line profiles expected to arise from inner regions of the accretion disk. It is modified by the interplay of Doppler and transverse Doppler shifts, relativistic beaming, and gravitational redshift (Fabian et al. 2000).

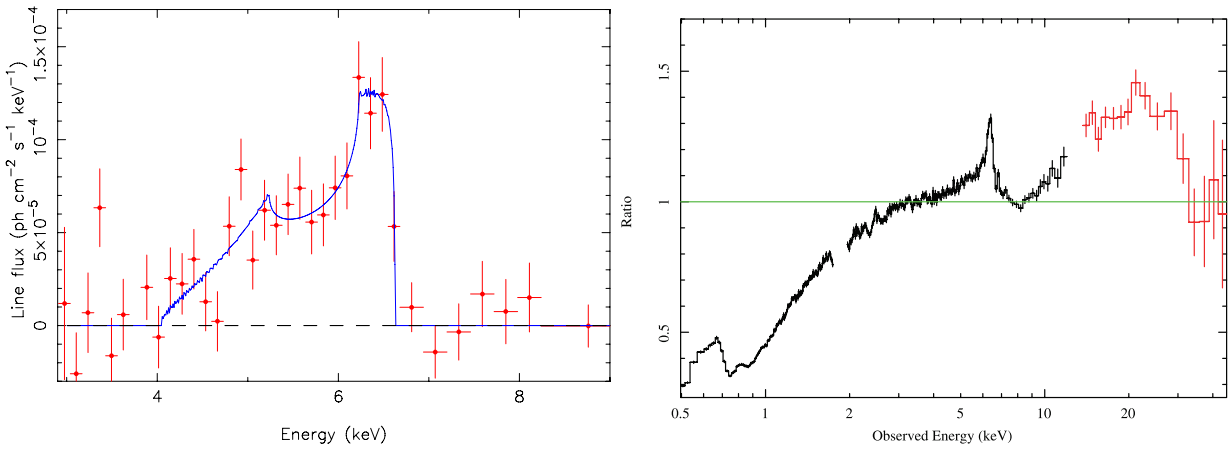

Figure 2.18: (left) The Fe-K line profile from MGC–6-30-15 observed with *ASCA* (Tanaka et al. 1995). In the spectrum, the continuum assuming a single PL shape is subtracted. (right) The *Suzaku* spectrum of MGC–6-30-15, in the form of its ratio to a PL fitted in energy bands excluding the absorption, the Fe line, and the hard X-ray hump features (Miniutti et al. 2007).

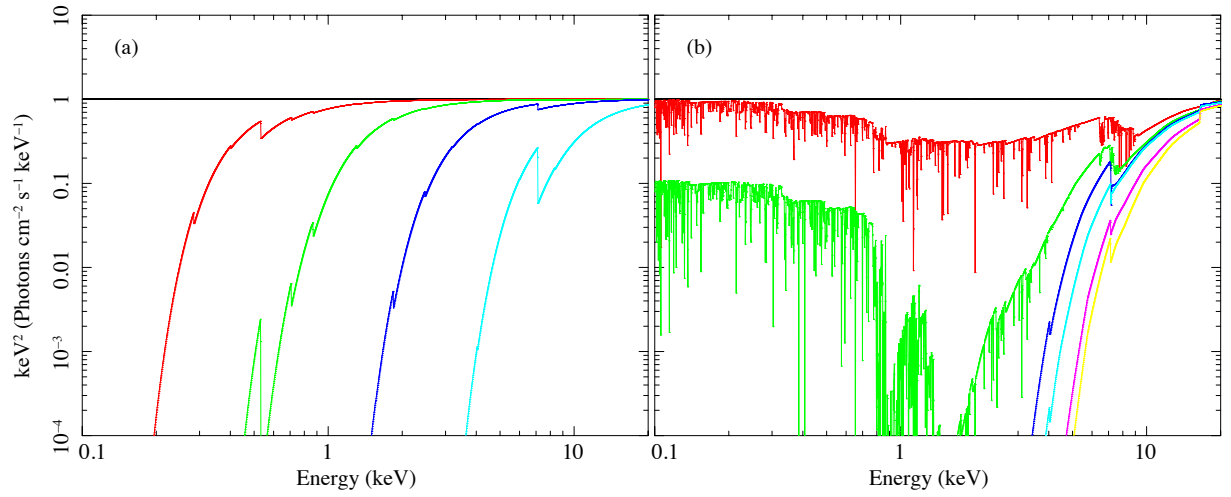

Figure 2.19: Relative changes in the spectral shape when the $\Gamma = 2.0$ PL (black) is absorbed by materials with solar abundance. (a) Absorption by a neutral gas with $N_{\rm H} = 10^{21}$ (red), 10^{22} (green), 10^{23} (green), and 10^{24} cm^{-2} (cyan). (b) Absorption by an ionized gaseous matter with $N_{\rm H} = 10^{24}$ cm^{-2} and $\log \xi = 3$ (red), 2 (green), 1 (blue), 0 (cyan), -1 (magenta), and -2 (yellow). The ionized absorber is modeled by Reeves et al. (2008).

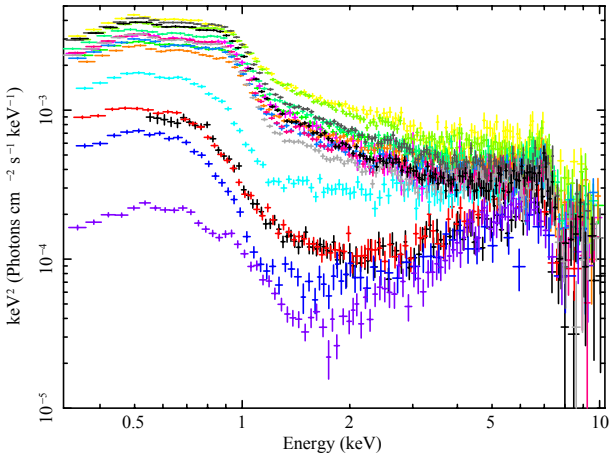

Figure 2.20: Spectra of the NLS1, 1H0707−495 (Hagino et al. 2016).

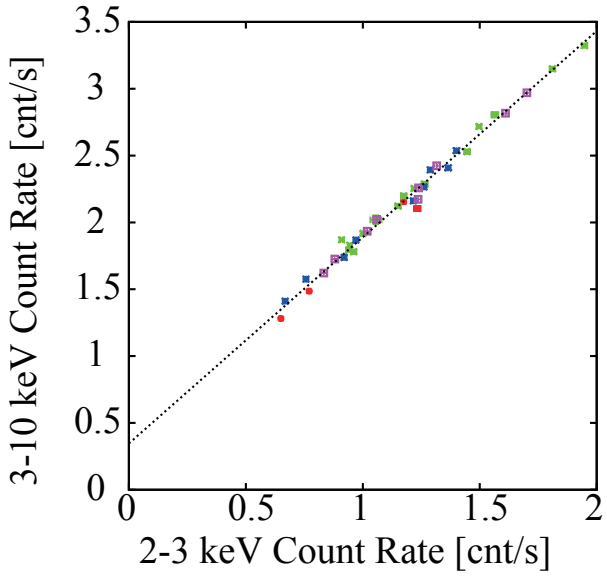

Figure 2.21: A CCP of MCG−6-30-15 between a reference band of 2–3 keV and the 3–10 keV band.

Chapter 3

INSTRUMENTATION

3.1 *Nuclear Spectroscopic Telescope Array* (*NuSTAR*)

3.1.1 Overview

Nuclear Spectroscopic Telescope Array (*NuSTAR*) was launched on 2012 June 13. It is the first in-orbit observatory capable of focusing hard X-rays. This observatory carries out high-sensitivity imaging spectrascopy in 3–79 keV, which is beyond the $\sim$ 10 keV high-energy cutoff achieved by all previous X-ray satellites. The difficulty of using grazing incident optics in hard X-ray band determined the limitation of the previous satellites, because the critical angle for the total reflection of hard X-ray photons is $< 1^\circ$; in the case of Au, the critical angle is 0.5° at 10 keV and 0.1° at 50 keV. In addition to the total reflection, Bragg reflection by multilayer-coated X-ray mirror is utilized to achieve concentrating hard X-rays in optics of *NuSTAR*.

Figure 3.1 shows an illustration of *NuSTAR*, which mounts two optics modules. Each optics consists of the X-ray telescope and the focal plane module (FPM). The FPM consists of a solid state CdZnTe (CZT) pixel detector and a surrounding CsI anti coincidence shield.

3.1.2 X-ray Telescopes

The X-ray telescopes of *NuSTAR* are Wolter-I type telescopes consisting of 133 grazing incidence shells, of which inner 89 shells are coated with depth-graded Pt/C multilayers and outer 44 with W/Si. The depth-graded multilayer coating achieves Bragg reflection of hard X-rays, and contributes the large effective area at > 10 keV. The focal length is 10.14 m. Figure 3.2 shows the effective area of *NuSTAR* compared with those of other satellites. The

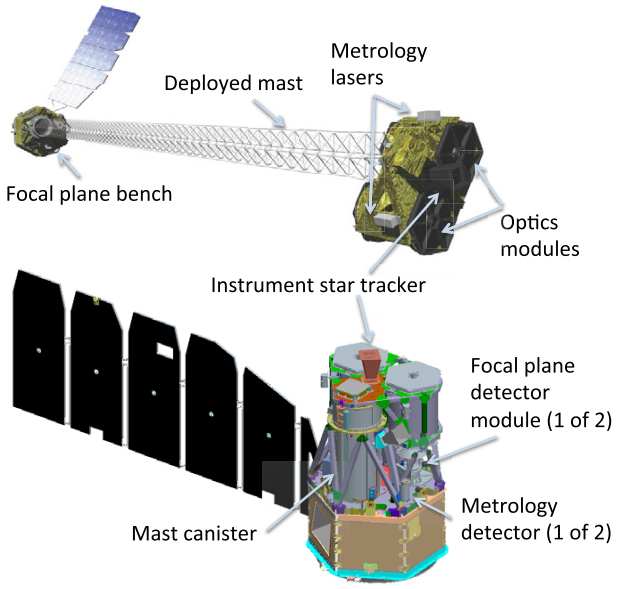

Figure 3.1: An illustration of *NuSTAR* in the deployed (top) and stowed (bottom) configurations (Harrison et al. 2013).

area of *NuSTAR* is significant in hard X-ray while those of the other satellites drops at $\sim$ 10 keV. A drop in *NuSTAR* at 78.4 keV is ascribed to Pt-K edge used in the inner shells. Another drop due to W-K edge used in the outer shells can be seen at 69.5 keV.

Figure 3.3 shows the reduction in the effective area as a function of the off-axis angle, which is called vignetting function. Reflectivity of optics depends on the position and the angle of an incident photon. The vignetting effect becomes larger at the off-axis angle $> 2'$ and with larger energies of incident photons. These effects are corrected when we analyze data obtained with *NuSTAR*.

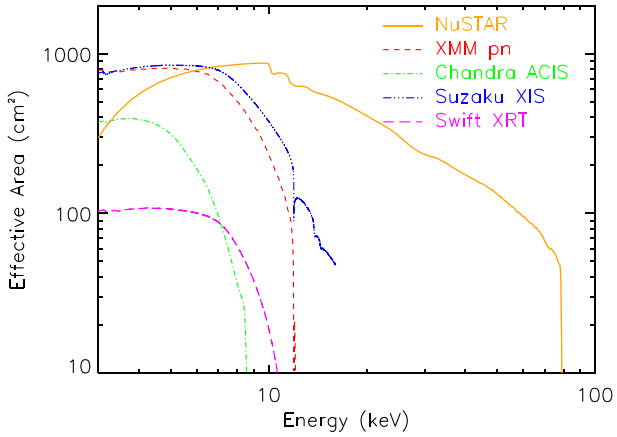

Figure 3.2: Effective area of *NuSTAR* compared with those of other X-ray observatories (Harrison et al. 2013).

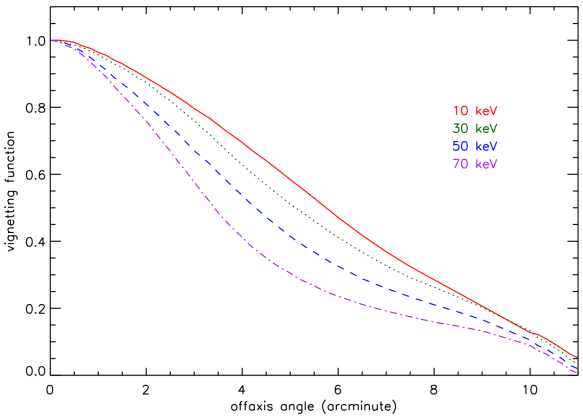

Figure 3.3: The reduction in effective area as a function of off-axis angle resulting from vignetting in the optics (Harrison et al. 2013).

3.1.3 Focal Plane Module (FPM)

The two X-ray telescopes has their own FPM, called FPMA and FPMB. Figure 3.4 shows a cross-sectional view of the FPM. The main detector of the FPM is surrounded by the CsI shield. As shown in the right panel of figure 3.4, the FPM consists of a 2×2 array of CZT pixel detectors. Each detector has a collecting area of 2 cm $\times$ 2 cm and a thickness of 2 mm. The anode electrodes are attached to make 32×32 grid with a pixel pitch of 605 μm. CZT has a high atomic number (48 for Cd and 52 for Te) and a wide band gap of ~ 1.5 eV. The former contributes to increase of detection efficiency of hard X-rays, and the latter enables operation at near room temperature. Combined with the mirrors, the field of view of each FPM is $12' \times 12'$. The energy resolution is 0.4 keV below 50 keV, and increases to 1.0 keV at 86 keV (full width of half maximum; FWHM).

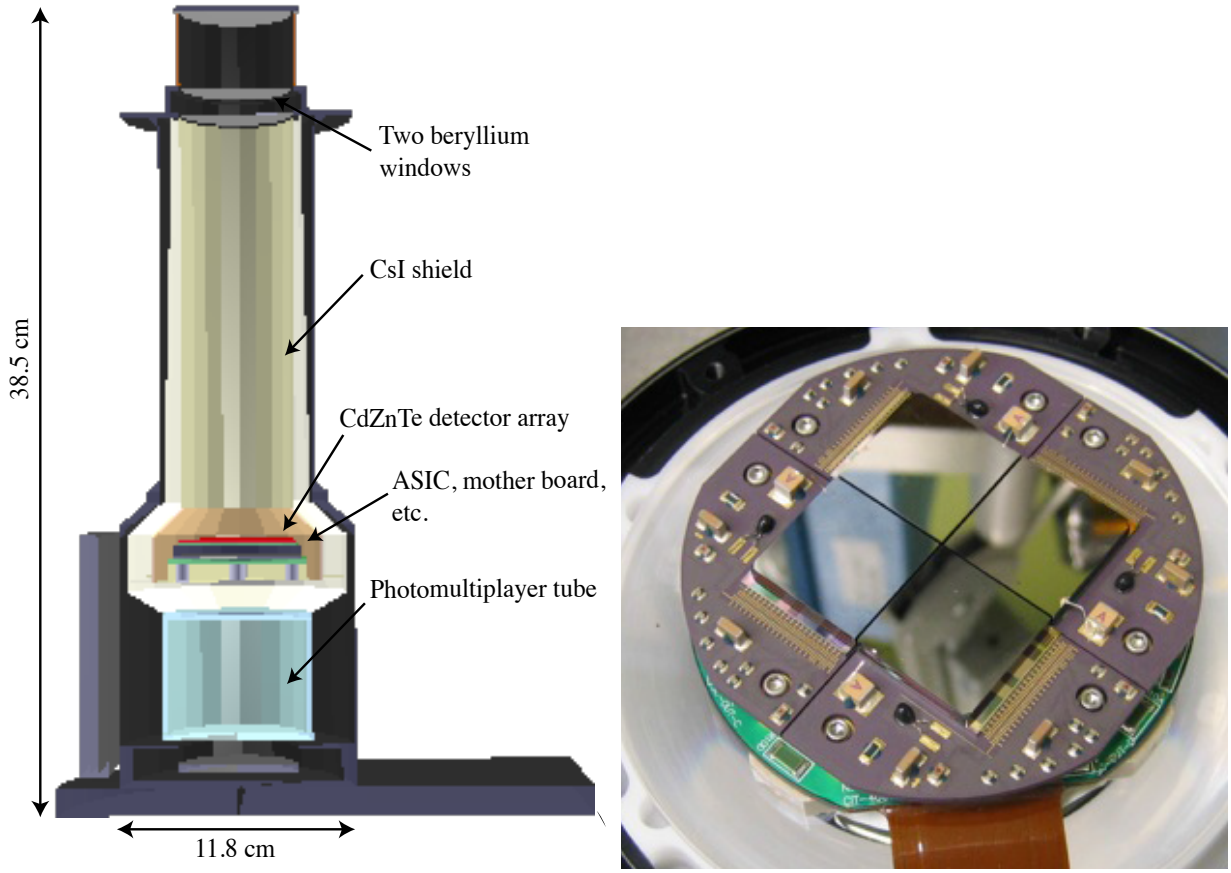

Figure 3.4: A schematic view (Kitaguchi et al. 2011) and a photograph (Harrison et al. 2013) of the FPM.

The CsI shield works as not only passive shield but also active shield. Figure 3.5 shows in-orbit background spectra. The shield significantly reduced the background in a whole energy band, while fluorescence lines from CsI remained after background rejection. Continuum below 10 keV originates from the cosmic X-ray background (CXB) from apertures of the optics or detectors.

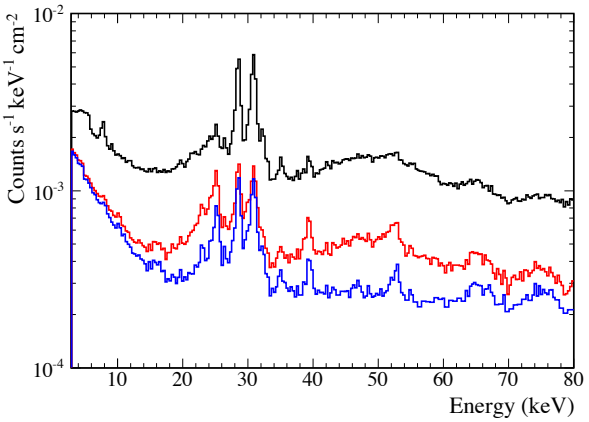

Figure 3.5: In-orbit background spectra of the FPM with different background rejection methods (Kitaguchi et al. 2014). Those without any rejection (black), with anti-coincidence (red), and with all background rejection (blue) are normalized by the geometrical area. The data were obtained from observations of a blank sky, the North Ecliptic Pole.

3.2 *Suzaku*

3.2.1 Overview

Suzaku was the fifth Japanese X-ray satellite, following *Hakucho* (launched in 1979), *Temma* (1983), *Ginga* (1987), and *ASCA* (1993). It was launched on 2005 July 10 aboard the M-V-6 rocket from the Uchinoura space center. The satellite entered into an orbit with the altitude of 570 km, the inclination angle of 31°, and the orbital period of 96 minutes. Because of the low-altitude orbit, background signals were reduced due to the geomagnetic shielding of cosmic rays and *Suzaku* achieved high sensitivity. After 10 years, JAXA terminated operation of the *Suzaku* satellite in 2015.

Figure 3.6 shows schematic views of the *Suzaku* satellite. It mounted five pairs of the X-ray Telescope (XRT) and detectors, and one hard X-ray detector. With these instruments, *Suzaku* covered 0.3–600 keV wide band simultaneously. Four of the five XRT focused 0.2-12 keV photons on four X-ray sensitive Si charge-coupled devices (CCD), the X-ray Imaging Spectrometer (XIS), while the other on the X-ray Spectrometer (XRS) with an energy resolution of 7 eV (FWHM) (Kelley et al. 2007). Unfortunately, the XRS was shut down because liquid helium of its cryostat entirely evaporated by 2005 August 8 due to malfunctions of its cooling system.

3.2.2 The X-ray Telescope (XRT)

As shown in figure 3.7, there were five almost identical XRTs covering 0.2–12 keV. It is Wolter-I type telescope, which consisted of 175 concentrically nested foils. The foil was made of 152 μm thick Al foil, coated with $>$ 1000 Åof Au. The four mirrors (XRT-I0 to XRT-3) with the focal length of 4.75 m were used for XIS and the other (XRT-S) with focal length of 4.5 m for XRS. Figure 3.8 shows the effective area of the XRT. The large effective area, comparable to that of *XMM-Newton* at $>$ 7 keV, was achieved with weight of $<$ 20 kg per one mirror.

3.2.3 The X-ray Imaging Spectrometer (XIS)

The XIS is composed of the four X-ray CCDs. Figure 3.9 shows a photograph and a schematic view of the XIS. Three of them (XIS 0, 2, and 3) are identical and contain front illuminated (FI) CCDs, while the other (XIS 1) uses a back illuminated (BI) CCD. Each CCD is located on the focal plane of the corresponding XRT, and works individually. As shown in the

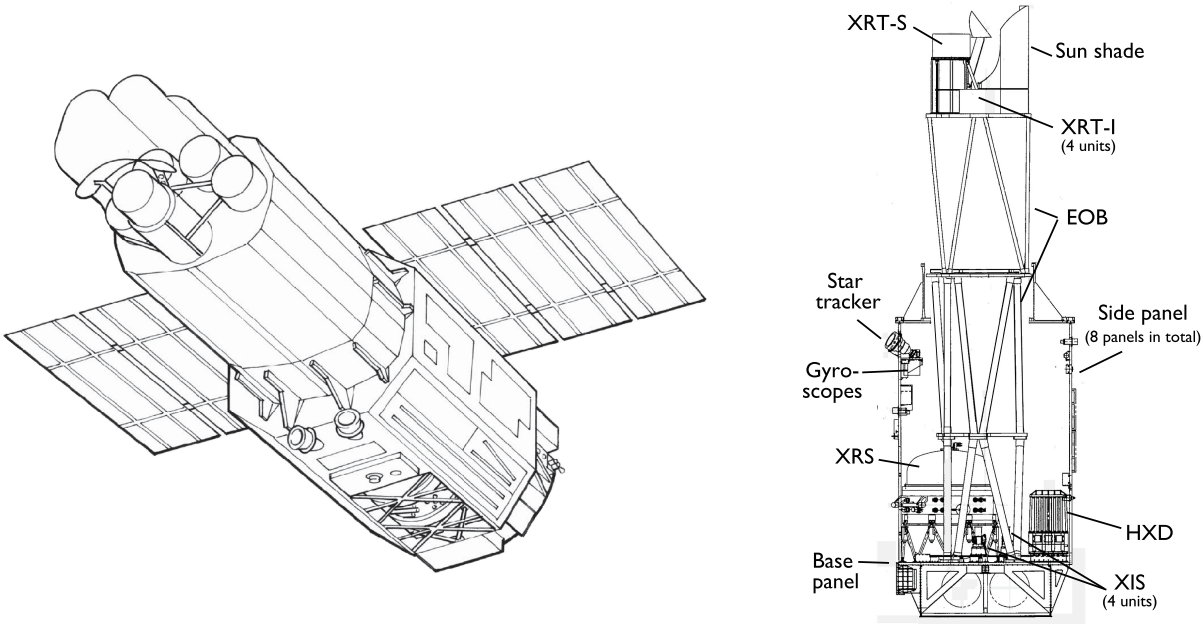

Figure 3.6: *Suzaku* schematic outer (left) and cross sectional(right) views (Mitsuda et al. 2007).

right panel of figure 3.9, each CCD consists of four segments. Each XIS unit has two ^{55}Fe calibration sources, which are located on a side wall of the bonnet and illuminate the two corner of the imaging area. Therefore, these corners should be excluded in imaging spectroscopy. The energy resolution is 130 eV (FWHM) at 6 keV.

Figure 3.10 shows the quantum efficiency of XIS FI and BI as a function of incident energy. Because the front side of the CCD has electrodes and thin gate insulating layers made of Si and SiO2, XIS FI is less sensitive in a lower energy band than XIS BI. On the other hand, XIS FI has higher efficiency at > 4 keV, because its depletion layer is thicker than that of XIS BI. In the present thesis, we mainly use XIS FI data for AGN wide band spectroscopy.

On 2006 November 9, XIS 2 suddenly showed anomaly. Two thirds of imaging area including the central imaging area became unusable and cannot have been recovered. For that reason, XIS 2 stopped working. This anomaly is considered to be caused by collision of micrometeorites. A similar trouble occurred also in XIS 0 on 2009 June 23, but fortunately the lost area was 1/12 at an edge of the imaging area.

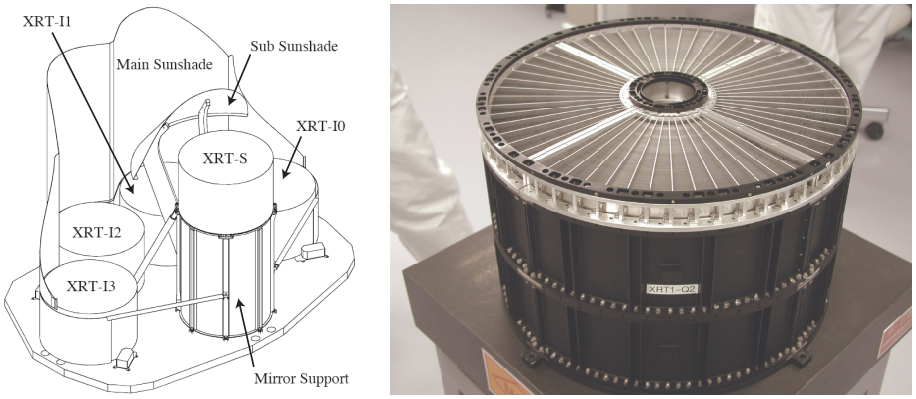

Figure 3.7: A schematic view (left) and a photograph (right) of the XRT (Serlemitsos et al. 2007).

3.2.4 The Hard X-ray Detector (HXD)

The HXD covers a wide energy range of 10–600 keV by the combination of Si PIN diodes and GSO scintillators, as shown in figure 3.11. In the hard X-ray band, signals from celestial objects are weaker than detector backgrounds, because of cosmic rays and emission from radioactive nuclei activated in the detector. These backgrounds are reduced by the combination of well-type detector units and surrounding $Bi_4Ge_3O_{12}$ (BGO) scintillator. Each well unit consists of a PSnCu fine collimator, well-type BGO, and the main detectors, HXD PIN and GSO. The collimator absorbs X-rays from out of view. The well-type and surrounding BGO work as passive and active shield. As shown in figure 3.12, these passive and active shields significantly reduce the background. The surrounding BGO units have effective area of 800 cm^2 at 100 keV and 400 cm^2 at 1 MeV. Thanks to this large effective area, these BGO units are used as a wide-band all-sky monitor (HXD WAM) to detect gamma-ray bursts.

The PIN and GSO detectors are located at the bottom of the BGO well. Figure 3.13 shows their effective area. X-rays with energy of 10–40 keV is absorbed in the PIN diodes with a thickness of 2 mm, and higher energy photons go through the PIN to be absorbed in the four GSO scintillators with a thickness of 5 mm each.

Because the HXD is an non-imaging instrument, we have to estimate its background. The Non-X-ray background (NXB) of the HXD was modeled by Fukazawa et al. (2009), based on such information as the spacecraft location around the Earth, the elapsed time after the SAA passages, and the instantaneous upper-discrimination hits.

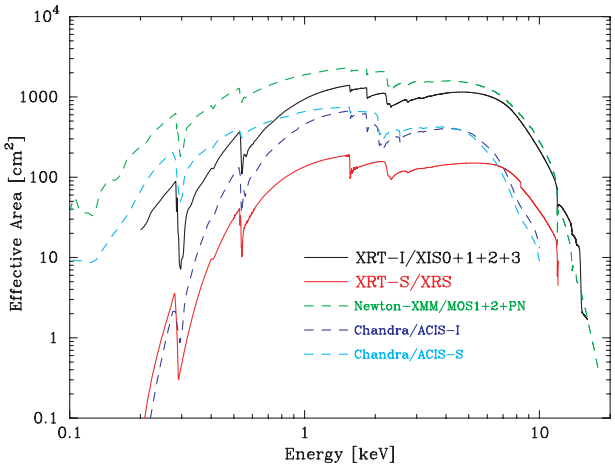

Figure 3.8: Total effective area of XRT units compared with those of *XMM-Newton* and *Chandra* (Serlemitsos et al. 2007).

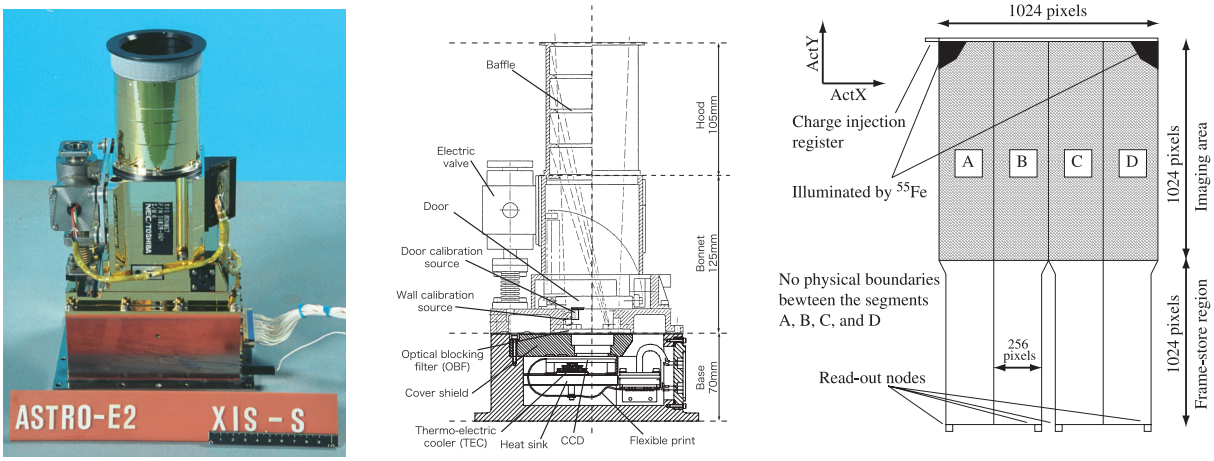

Figure 3.9: A photograph (left) and a schematic view (middle) of the XIS, and a schematic view of the CCDs (Koyama et al. 2007).

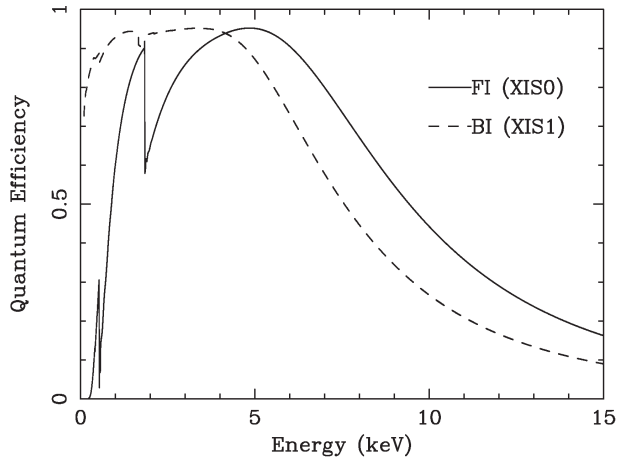

Figure 3.10: The quantum efficiency of XIS FI and BI as a function of incident energy (Koyama et al. 2007).

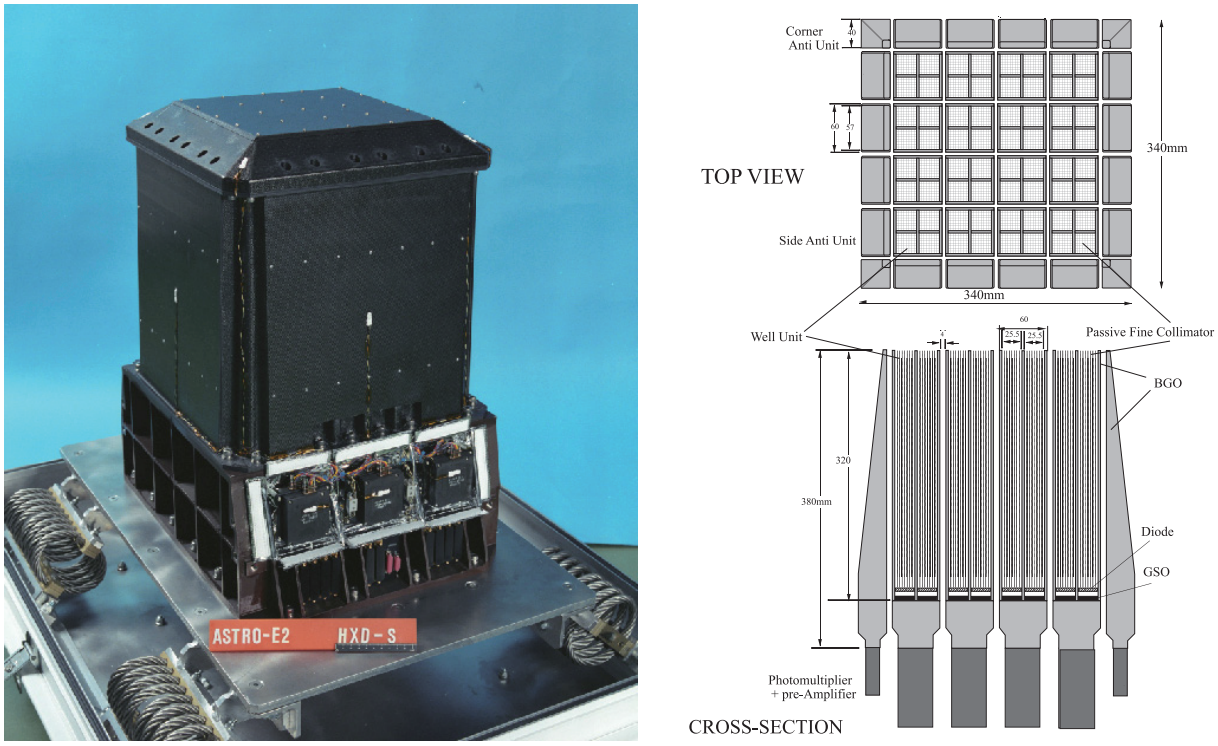

Figure 3.11: A photograph (left) and a schematic view (right) of the HXD (Takahashi et al. 2007).

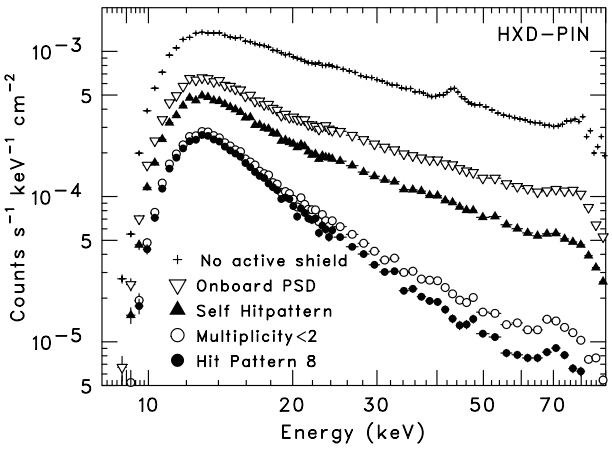

Figure 3.12: Background spectra of HXD PIN under various reduction conditions (Takahashi et al. 2007). The background was reduced by the active shield from + to •.

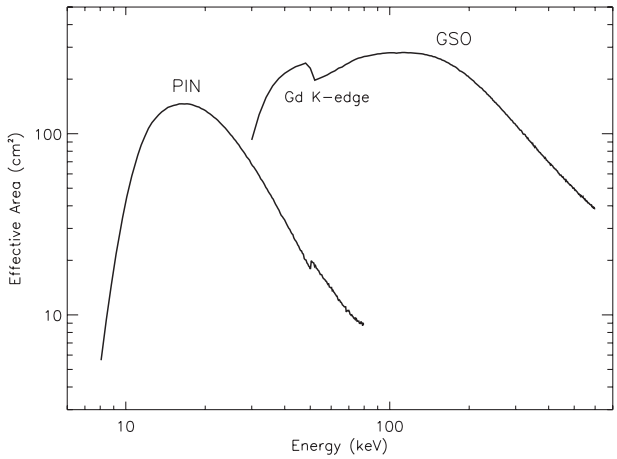

Figure 3.13: Total effective area of HXD PIN and GSO (Takahashi et al. 2007).

Chapter 4

OBSERVATION AND DATA REDUCTION

4.1 Strategy of the Present Thesis

We analyze broad-band X-ray data of representative NLS1s for their primary continua. Because their X-ray emission has been known to distribute over broad energy ranges, with the photon flux decreasing toward higher energies, the sensitivity to hard X-rays is essential in our study. The observatory most suitable for the purpose is *NuSTAR*, which covers up to 78 keV and has the highest sensitivity and the largest effective area even in the hard X-ray band. However, a disadvantage of *NuSTAR* is the lack of sensitivity to soft X-rays below 3 keV, where some AGNs are known to exhibit complex absorption features. Therefore, we analyze *Suzaku* data of such AGNs instead of *NuSTAR*, because the combination of the *Suzaku* XIS, covering the 0.5–10 keV, and the HXD, covering the 15–45 keV, enables us to investigate absorption features.

4.2 Target Selection

4.2.1 Primary sample

So far, 9 NLS1s have been observed with *NuSTAR*. The total number of the observations is 25, and all of these data have been made public. Table 4.1 summarizes these observations, which defines our a primary sample.

Table 4.1: All the NLS1s observed with *NuSTAR* (our primary sample).

	date (YYYY/MM/DD)	exposure	V (cnt)	$V'_{\rm max}$ (cnt)	selected
1H 0323+342	2014/03/15	101 ks	2270	—	
1H 0707−495	2014/05/05	144 ks	1110	473	
	2014/06/10	49 ks	644	473	
	2014/06/28	47 ks	331	235	
Ark 564	2015/05/22	211 ks	25700	—	◯
Mrk 335	2013/06/13 08-	21 ks	427	4590	
	2013/06/13 21-	22 ks	514	2360	
	2013/06/25	93 ks	2500	4590	
Mrk 766	2015/01/24	90 ks	8220	5300	◯
	2015/07/05	24 ks	1150	5300	
NGC 1365	2012/07/25	36 ks	1910	26500	
	2012/07/26	41 ks	1680	25700	
	2012/12/24	66 ks	6740	22100	
	2013/01/23	74 ks	19700	26500	
	2013/02/12	70 ks	10100	17600	
NGC 4051	2013/06/17 16-	9 ks	1060	8880	◯
	2013/06/17 21-	46 ks	7040	13300	◯
	2013/10/09 13-	10 ks	354	12600	◯
	2013/10/09 20-	50 ks	4480	25600	◯
	2014/02/16	57 ks	7460	25600	◯
NGC 5506	2014/04/01	57 ks	6310	—	
Swift J2127.4+5654	2012/11/04	49 ks	4290	13500	◯
	2012/11/05	29 ks	1290	6600	◯
	2012/11/06	75 ks	7100	11200	◯
	2012/11/08	42 ks	4280	13500	◯

Table 4.2: The selected NLS1s.

	$M_{\rm BH}$ ($10^6 M_\odot$)	z
Ark 564	2.6 (Botte et al. 2004)	0.0247 (Huchra et al. 1999)
Mrk 766	1.26 (Giacchè et al. 2014)	0.012929 (Smith et al. 1987)
NGC 4051	1.7 (Denney et al. 2009)	0.002336 (Verheijen & Sancisi 2001)
Swift J2127.4+5654	15 (Malizia et al. 2008)	0.0144 (Sazonov et al. 2007)

4.2.2 Final sample

From the primary sample, we further select NLS1s with strong variability needed for timing spectroscopy. For this purpose, a quantity named "variability significance", V, is defined in the following way. First, for each data set, we define "high" and "low" phases in which the source flux is higher and lower than the average, respectively. In short, this V is defined as

$$V = (r_{\rm h} - r_{\rm l}) \times t, \tag{4.1}$$

where $r_{\rm h}$, $r_{\rm l}$, and t is the average count rate in the high phase, that in the low phase, and the average exposure of the two phases. V is the number of signal photons that contribute to the source variation. To detect a change in the spectral slope with $\sim 5\%$ accuracy, V must be larger than 6500. Seven observations of five objects which satisfy $V > 6500$ survived this screening.

Among the five objects, the X-ray spectrum of NGC 1365 is known to be contaminated by strong absorption lines due to an outflow as shown in figure 4.1 (Walton et al. 2014). Because the absorption features prevent accurate spectral decomposition, NGC 1365 was eliminated.

Even though an object exhibited $V < 6500$ in a particular observation, we may utilize that particuler data if the source was observed on a separate occasion and showed a different intensity, to allow us to study differences between such observations. For this purpose, we introduce another parameter V' to evaluate source variations among different observations of the same source. This V' can be calculated by adopting a pair of observations instead of the high and low phases. In table 4.1, the max values of V', $V'_{\rm max}$, are listed. Six observations of NGC 4051 and Swift J2127.4+5654 satisfying $V'_{\rm max} > 6500$ were revived for our analysis. The selected 11 observations are marked with circles in table 4.1. and they define the final sample of the present thesis. Table 4.2 shows the four NLS1s in the final sample.

Among the objects, NGC 4051 is known to be absorbed by ionized gasses, so we employ *Suzaku* data for its study in addition to the *NuSTAR* data.

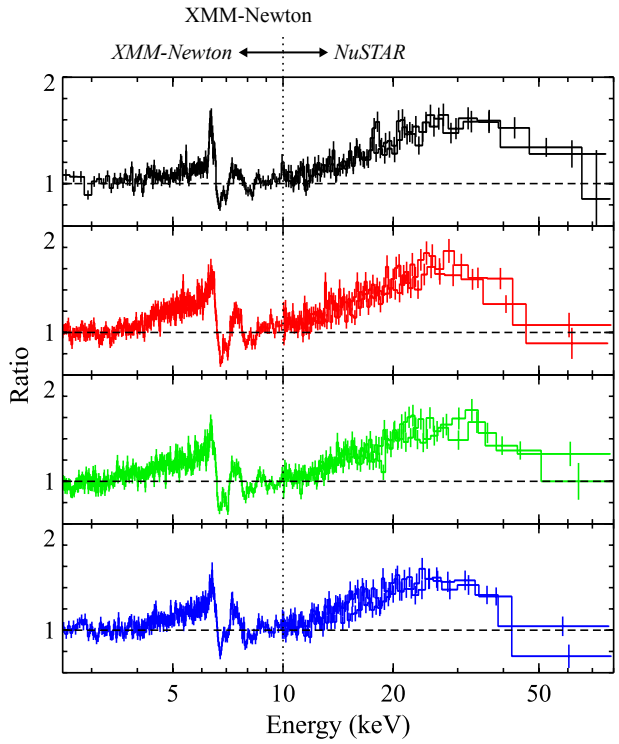

Figure 4.1: X-ray spectra of NGC 1365 obtained simultaneously with *XMM-Newton* and *NuSTAR* on four occasions, shown in the form of their ratios to a PL with $\Gamma = 1.75$, and its partial absorption, which are determined by the data in the 2.5–4, 7–10, and 50–80 keV energy ranged (Walton et al. 2014).

4.3 *NuSTAR* Data Reduction

Generally, a file format called Flexible Image Transport System (FITS) is used for data handling in X-ray astronomy. A FITS file consists of a header and a table. The header contains observational information, including the observation date, the attitude of telescope or spacecraft, and other parameters. The table is a list of photons (or events), in which each photon is tagged with the sky coordinate, the arrived time, the energy (converted from pulse height via response files), and other information. The FITS format thus enable us photon-by-photon analysis. In analyses of the *NuSTAR* and *Suzaku* data, we used a software package, HEAsoft (version 6.20), developed by NASA to handle the FITS files,

The left panel of figure 4.2 shows an X-ray image of Swift J2127.4+5654 obtained on 2012/11/04, made by using position information in a FITS file. As shown there, the on-source events were extracted from a circular region with a radius of 100″. The background

region was chosen to be an annular region on the same detector as the source. The FPM responses (§3.1.2) change to some extent among observations due to attitudes of *NuSTAR*. Therefore, for each observation, we produced the response matrices and the ancillary response files (§3.1.2) using `numkrmf` and `numkarf` in HEAsoft, respectively.

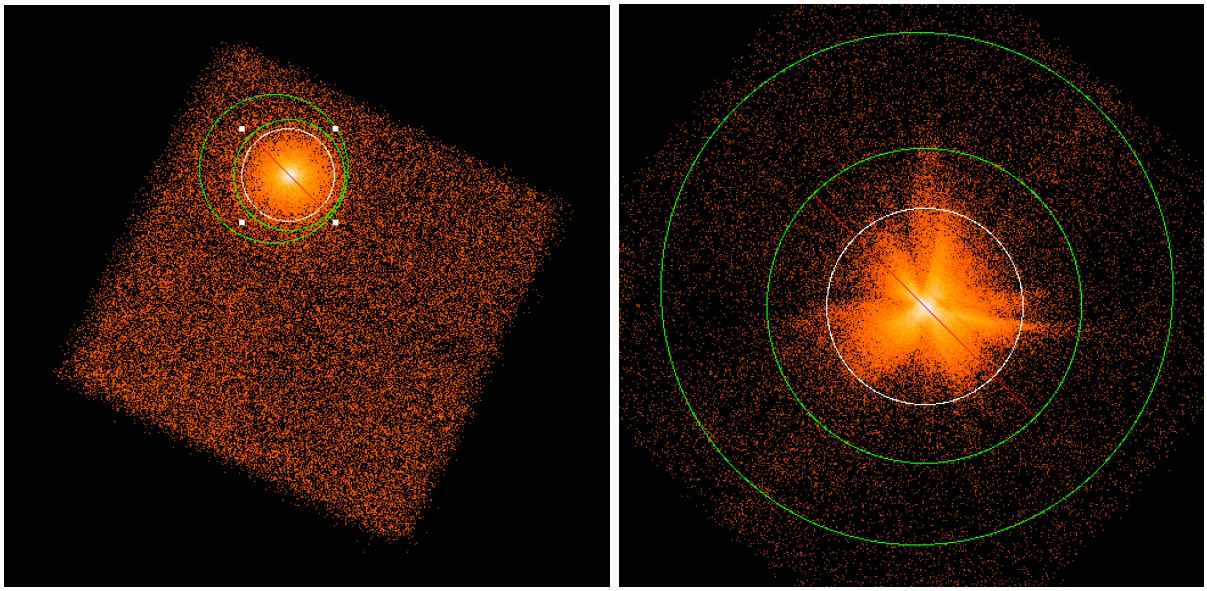

Figure 4.2: (left) An X-ray image of Swift J2127.4+5654 taken on 2012/11/04 with *NuSTAR* FPMA. (right) The same as the left panel but of NGC 4051 on 2008/11/06 with *Suzaku* XIS0. Source regions (white) and background regions (green) are indicated.

By extracting X-ray events from the source and background regions defined in this way, and using their energy information, we obtain spectra as exemplified in figure 4.3. Because of the energy-dependent effective area of the FPM (§3.1.3), they rises from $\sim$ 3 keV and gradually fall above $\sim$ 10 keV. The fluorescence emission lines from CsI at $\sim$ 30 keV (same as in figure 3.5) disappear after subtracting the background.

Finally, light curves are made from the timing information of individual photons. As shown in figure 4.4 as an example, such a light curve usually suffers quasi-periodic data gaps, which are caused by the following three particular locations of the spacecraft around the Earth. One is the South Atlantic Anomaly (SAA), where the Earth's inner Van Allen belt is closest to the Earth, so that the radiation background is too high for any detector to detect celestial X-rays. Another is regions with low cutoff rigidity, mostly in regions of high geomagnetic latitude, where cosmic rays with lower energies can penetrate the magnetic barrier. The other is Earth occultation, when the source is behind the Earth, depending on

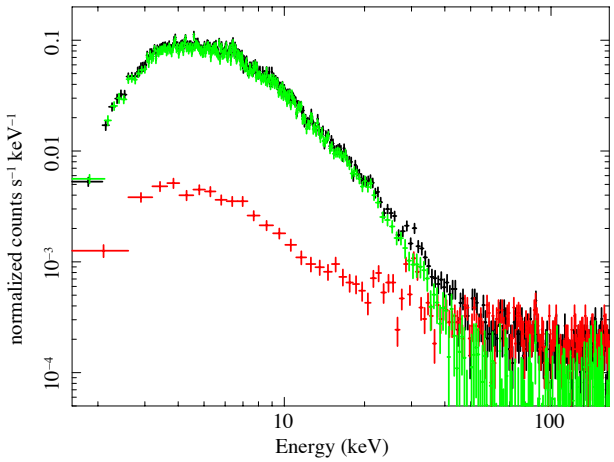

Figure 4.3: *NuSTAR* spectra of Swift J2127.4+5654 from the source (black) and background (red) regions, and the background-subtracted spectrum (green).

the source position in the sky and the spacecraft location around the Earth. After excluding these conditions, we obtained data which can be used for analysis.

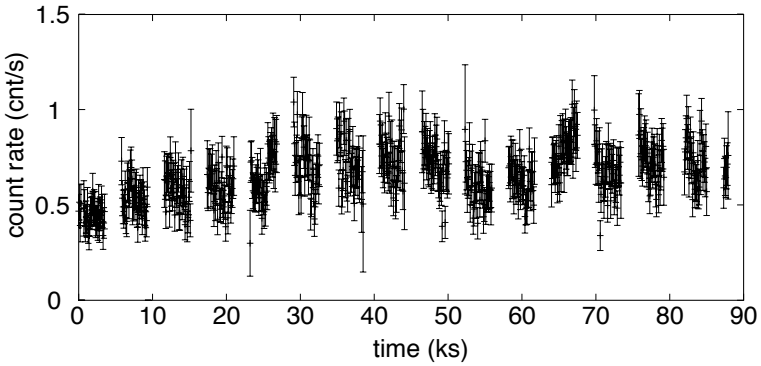

Figure 4.4: A background-subtracted 3–10 keV light curve of Swift J2127.4+5654.

4.4 *Suzaku* Data Reduction

Basically, the *Suzaku* data were processed in the same manner as those of *NuSTAR*. We analyzed public data of XIS 0, XIS 3, and HXD-PIN. The events from XIS 0 and XIS 3 were co-added, and are collectively called XIS-FI events. As shown in 4.2 (right), the on-source events were extracted from a circular region with a radius of 3′, and the backgrounds were

from an annular region with inner and outer radii of $4'.8$ and $7'.8$, respectively. The response matrices and the ancillary response files were generated by `xisrmfgen` and `xissimarfgen` in HEAsoft (Ishisaki et al. 2007), respectively.

In contrast to the *NuSTAR* FPM and the *Suzaku* XIS, the *Suzaku* HXD (§3.2.4) is a non-imaging detector, and has no offset detectors. As a result, the HXD data lack real-time background (especially NXB; §3.2.4) information. Therefore, we subtracted the NXB and the CXB modeled by Fukazawa et al. (2009) (§3.2.4) and Boldt (1987).

Chapter 5

ANALYSIS AND RESULTS OF THE *NuSTAR* DATA

In this Chapter, we analyze the *NuSTAR* data of our final sample (table 4.2), 11 data sets of four NLS1s, through the procedure described in §4.3.

5.1 Swift J2127.4+5654

5.1.1 Description of the object

Swift J2127.4+5654 is one of the brightest and most variable NLS1s with $z = 0.0144$ (Sazonov et al. 2007). It has a SMBH mass of $M_{\rm BH} = 1.5 \times 10^7 M_\odot$ (Malizia et al. 2008), which translates to the the gravitational radius of $r_{\rm g}/c = 75$ s (§2.1.5). This source is located at a low Galactic latitude at $\sim 4.4°$, so that its host galaxy had not been catalogued in the optical, until it was first identified by the *Swift*/BAT as a hard X-ray source (Tueller et al. 2005). Figure 5.1 shows optical and X-ray images of this AGN, in comparison with the typical NLS1 Ark 564. The host galaxy of Swift J2127.4+5654 is highly obscured, whereas the spiral galaxy hosting Ark 564 is clearly seen in the optical. By subsequent optical spectroscopy, Swift J2127.4+5654 was classified as an NLS1. This object was also detected in X-rays with the *INTEGRAL*/IBIS, and its cutoff energy $E_{\rm c}$ was determined as $\lesssim 50$ keV (e.g. Malizia et al. 2008; Panessa et al. 2011).

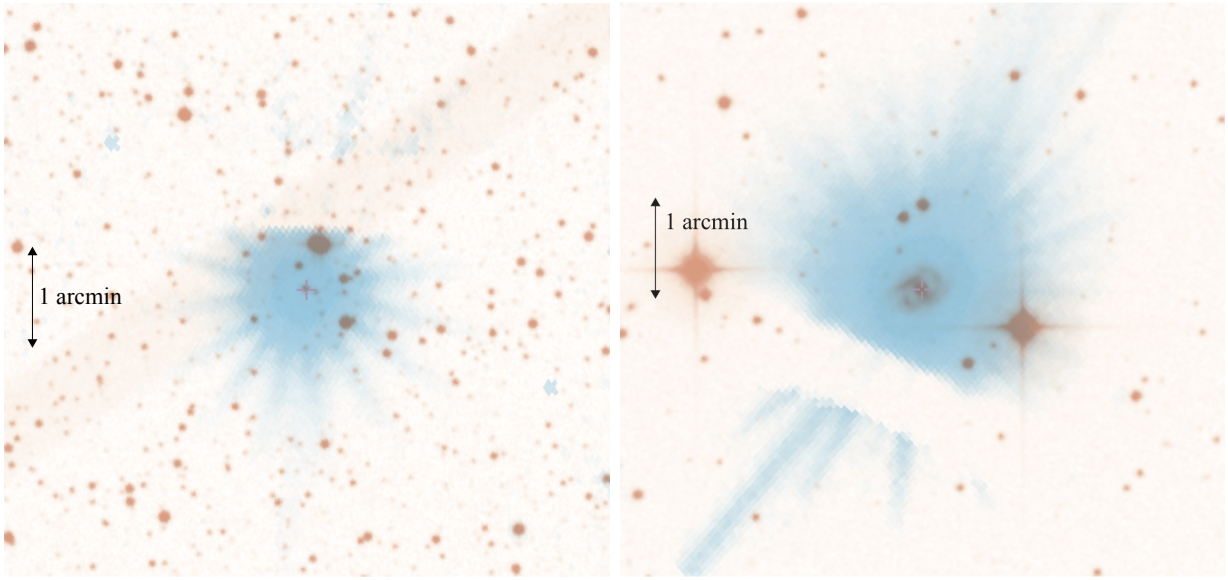

Figure 5.1: (left) Optical (red) and X-ray (blue) images of Swift J2127.4+5654. The former is taken from the Digital Sky Survey, and the latter from the *XMM-Newton* EPIC PN. (right) The same as the left panel but of Ark 564.

5.1.2 Light curves

The top panel of figure 5.2 shows light curves of Swift J2127.4+5654 from all *NuSTAR* data combined. The count rate changed by a factor of ~ 1.5 within ~ 10 ks, and also by ~ 1.5 among the observations. The variations in 10–50 keV were closely correlated with those in 3–10 keV, with comparable amplitudes. This suggests that the source varied with its spectral shape approximately kept constant.

Figure 5.3 shows a CCP (count-count plot; §2.3) between 3–10 keV and 10–50 keV. As suggested by the light curves, the variations in these energy bands are reasonably well correlated, with the correlation coefficient of 0.902. The fit with a single line was however not so good, with $y = 0.331x + 0.0422$ and $\chi^2/\mathrm{d.o.f.} = 165.5/114$, because of scatter of the data points. From the CCP, we can see three types of variations. One is the variation along the fitted line; this evidently represents the color-conserved variations on time scales of ~ 10 ks, which dominate the light curves (figure 5.2). Another is the clear offset in the 10–50 keV rate, which suggests the presence of some non- (or weakly-) varying signals in hard X-rays; from the energy range, this cannot be soft X-ray contamination from the host galaxy, or from the foreground Milky Way. The other is the small but statistically significant scatter

of the data points around the fitted line; this suggests the presence of some color-changing effects. Actually in the CCP, the data on 2012/11/04 and 11/08 tend to be distributed lower than the fitted line, while those on 11/05 and 11/06 higher. This is also confirmed in hardness ratios shown in the bottom panel of figure 5.2. The spectrum was thus softer on 2012/11/04 and the latter half of 11/08, while harder on 11/05 and 11/06. Figure 5.3 (right) shows a scatter plot between the 3–10 keV intensity and the hardness ratio, where the two quantities do not show strong correlation, with the correlation coefficient of -0.33. Therefore, the hardness variations were not synchronized with the intensity variations. This agrees with the CCP (figure 5.3 left), where the data points scatter rather randomly around the straight line; the CCP would exhibit a curved distribution if the hardness ratio were correlated with the intensity.

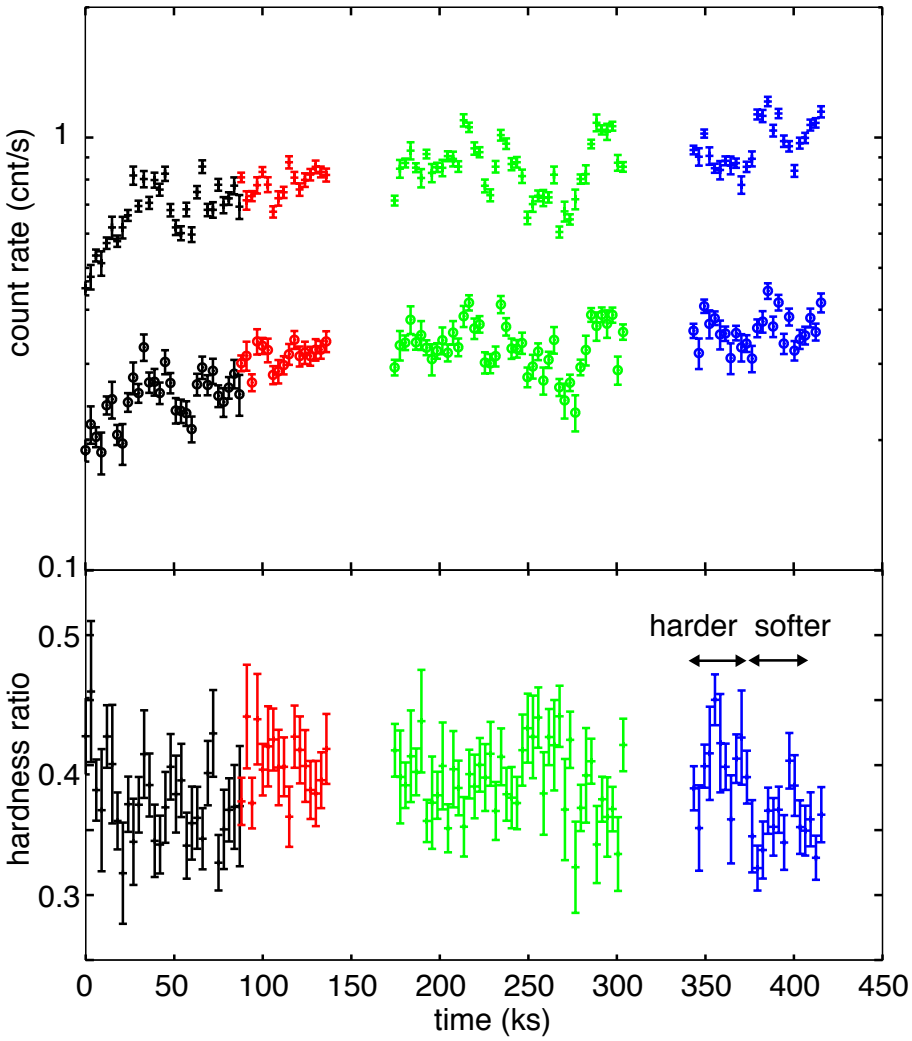

Figure 5.2: (top) Background-subtracted light curves of Swift J2127.4+5654 in the 3–10 keV (cross) and the 10–50 keV (open circle) energy ranges. Colors specify the data acquired on 2012/11/04 (black), 11/05 (red), 11/06 (green), and 11/07 (blue). Each bin is 3 ks long. (bottom) Hardness ratios between the 3–10 keV and 10–50 keV energy bands.

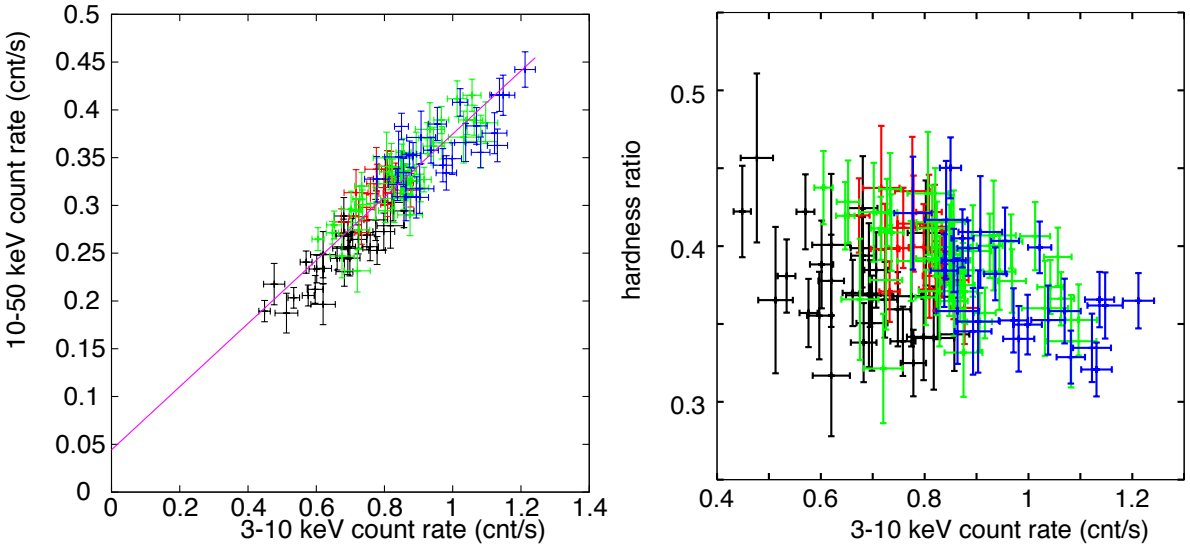

Figure 5.3: (left) A CCP between 3–10 keV and 10–50 keV on 2012/11/04 (black), 11/05 (red), 11/06 (green), and 11/08 (blue), fitted with a common straight line (magenta). (right) The hardness ratio plotted against the 3–10 keV rate, colored as in the left panel.

5.1.3 Spectra

Figure 5.4 shows background-subtracted X-ray spectra, produced as described in §4.3 by averaging over the individual observations. By dividing them by a response-folded PL with $\Gamma = 2$, the instrumental effects are approximately removed, and the presentation is made similar to an νF_ν plot. The spectra exhibit a PL-shaped continuum, an Fe K line at $\sim$ 6.3 keV, a hard X-ray hump at $\sim$ 20 keV, and a cutoff at $E_c > 30$ keV. These spectral shapes are typical of AGNs. The narrow Fe K line and the hard X-ray hump suggests the presence of a distant reflection component (§2.2.2), which must work as stationary signals.

The right panel of figure 5.4 shows ratios of the spectra to their average. The good flatness of the ratios below 10 keV means that the spectral shape below $\sim$ 10 keV is conserved as the source varies. In contrast, the spectral shape above $\sim$ 10 keV is inferred to vary weakly among the four observations. Especially on 2012/11/05 (red) and 11/06 (green), the 20–50 keV flux is relatively higher, in agreement with the behavior of the hardness ratio (figure 5.2). We hence find that the source variability is mainly carried, like in other AGNs, by a PL with $\Gamma \sim 2$, which is regarded as a primary component, but some additional effects produce the slight change in the spectral shape.

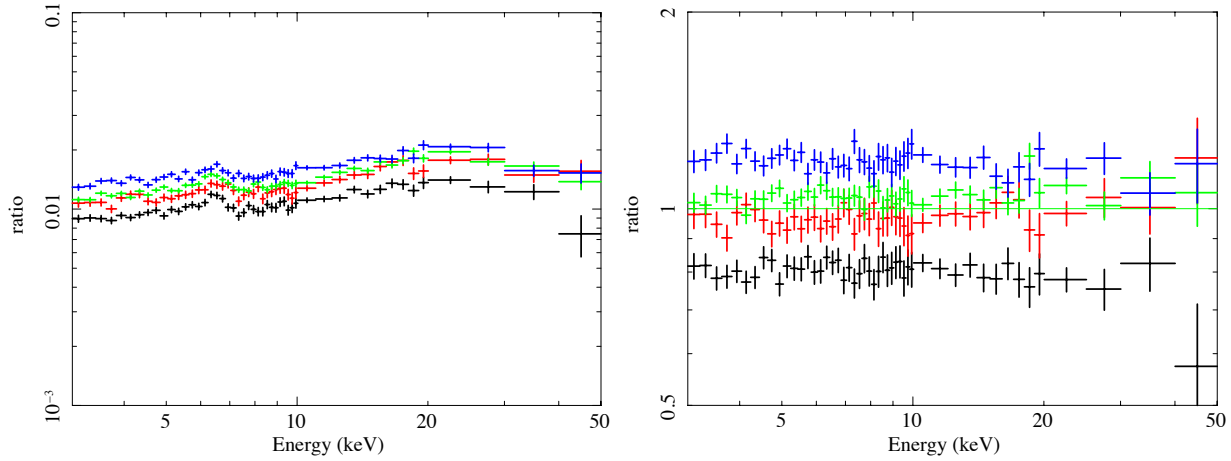

Figure 5.4: (left) Background-subtracted spectra of Swift J2127.4+5654, shown in the form of their ratios to a PL with $\Gamma = 2$ and a normalization of 1 ph cm^{-2} s^{-1} keV^{-1}. (right) Ratios to a spectrum averaged over all the four observations. In both panels, data were obtained on 2012/11/04 (black), 11/05 (red), 11/06 (green), and 11/07 (blue).

To further examine the variability of the X-ray spectral shape, the root mean square (RMS) variation is shown in figure 5.5. The results do not show clear differences among

the observations. Although the RMS variation is thus approximately energy independent, it shows some decrease in the 10–20 keV band. This behavior can be understood to be caused by the distant reflection hump (§2.2.2), which is known to vary only on very long time scales of ~ 1 year.

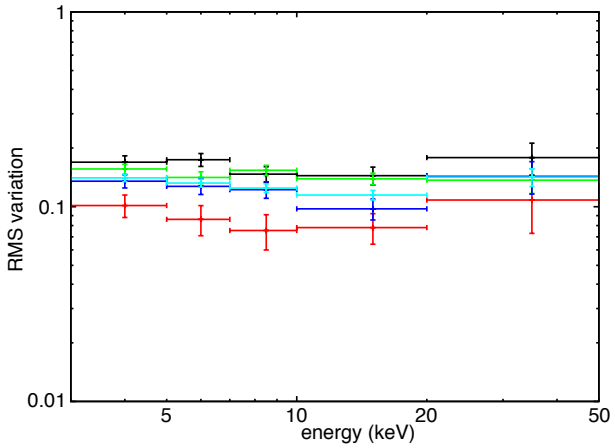

Figure 5.5: The RMS variations on 2012/11/04 (black), 11/05 (red), 11/06 (green), and 11/07 (blue), and their average (cyan), shown as a function of X-ray energy.

From these examinations, we infer that the color-conserved variations, which dominate in the CCP (figure 5.3 left), are produced mainly by the $\Gamma \sim 2.1$ PL as it changes the intensity with its shape kept constant. Then, what is responsible for the color-changing variations? It can be explained by three alternative ways. One is variations of the PL shape, or Γ; supposing that this PL component arises via thermal Comptonization (§2.2.1), its Γ would generally decrease (flatten) if its intensity increase is caused by those of the density or $T_{\rm e}$ of the Comptonizing hot electrons, whereas Γ would increase slightly due to electron cooling if the PL intensity increase is due to an increase of the seed photon number. However, as shown in figure 5.3 (right), the intensity variations are not correlated with those of the hardness; a fine tuning would be needed among $T_{\rm e}$, the electron density, and the seed-photon flux, in order for the spectral slope to change without accompanied by correlated intensity variations. Namely, it would be unnatural to assume that the physical parameters determining the PL shape, τ and $E_{\rm c}$ of the assumed Comptonization process (§2.2.1), vary independently of the flux. Another is to invoke some reprocessing of the primary PL, such as partial covering absorption (§2.2.3), or relativistic reflection (§2.2.2). Although these reprocessed signals can indeed have a different hardness, they are considered to show basically the same variability as the primary PL. Therefore, this alternative is not likely, either. We are hence left with

the last possibility, that is, the presence of another primary continuum component that has a different shape from, and varies independently of, the dominant $\Gamma = 2$ primary. Based on this interpretation, the scatter in the CCP can be considered to be a superposition of the variations of the two distinct primary emissions that are characterized on the CCP as two lines with slightly different slopes. In other words, there are two independent vectors on the CCP, and their linear combination makes the scattered distribution. Below, this interpretation is adopted as a working hypothesis.

5.1.4 Difference spectra within the observations

Given the inference made in §5.1.3, we attempt to decompose the spectrum into the different components using time variability. This may be carried out in several ways, such as the difference spectrum method, the principal components analysis (PCA), and the C3PO method developed by Noda et al. (2013a) as described in §2.3. Because this object shows two independent variations, color-conserved and changing ones, we cannot use the C3PO method which works basically when the spectrum consists of a single variable component and non varying signals. Although the PCA enables us to extract independently-varying components in the form of eigenvectors (e.g. Parker et al. 2015), the results do not usually lead to unique physical interpretations. Therefore, we adopted the difference spectrum analysis, which provides a very powerful way of spectral decomposition when the emission is a linear superposition of multiple components that vary without strong shape changes (e.g. Mitsuda et al. 1984; Makishima et al. 1989), as suggested for Swift J2127.4+5654.

To conduct the difference spectrum analysis, we first divided each observation, as in §4.2.2. Figure 5.6 reproduces the 3–10 keV light curve on 2012/11/06, on which the average count rate of 0.85 cnt s^{-1} is indicated. The observation was thus divided into high and low phases, with the exposures of 31 ks and 25 ks, respectively. In this way, we produced a pair of spectra, one from the high phase and the other from the low phase, and took their difference to obtain a difference spectrum.

Figure 5.7 shows all four difference spectra, one from each observation. They exhibit a similar shape, approximated by a PL with $\Gamma \sim 2.1$ and a cutoff at $E_c \sim 50$ keV, and no longer bear the hard X-ray hump. In addition, the difference spectra are somewhat softer than their parent spectra, implying that the variation is slightly stronger in soft X-rays. This agrees with the decrease of the RMS variation in figure 5.5 from 3 keV to 10 keV.

To quantify the difference spectra, we fitted them with a single PL. The fit to each difference spectrum was successful, and yielded $\Gamma = 2.2 \pm 0.2$ (2012/11/04), 2.1 ± 0.3 (11/05), 2.1 ± 0.1 (11/06), and 2.1 ± 0.1 (11/08). To better constrain Γ, we fitted the four spectra simultaneously with a PL having a common Γ. Figure 5.8 shows the fit to all the difference spectra with a PL with common Γ. They were well reproduced ($\chi^2/\mathrm{d.o.f.} = 20.2/30$ summed over the four spectra) by a single PL with $\Gamma = 2.07 \pm 0.07$. In this way, the color-conserved variable component has been identified as a PL with $\Gamma = 2.1$. Since the slope of $\Gamma = 2.1$ is somewhat softer than that of the time-averaged spectra (either high or low phase), we hereafter call this component "a variable soft PL component", or simply, "a soft PL".

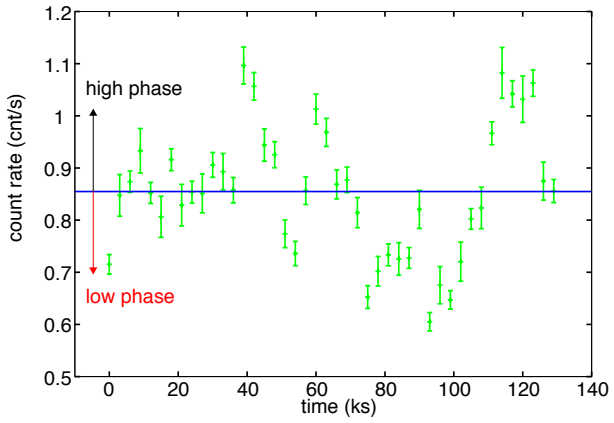

Figure 5.6: The same 3–10 keV light curve on 2012/11/06 (green) as that in figure 5.2, and the average count rate (blue). The high and low phases are defined.

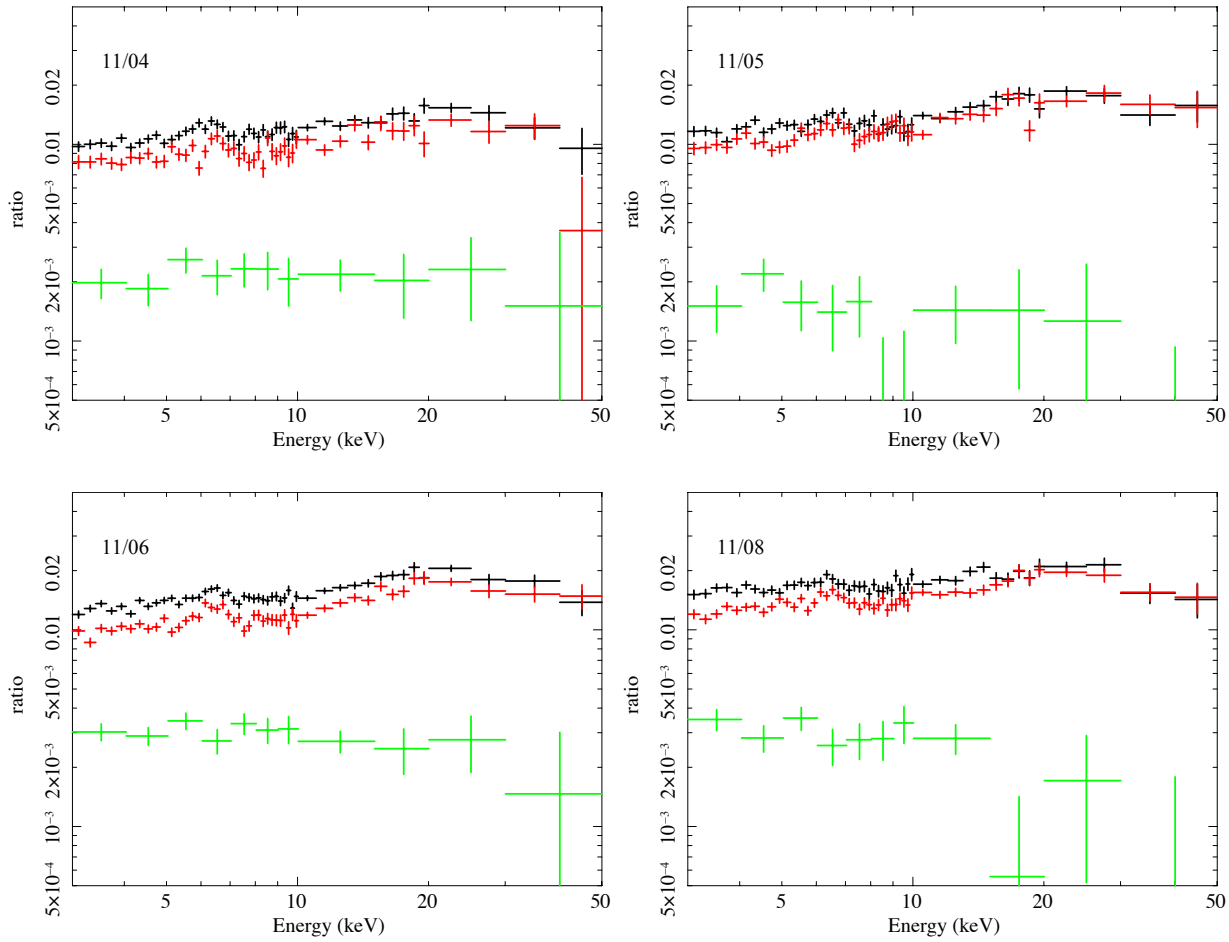

Figure 5.7: The spectra in the high (black) and low (red) phases, and the difference spectra between them (green), shown in the form of their ratios to a PL with $\Gamma = 2$ and a normalization of 1 ph cm^{-2} s^{-1} keV^{-1}.

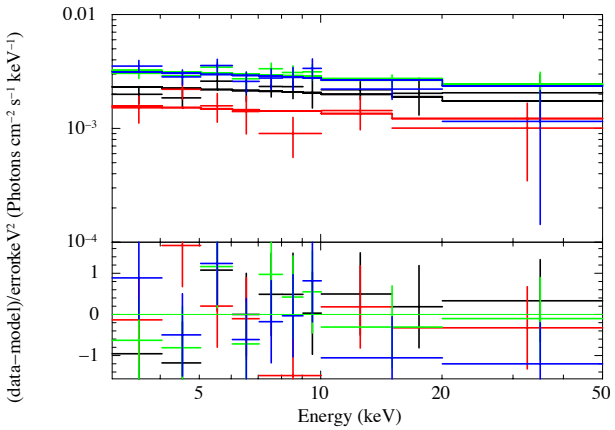

Figure 5.8: The difference spectra within the observations on 2012/11/04 (black), 11/05 (red), 11/06 (green), and 11/08 (blue). They were individually fitted with a PL, of which Γ is constrained to be the same.

5.1.5 Difference spectra among the observations

Given the consideration of §5.1.4, our next task is to identify the spectral component responsible for the color-changing variation. One way of doing this is to take a difference when the source was hard and soft. Figure 5.9 (top left) reproduces the 3–10 keV light curves, where the colors specify time intervals when the source is more than $+1\sigma$ above (blue) and more than -1σ below (red) the line fitted to the CCP in figure 5.3. The excluded data points, lying within statistical $\pm1\sigma$ of the linear fit in figure 5.3, are indicated in figure 5.9 (top left) in black. Figure 5.9 (top right) shows the spectra in softer and harder time intervals, accumulated over the four observations, and their difference. The difference spectrum is indeed very hard, and this property is considered to mainly reflect the intrinsic slope change (which is statistically significant; §5.1.2) rather than Poisson fluctuations, because of the $\pm1\sigma$ exclusion. It is approximately reproduced by a PL with $\Gamma = 1.4 \pm 0.3$, while the < 10 keV band suggests the presence of absorption.

Although we have thus obtained some hint on the color-changing variation, the difference spectrum in figure 5.9 suffers very poor statistics, because the spectrum changes only slightly in its slope (figure 5.3 left) and about $\sim 1/2$ of the data points were discarded (figure 5.9 top left). Therefore, as another approach to the same issue, differences *among* the four observations may be considered. As shown in figure 5.2 and figure 5.9 (top left), the hardness remained low almost throughout on 2012/11/04. Accordingly, we made another set of difference spectra by selecting the observations on 2012/11/05, 11/06, and 11/08 as high phases, and that on 11/04 as low one to be subtracted. Figure 5.9 (bottom) shows three difference spectra made in this way. They exhibit a harder component above ~ 10 keV, while the 3–10 keV band is still dominated by the soft PL. We fitted these difference spectra simultaneously with a model consisting of two PLs. One is the soft PL with $\Gamma = 2.1$ (fixed). The other is a harder PL, of which Γ is free but constrained to be the same among the spectra. The normalizations of the two PL components were allowed to vary freely for each spectrum. The fit was successful with $\chi^2/\mathrm{d.o.f.} = 35.9/38$, and the best-fit parameters are shown in table 5.1. The hard PL has been found to have $\Gamma = 1.2 \pm 0.4$. In addition, the hard PL has been suggested to be less variable than the soft PL, because the hard-PL normalization in table 5.1 is consistent with being constant (within rather large errors), whereas that of soft PL varied by a factor of ~ 4 among the three spectra.

Let us further examine the spectral shapes of the two PLs obtained so far. We averaged the four difference spectra in figure 5.8 to make one difference spectrum, labeled [A]. In the same way, a difference spectrum labeled [B] was made by averaging the three difference spectra in figure 5.9 (bottom). Figure 5.10 shows the difference spectra [A] and [B], representing

Table 5.1: The best-fit parameters to the three difference spectra among the observations[†].

		11/05	11/06	11/08
soft PL	Γ	2.1 (fixed)		
	norm*	$1.2^{+0.6}_{-1.1}$	$2.2^{+0.6}_{-0.13}$	$4.5^{+0.6}_{-1.4}$
hard PL	Γ	1.2 ± 0.4		
	norm*	$0.2^{+0.63}_{-0.14}$	$0.24^{+0.76}_{-0.17}$	$0.22^{+0.75}_{-0.16}$

[†] The spectrum on 2012/11/04 was subtracted.

* normalization (photons/keV/cm^2/s at 1 keV).

the intra-observation slope change and variations among different observations. We first fitted them with a simple model consisting of two PLs, `phabs[0]*(powerlaw[0]+powerlaw[1])` in XSPEC terminology. The component numbers are specified with `[0]` and `[1]`, and `powerlaw[0]` is a softer PL which contributes to both [A] and [B], with a common Γ but separate normalization, while `powerlaw[1]` is a harder PL, contributing only to [B]. The column density $N_{\rm H}$ of interstellar absorption is taken into account as `phabs[0]`, and was fixed at 2.1×10^{22} cm^{-2}, which was determined by a simultaneous observation with *NuSTAR* and *XMM-Newton* (Marinucci et al. 2014). Cut-off energies of both `powerlaw` are taken into account, and were fixed at 50 keV, based on *INTEGRAL* results by Panessa et al. (2011). The fit result is shown in figure 5.10 (a), and the parameters are summarized in table 5.2. The difference spectrum [A] was well reproduced by `powerlaw[0]`, and the fit itself was statistically acceptable, but spectrum [B], with its characteristic curvature, left systematic residuals at $\gtrsim 20$ keV. In addition, $\Gamma = 0.6 \pm 0.3$ of the harder PL is unphysical. Therefore, we took into account absorption of `powerlaw[1]`, `phabs[1]`, as suggested by figure 5.9 (top right). As shown in figure 5.10 (b), the fit became significantly better because the model well reproduces the curvature of [B] above 20 keV. The harder PL have a reasonable value of $\Gamma = 1.5$. Finally, we replaced `powerlaw[1]` by `Nthcomp` (Zdziarski et al. 1996; Życki et al. 1999), which models a thermally Comptonized continuum, wherein the cut-off appears at $E_{\rm c} = (2\text{–}3) k_{\rm B} T_{\rm e}$. The electron temperature was fixed at $T_{\rm e} = 25$ keV, and the blackbody temperature $T_{\rm in}$ of the seed photons fixed at the typical value of $T_{\rm in} = 10$ eV. As shown in figure 5.10 (c, d), the harder component now requires the additional absorption with a higher statistical significance than in (b). In conclusion, figure 5.10 gives firm evidence that the hard PL is heavily absorbed.

Table 5.2: The best-fit parameters to the difference spectra [A] and [B]. (a–e) correspond to those in figure 5.10.

		(a)	(b)	(c)	(d)
`phabs[0]`	$N_{\rm H}^{\dagger}$	2.1 (fixed)			
`powerlaw[0]`	norm*	3.9 ± 1.0	4.5 ± 1.0	2.9 ± 1.3	4.5 ± 1.1
	Γ	2.23 ± 0.14	2.16 ± 0.15	2.22 ± 0.14	2.16 ± 0.14
	$E_{\rm c}$	50 keV (fixed)			
`phabs[1]`	$N_{\rm H}^{\dagger}$		152^{+192}_{-104}		156^{+196}_{-86}
`powerlaw[1]`	norm*	$0.08^{+0.14}_{-0.05}$	$1.1^{+40.4}_{-1.0}$		
	Γ	0.6 ± 0.3	$1.5^{+1.0}_{-0.7}$		
	$E_{\rm c}$	50 keV (fixed)			
`Nthcomp`	norm*			$0.49^{+0.55}_{-0.25}$	$2.9^{+49.7}_{-2.3}$
	Γ			1.4 ± 0.2	$1.9^{+0.8}_{-0.4}$
	$T_{\rm e}$			25 keV (fixed)	
χ^2/d. o. f.		15.4/17	8.2/16	18.4/17	8.3/16

† in units of 10^{22} cm^{-2}.

* for [B], in units of 10^{-3} ph cm^{-2} s^{-1} keV^{-1}.

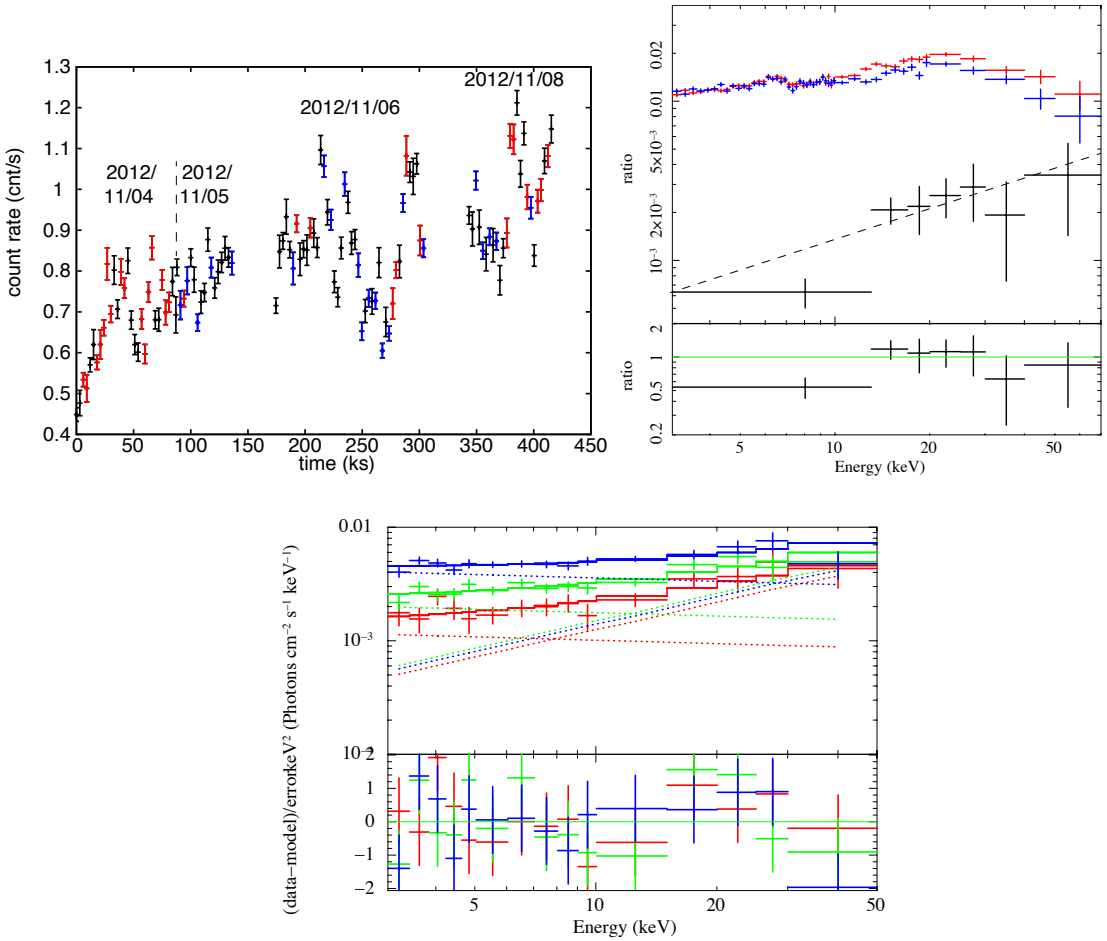

Figure 5.9: (top left) The 3–10 keV light curve of Swift J2127.4+5654, where colors specify harder (blue) and softer (red) phases defined in reference to figure 5.3. (top right) The spectra of the harder (blue) and softer (red) phases, and their spectral difference (black). The difference spectrum is fitted with a PL. (bottom) Difference spectra among the observations. The time-averaged spectrum on 11/04 was subtracted from those on 11/05 (red), 11/06 (green), and 11/08 (blue). The spectra were fitted with a model consisting a $\Gamma = 2.1$ PL and another harder PL, of which Γ is free but constrained to be common to the three spectra.

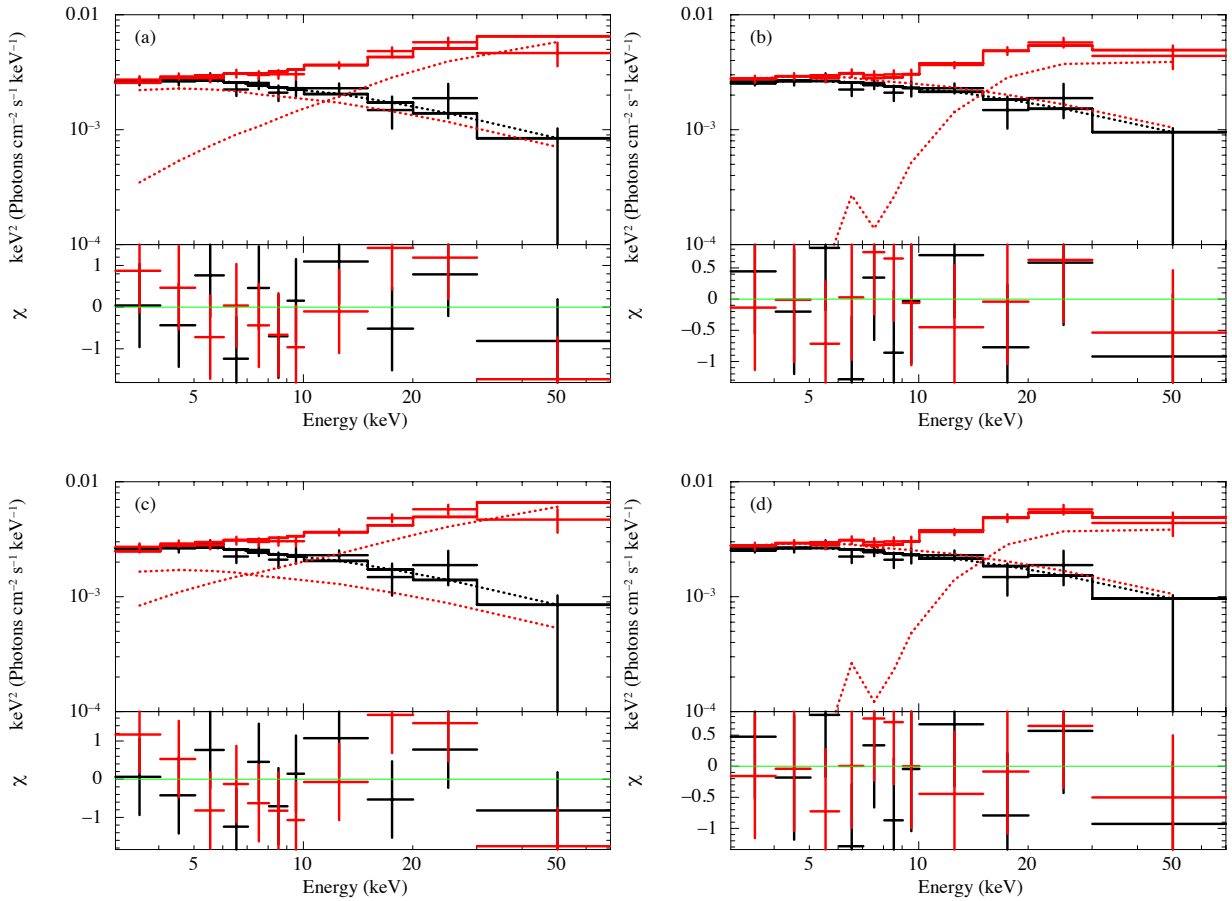

Figure 5.10: Difference spectra [A] (black), within the observations, and [B], among the observations, fitted simultaneously with different models. (a) Two cut-off PLs subject to a common interstellar absorption. The softer of them is assumed to contribute to both [A] and [B] with a common shape, whereas the harder one only to [B]. (b) The same as (a) but the harder PL is further absorbed. (c) The same as (a) but the harder PL is replaced by `Nthcomp`. (d) The same as (c) but `Nthcomp` is absorbed.

5.1.6 Simultaneous fitting to the time-averaged spectra

The studies conducted so far in this thesis suggest that the source variability is carried by the soft and hard PLs. From the narrow Fe line at 6.4 keV, a distant reflection component must also be contributing to the overall emission. Therefore, our next task is to examine whether the time-averaged four spectra can be reproduced by an appropriate linear combination of these three components. We hence adopted a model consisting of a soft PL with a fixed $\Gamma = 2.1$, a hard PL which is subject to absorption as suggested in §5.1.5, and a distant reflection component; it is described as `phabs[0]*(powerlaw[0]+phabs[1]*powerlaw[1]+pexmon[0])` in XSPEC terminology, where `pexmon[0]` models the distant reflection accompanied by Fe and Ni lines. Primary emission of `pexmon` is tentatively regarded as the soft PL.

We conducted simultaneous fitting with the model to the four time-averaged spectra. Based on the treatments, the model parameters are classified into the following three categories.

- Fixed parameters; $N_{\rm H}$ of `phabs[0]` at 2.1×10^{22} cm^{-1} (Marinucci et al. 2014); Γ of `powerlaw[0]` at 2.1; the cutoffs of `powerlaw[0]` and `powerlaw[1]` at 50 keV (Panessa et al. 2011); the abundance of `pexmon[0]` at 1 solar; and the inclination angle of `pexmon[0]` at the typical value of 60°.
- Those left free but constrained to be common among the four spectra; $N_{\rm H}$ of `phabs[1]`; Γ of `powerlaw[1]`; and the normalization of `pexmon[0]`.
- Those allowed to vary freely for individual spectra; the normalizations of `powerlaw[0]` and `powerlaw[1]`.

Figure 5.11 shows results of the simultaneous fit. The observed spectra were well reproduced by the model with $\chi^2/{\rm d.o.f.} = 204.1/185$. The hard PL has $\Gamma = 1.3 \pm 0.1$ in agreement with the results in §5.1.5, and is strongly absorbed with $N_{\rm H} = (8.3 \pm 1.8) \times 10^{23}$ cm^{-1} as suggested by figure 5.9 (top right). The solid angle of the distant reflector is calculated using the normalization of `pexmon` as (0.8–1.2)π which is physically reasonable.

Although the above simultaneous fit has been successful, we have so far fixed Γ of the soft PL at 2.1, based simply on figure 5.8. It would be more realistic to think that the intensity changes of the soft PL is accompanied by some changes in its Γ. So, we repeated the combined fit, allowing Γ of the soft PL to take free values in the individual observations. As summarized in table 5.3, the four spectra all gave a value of Γ that is consistent with the previously assumed 2.1, and the scatter of Γ is at most ± 0.2. Like in many Seyfert 1s (Noda

Table 5.3: The best-fit Γ of the soft PL when they are allowed to vary.

	2012/11/04	2012/11/05	2012/11/06	2012/11/08
Γ	2.03 ± 0.08	2.08 ± 0.10	2.06 ± 0.08	2.06 ± 0.08

2013), Γ of the primary emission of Swift J2127.4+5654 has been found to depend little on the intensity. This is also in agreement with another important observational fact that the photon indices of AGNs are clustered in a rather narrow range around $\Gamma = 2$ (Zhou & Zhang 2010). The constant Γ independent of the soft PL intensity suggests that the intensity variation is caused not by changes of the physical state of the corona but by increase and decrease of seed photons. Although an increase of the seed photons should make $T_{\rm e}$ lower by Compton cooling in such a situation, there may be a feedback mechanism to keep $y \sim 1$ in the corona, and hence $\Gamma \sim 2$. In this way, the employed model are considered to explain the time-averaged spectra in a way that is physically reasonable, and is consistent with the results obtained through the difference spectral analyses.

Now, let us examine whether other models can explain the same set of spectra. Because the photon indices of the two PLs are distinct, the hard PL cannot be a partially covered part of the soft PL, which should have the same Γ and the same variability as the soft PL. Alternatively, we attempted a model in which the hard PL is replaced by a relativistic reflection model, `kdblur*pexmon[1]`, where `kdblur` is a convolution model simulating the relativistic effects (Laor 1991) (§2.2.2). The normalization of `pexmon[1]` was allowed to vary independently of that of `pexmon[0]`. As shown in figure 5.11 (right), the fit was unsuccessful with $\chi^2/\mathrm{d.o.f.} = 828.9/185$, because the model has two problems. One is a too strong emission in 5–7 keV compared to the hard X-ray hump at > 10 keV. The other is an unphysically large solid angle of 5–8π required for `pexmon[0]` and `pexmon[1]` to reproduce the strong hard X-ray hump. These first problem could be mitigated by allowing the reflector's abundance to vary, but then the fit indicates an unrealistically low abundance of 0.5 solar. In this way, the X-ray spectra of the NLS1 can also be explained by considering the two primary PLs.

5.2 Hard Lags of Swift J2127.4+5654

5.2.1 Backgrounds of delay analysis

In some AGNs, we can see time lags between fluxes in different energy bands. For example, Noda et al. (2016) discovered that optical variations in the Seyfert 1 NGC 3516 are delayed

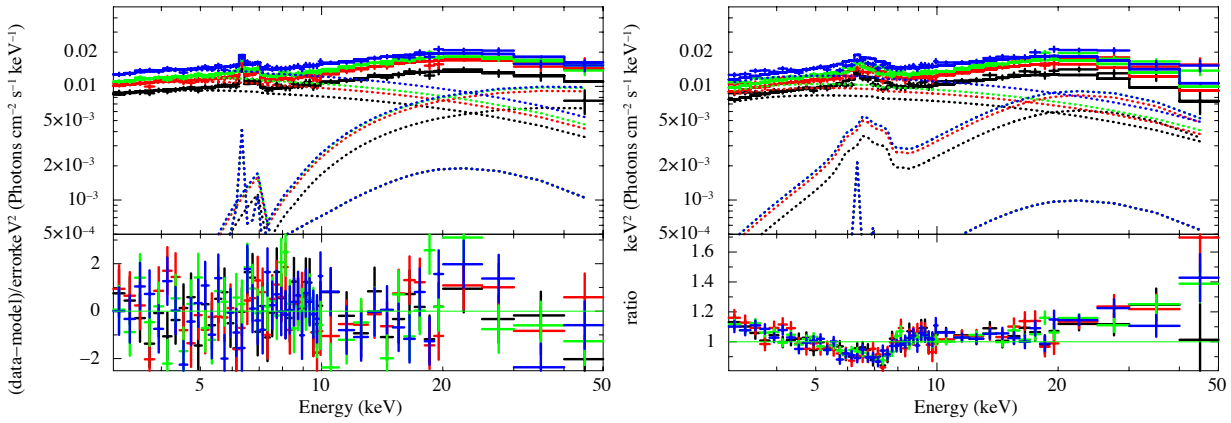

Figure 5.11: (left) Results of the simultaneous fit to the four time-averaged spectra of Swift J2127.4+5654 (with the same colors as in figure 5.4), employing a model consisting of two (soft and hard) PLs and distant reflection. Some of the model parameters are common among the four spectra (see text for details). (right) The same as the left panel but the hard PL is replaced by relativistic reflection.

by ~ 2 days from those in X-rays; this "soft lag" is interpreted as the light travel time from the X-ray emission region to an X-ray illuminated region that produces optical variations. If we instead observe harder photons to lag behind softer ones, or "hard lag", several different interpretations can be considered. The most straightforward one is that the delay reflect the time needed for the accreting matter to fall from the region emitting the softer photons to that producing the harder ones. An alternative possibility is inverse Compton scattering, in which softer photons are boosted into higher energies as scattered many times by higher energy electrons. Yet another is reflection of the soft PL, wherein the delay again represent the light travel time like in the soft lag in NGC 3516, but the effect appears as a hard lag because the reprocessing in this case hardens X-ray spectrum due to photoelectric absorption. The time delay hence may give us information about geometry of the two distinct PLs.

From Swift J2127.4+5654, hard X-ray lags have been discovered (Kara et al. 2015). Figure 5.12 shows the energy dependence of the lag with respect to 4–5 keV signals, calculated at two different frequencies. The high-frequency lag of 400 s ($\sim 5r_{\rm g}/c$, calculated using $M_{\rm BH} = 1.5 \times 10^7 M_\odot$ and $r_{\rm g}/c = 75$ s ; §5.1.1) is considered to be typical of NLS1s, because similar delays were confirmed in the NLS1s, Ark 564 and Mrk 335 (e.g. Kara et al. 2013). From the timescales, they can be considered as due to X-ray reflection by an accretion disk. However, the low-frequency lag by ~ 6 ks ($\sim 80r_{\rm g}/c$) has remained unexplained, because

it is too long for that interpretation, while too short to be considered as reflection from a torus.

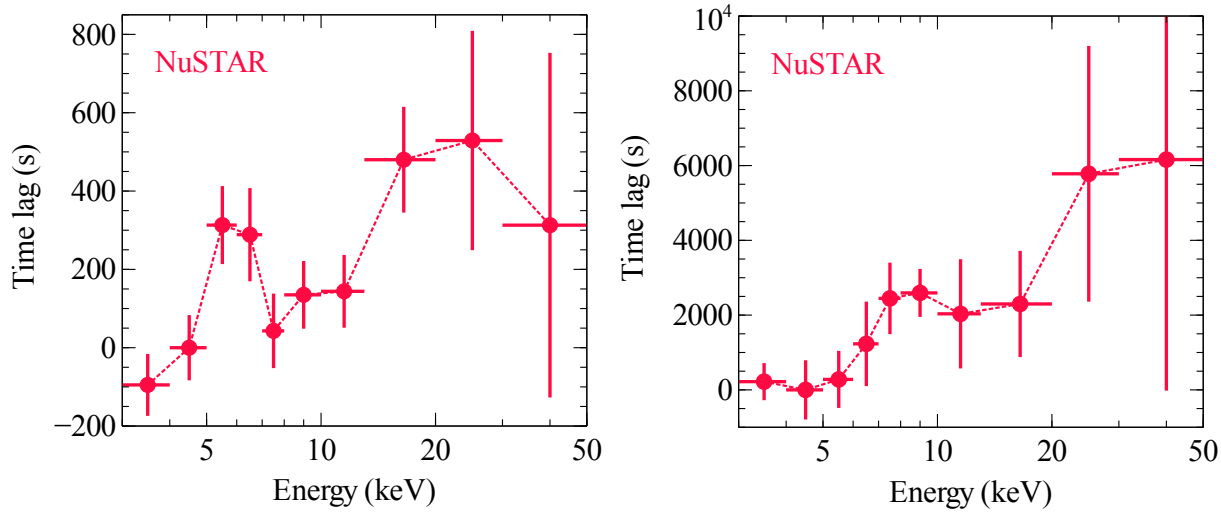

Figure 5.12: High- (left; $> 0.4 \times 10^{-4}$ Hz) and low-frequency (right; $< 0.4 \times 10^{-4}$ Hz) lag-energy spectra for Swift J2127.4+5654, taken from Kara et al. (2015). The lag is calculated against the 4–5 keV signals.

5.2.2 Running average

In the present data of Swift J2127.4+5654, the hard X-ray flux was well correlated with the soft one (figure 5.2), and we cannot directly see a clear lag. However, this could be due to Poisson errors. To suppress them, Fourier filtering would be useful. As an easier alternative way, we adopted running average. That is, specifying the smoothing data length n, the i-th data x_i is re-calculated as

$$x_i = \sum_{j=i-\frac{n-1}{2}}^{i+\frac{n-1}{2}} \frac{x_j}{n}. \tag{5.1}$$

Figure 5.13 shows the same 3–10 keV and 10–50 keV light curves of Swift J2127.4+5654 as in figure 5.2, but smoothed with running averages of $n = 3$ and 5. Now, we notice several occasions wherein the 10–50 keV variations are delayed behind those in 3–10 keV, by several ksec. This hard lag is likely to be the same phenomenon as observed previously by Kara et al. (2015) using the same data sets of this NLS1. This effect is generally seen in both $n = 3$ and $n = 5$ results. In addition, we notice a hint that the delay is more visible when

the object was in the soft phase in figure 5.9 (top left) than in the hard phase, as indicated by the bottom panel of figure 5.13.

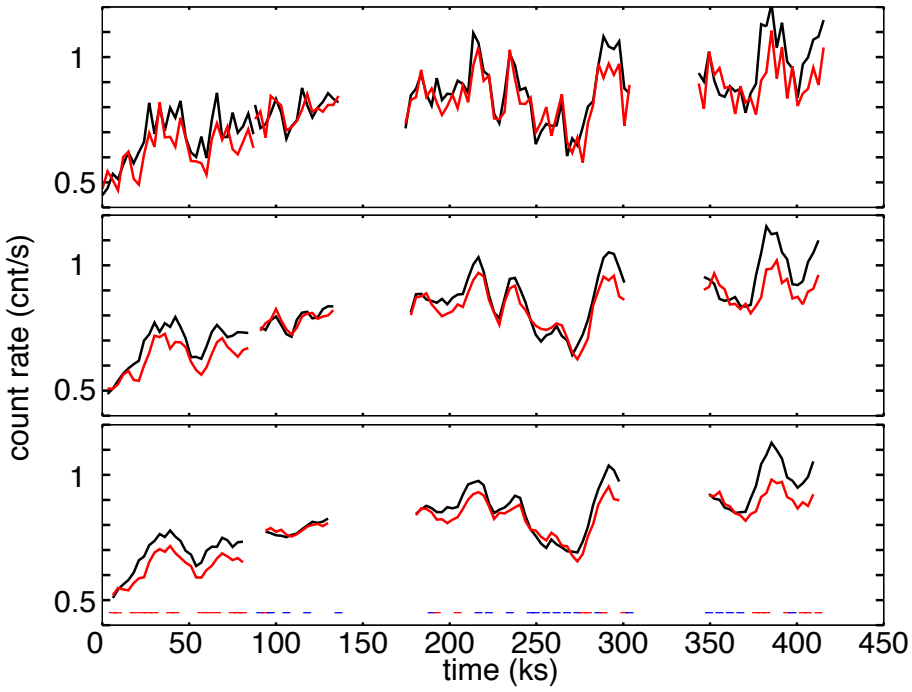

Figure 5.13: (top) The same 3–10 (black) and 10–50 keV (red) light curves with 3 ks bin, as in figure 5.2. (middle) The same as the top panel but running-averaged over 3 data points. (bottom) Averaging over $n = 5$ data points is used instead of $n = 3$. The red and blue ticks in the bottom panel indicate the softer and harder phases of figure 5.9, respectively.

5.2.3 Cross correlation

To quantitatively confirm the suggested delay, we calculated a cross-correlation function (CCF) between 3–10 keV and 10–50 keV, using 512 s binning and excluding those data points where either light curve falls on a data gap. Figure 5.14 shows the CCFs of the four observations, where the strongest peak with a width of $\sim$ 2 ks is seen always at zero lag. This means synchronization between the soft and hard fluxes, and is considered to reflect the variations of the soft PL which contributes significantly to the harder band. In addition, the CCFs on 2012/11/04 and 2012/11/08 reveal a secondary peak at $+6 \pm 1$ ks; this reconfirm the hard lag suggested by figure 5.13, and already detected by Kara et al. (2015).

Although CCFs on 2012/11/04 and 11/08 exhibit the 6 ks hard lag, the effect is not so clear in those on 2012/11/05 or 11/06, when the X-rays were relatively harder (figure 5.2). This supports the inspection of figure 5.13 made above, that the hard lag is observed only when the spectrum is softer (i.e., the hard PL is weaker). To confirm this possibility, we utilized the division of the 2012/11/08 data into the harder and softer phases (figure 5.2), and produced CCFs separately for them. As shown in the bottom of figure 5.14, only the softer-phase CCF shows the 6 ks hard lag. This fact comfirms the correlation between the presence of the 6 ks lag and the hardness. This is our new discovery, which was not noticed by Kara et al. (2015) when they first detected the 6 ks hard lag. The meanings of these phenomena are discussed in §7.2.2.

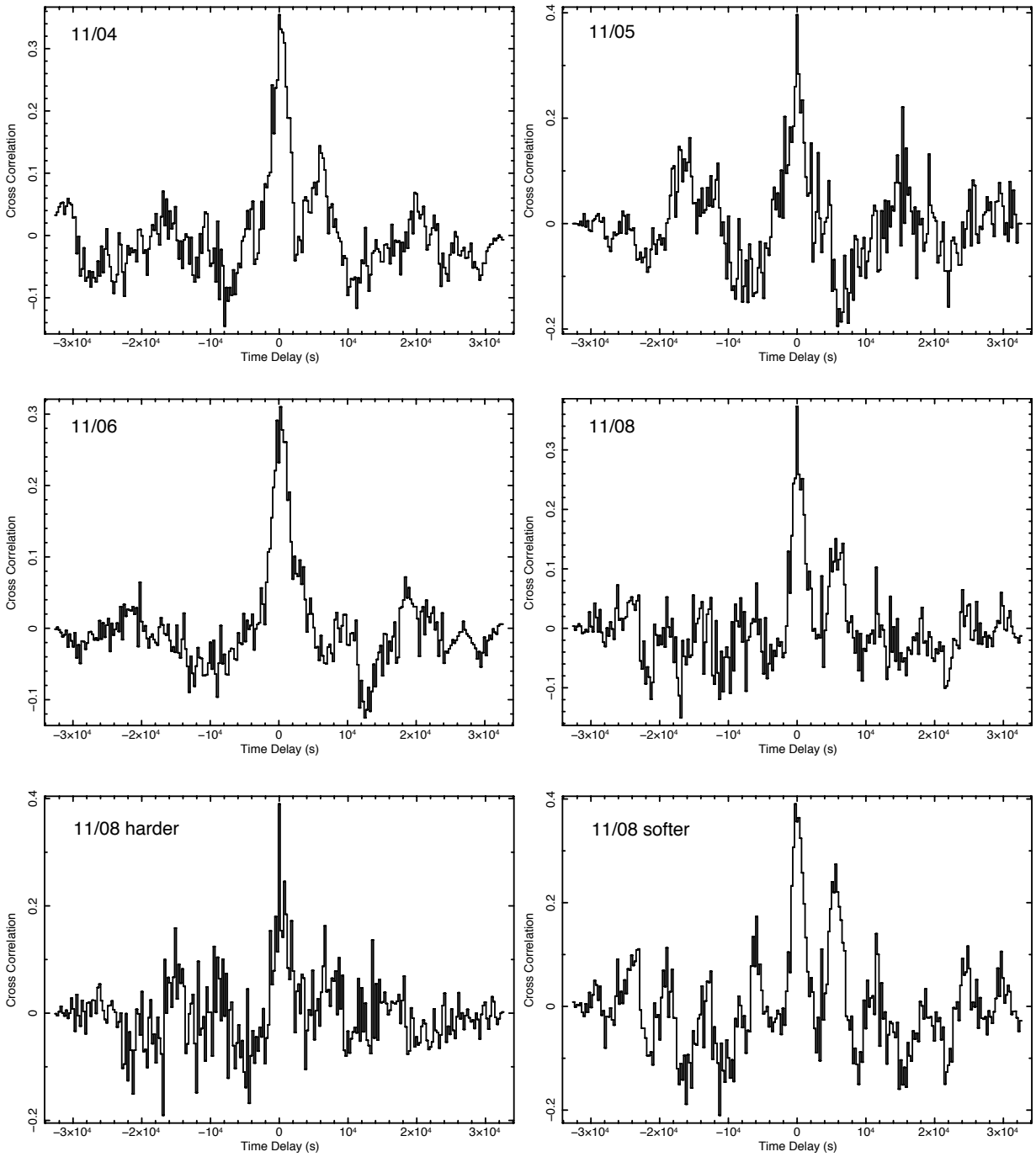

Figure 5.14: CCFs between the 3–10 keV and 10–50 keV count rate, with 512 sec binning, of Swift J2127.4+5654. Positive time delays mean the harder signals lagging behind the softer ones. The first four panels represent the four data sets. The last two panels show the harder and softer phases of 2012/11/08.

5.3 Mrk 766

5.3.1 Description of the object

The bright NLS1, Mrk 766, has the highest accretion rate in our sample with $\eta \sim 0.4$, together with $M_{\rm BH} = 1.26 \times 10^6 M_\odot$ (Giacchè et al. 2014; $r_{\rm g}/c = 6.3$ s) and $z = 0.012929$ (Smith et al. 1987). Its X-rays are known to show high variability. The object was observed by *XMM-Newton* 8 times in 2000, 2001, and 2005, and the spectrum was seen to change in shape. Liebmann et al. (2014) discovered that the X-ray spectra exhibits a weak narrow Fe line when the source is faint, while the Fe line is hidden behind other components when it is bright. They applied difference spectrum analysis to the *XMM-Newton* data, and explained the spectra by a model which involves relativistic reflection. However, these results, obtained using a narrow energy band (0.3–12 keV), could change if we incorporate higher energies (e.g. 10–50 keV). Therefore, to obtain broad-band view of this high-η NLS1, we analyze the *NuSTAR* data of this NLS1, which were explained in §4.2.2.

5.3.2 Light curves

Figure 5.15 shows background-subtracted light curves and the behavior of hardness ratio, recorded in the *NuSTAR* observation. The X-ray count rate changed by a factor of 1.5 during the observation on a typical time scale of ~ 5 ks. The 3–10 keV and 10–50 keV count rates varied simultaneously with almost the same amplitude, so that the hardness ratio was approximately constant. Figure 5.16 shows a CCP of the observation. All the data points can be fitted with a straight line of $y = ax+b$ (with $\chi^2/{\rm d.\,o.\,f.} = 64.4/56$), of which the slope is $a = 0.282 \pm 0.045$, and the offset $b = 0.021 \pm 0.026$. The value of b, which is consistent with zero, means that any stationary emission was not significantly detected within the data statistics. Therefore, the spectrum of Mrk 766 is expected to be reproduced by a primary emission, plus any reprocessed emission that varies synchronized with the primary signals.

5.3.3 Spectra

Figure 5.17 (left) shows the time-averaged spectrum of Mrk 766, which consists of a PL-like continuum, a weak broad Fe line at ~ 7 keV, and a hard X-ray hump at 10–20 keV. It had a similar spectral shape and the comparable 3–10 keV flux of $\sim 2 \times 10^{-11}$ erg cm^{-2} s^{-1} to those in the brighter phases of the *XMM-Newton* observations quoted above (Liebmann et al. 2014). Therefore, it is interesting to examine whether a relativistic reflection model

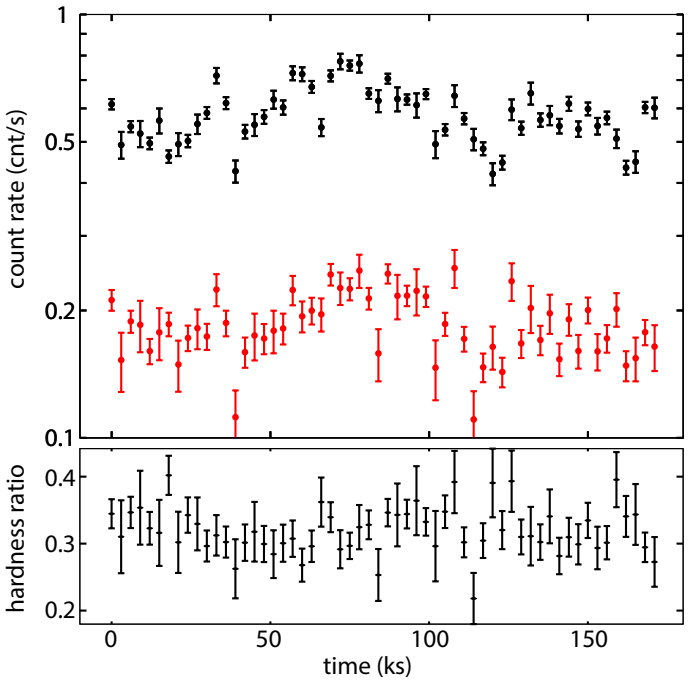

Figure 5.15: (top) Background-subtracted light curves of Mrk 766 in 3–10 keV (black) and 10–50 keV (red). One data bin is 3 ks. (bottom) Hardness ratios between 3–10 keV and 10–50 keV.

can explain the *NuSTAR* data as well.

In the same manner as in §5.1.4, we made the spectra of the high and low phases, to obtain the results shown in figure 5.17. As expected from the CCP, the high-phase and low-phase spectra have nearly the same shape. Actually, the spectral slopes, calculated in the 3–5 keV plus 7–20 keV band are $\Gamma = 2.01 \pm 0.03$ and 1.98 ± 0.03 in the high and low phases, respectively. The difference spectrum between them is also approximated by a single PL, of which the slope of $\Gamma = 2.0 \pm 0.1$ is consistent within errors with those of the high- and low-phase spectra. We fitted the high- and low-phase spectra simultaneously with a model consisting of a PL and its relativistic reflection, `phabs*(powerlaw+kdblur*pexmon)`, in which the two components are considered to vary in intensity while keeping their shapes. This model composition is motivated primarily by the spectral shape (figure 5.17), where the presence of a reflection is indicated. Furthermore, the reflector is suggested to be relatively close to the primary source because the Fe-K line appears to be broad and because the CCP is consistent with $b = 0$ (i.e., the reflection is varying too).

After §5.1.6, we first set the parameters as below.

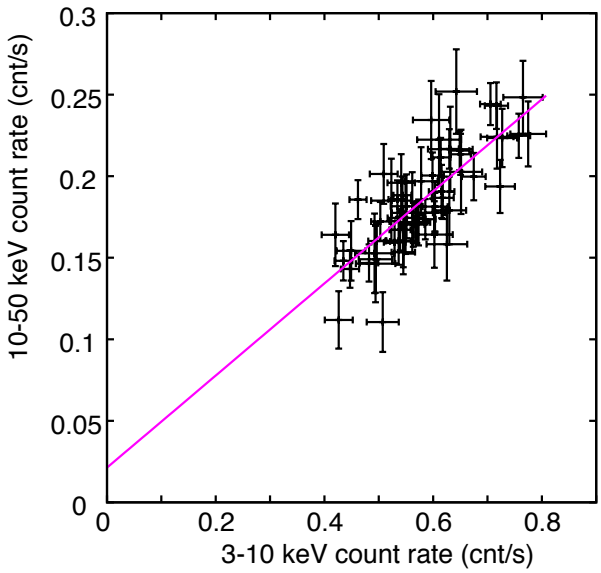

Figure 5.16: A CCP between 3–10 keV and 10–50 keV of Mrk 766, fitted with a straight line (magenta).

- Fixed parameters; the abundance of `pexmon` at 1 solar; the inclination angle of `pexmon` at 60°; and the outer radius of `kdblur` at $400r_{\rm g}$.
- Those left free but constrained to be common among the two spectra; $N_{\rm H}$ of `phabs`; Γ and $E_{\rm c}$ of `powerlaw`; $r_{\rm in}$ of `kdblur`; and the solid angle of `pexmon[0]` (relative normalization to `powerlaw`).
- Those allowed to vary freely for individual spectra; the normalizations of `powerlaw`.

Figure 5.18 (left) shows the fit result, which has been successful with $\chi^2/{\rm d.\,o.\,f.} = 240.1/192$. The PL is soft with $\Gamma = 2.17 \pm 0.05$, which is similar to that of the soft PL of Swift J2127.4+5654, and has $E_{\rm c} > 130$ keV. The reflector is implied to have $r_{\rm in} = 27^{+17}_{-14} r_{\rm g}$ and the common solid angle of $(2.8 \pm 0.6)\pi$. This $r_{\rm in}$ is much larger than the ISCO (§2.1.6), but the longitudinal Doppler effect is still significant, because the Keplerian velocity at $30r_{\rm g}$ amounts to $\sim 0.18c$, which would broaden the Fe-K line typically ~ 1.0 keV in agreement with figure 5.17. The larger solid angle than that of Swift J2127.4+5654 is consistent with considerable contribution by the disk reflection. Because $r_{\rm in}/c \sim 200$ s (§5.3.1) is sufficiently smaller than the time bin of 3 ks of the light curve, it is reasonable to regard that the reflection component varies in synchronization with the soft PL. In short, the model is self consistent.

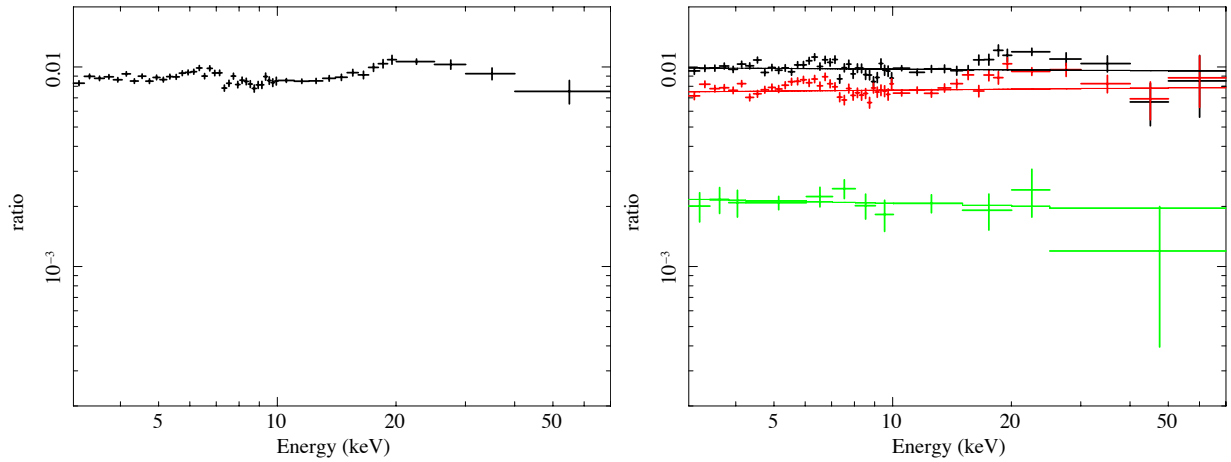

Figure 5.17: (left) The time-averaged spectra of Mrk 766, presented in the same form as figure 5.4. (right) The spectra of the high (black) and low (red) phases of Mrk 766, and their difference (green), fitted with a PL (see text for detail).

Next, we left the normalization (absolute intensity) of `pexmon` free but common between the high- and low-phase spectra. The fit χ^2/d. o. f. becomes unacceptable from 240.1/192 to 244.1/192. Therefore, the reflection is suggested to vary following the soft PL.

Finally, we examined the spectra for possible presence of another primary PL. We added to the above models a typical harder PL with $\Gamma = 1.3$, absorbed with $N_{\rm H} = 5 \times 10^{23}$ cm^{-2}, as a stationary component. Its $E_{\rm c}$ was set the same as that of the soft primary. As a result, the upper limit on the hard PL flux in 10–50 keV has been obtained as 1.75×10^{12} erg cm^{-2} s^{-1}, which is 34% of that of the soft PL. We hence conclude that the single PL with $\Gamma = 2.17$ dominates the primary emission from Mrk 766, and its variation is closely followed by the reflection which is weakly relativistic. This make a contrast to the case of Swift J2127.4+5654, in which the two distinct PL primaries are co-existing, and the reflection is distant and non-varying at least on ~ 400 ks.

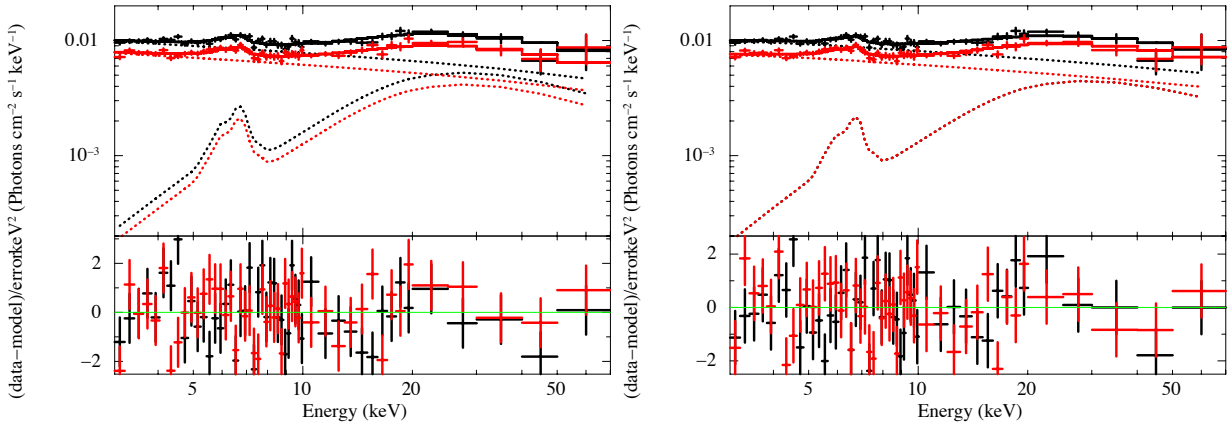

Figure 5.18: (left) The spectra of the high (black) and low (red) phases of Mrk 766, fitted with a model consisting of a PL and a relativistic reflection model, whose relative normalization is made common between the two spectra. (right) The same as the left panel but the absolute normalization of the reflection is constrained to be common.

5.4 Ark 564

5.4.1 Description of the object

Our third target, Ark 564, is a typical NLS1, in the optical, but in X-rays it shows a steep spectrum, and exhibits violent variability. It has $M_{\rm BH} = 2.6 \times 10^6 M_\odot$ (Botte et al. 2004; $r_{\rm g}/c = 13$ s), and $z = 0.0247$ (Huchra et al. 1999). The source is bright, and is one of those which have the highest accretion rates $\eta \sim 0.4$. By observations with the *XMM-Newton* RGS, which has a high energy resolution, a low ionized absorber was found (e.g. Giustini et al. 2015). The *NuSTAR* spectrum, explained in §4.2.2, was found to exhibit a cutoff at 20 keV, and is free from the ionized absorption, which mainly affects the spectrum below ~ 1 keV (Kara et al. 2017). In the present thesis, we analyze the *NuSTAR* data to examine whether the spectrum of this high-η AGN , too, can be described with a single soft primary plus reflection, just as we found for Mrk 766.

5.4.2 Light curves

Background-subtracted light curves in softer and harder energy bands and hardness ratio between them are shown in figure 5.19. Because this object did not have sufficient statistics above 20 keV, the 10–20 keV range was adopted as the harder energy band, instead of 10–50 keV. The X-ray count rates in both bands varied violently on a time scales of ~ 10 ks, including a flare at 295 ks. The hardness ratio is relatively constant at ~ 1.7, but sometimes it decreased to ~ 1.2, particularly in the brightest interval from 200 to 290 ks.

Figure 5.20 shows a CCP between the soft and hard X-rays. It cannot be reproduced by a straight line, with $\chi^2/\mathrm{d.o.f.} = 227.9/139$, because it is bending at the 3–10 keV count rate of ~ 0.8 cnt s^{-1}. Therefore, in the same way as in Swift J2127.4+5654 (§5.1.5), we divided the data into hard and soft phases, as indicated in figure 5.19. The CCPs derived separately from the two phases are shown in figure 5.20 (right) with different colors. Now, the hard and soft phase have been fitted individually by a single line, with $\chi^2/\mathrm{d.o.f.} = 137.5/109$ and $\chi^2/\mathrm{d.o.f.} = 36.2/28$, respectively. This suggests that two distinct components, color-conserved and color-changing ones, are present in X-rays from Ark 564.

5.4.3 Spectra

Figure 5.21 shows the time-averaged spectrum of Ark 564, and the spectra in the soft and hard phases. As already noted in §5.4.1, the time-averaged spectrum of the object is softer

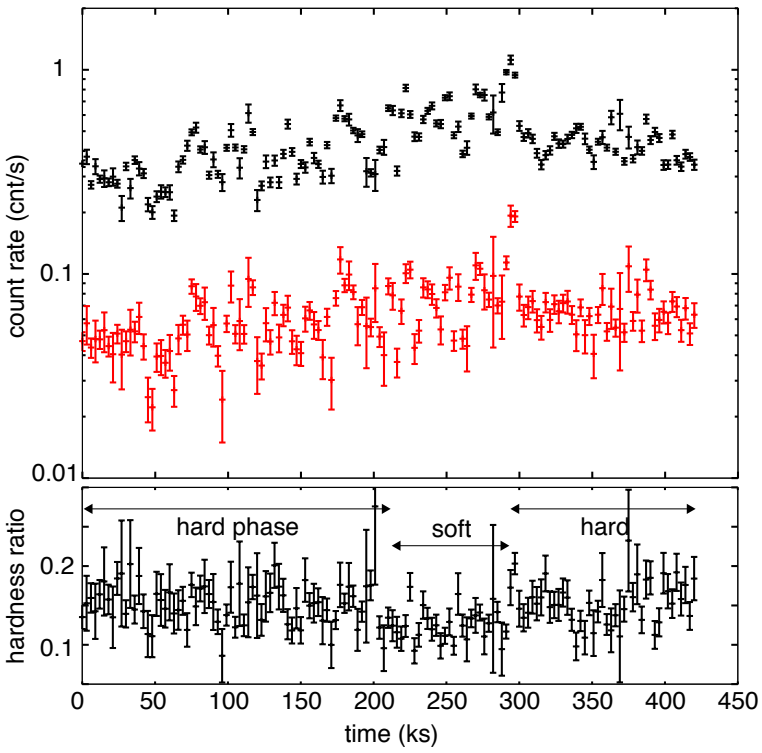

Figure 5.19: (top) Background-subtracted light curves of Ark 564 in 3–10 keV (black) and 10–20 keV (red). (bottom) Hardness ratio between 3–10 keV and 10–20 keV, where the soft and hard phases are indicated.

than those of the other NLS1s, and consists of a dominant PL and a broad Fe line. The spectrum in the hard phase is similar to the time-averaged one. However, the spectrum in the soft phase is more PL-dominant, and do not exhibit such a strong Fe line. Therefore, the reflection is inferred to be less variable than the primary PL.

We first adopted a model consisting of a primary PL as the color-conserved component and a relativistic reflection, `phabs*(powerlaw+kdblur*pexmon)`, which is the same as that used for Mrk 766 (§5.3.3). Again, the model parameters were set as below.

- Fixed parameters; $N_{\rm H}$ of `phabs`; $E_{\rm c}$ of `powerlaw` at 20 keV; the abundance of `pexmon` at 1 solar; the inclination angle of `pexmon` at 60°; and the outer radius of `kdblur` at $400r_{\rm g}$.
- Those left free but common; Γ of `powerlaw`, and $r_{\rm in}$ of `kdblur`.
- Those left free for individual spectra; the normalizations of `powerlaw`, and the solid

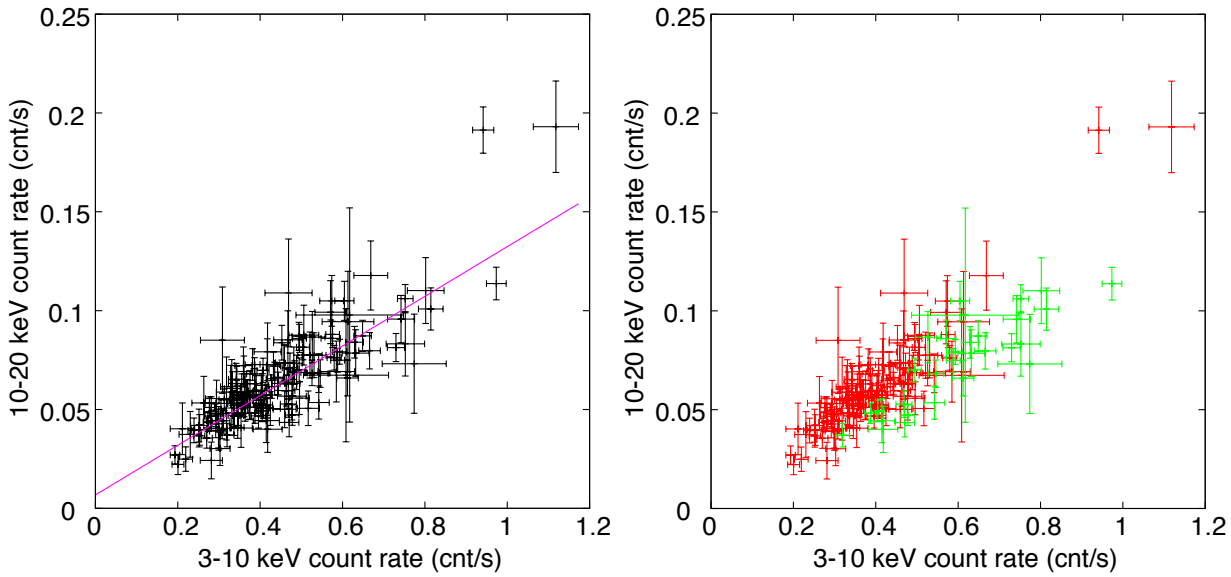

Figure 5.20: (left) A CCP between 3–10 keV and 10–20 keV of Ark 564, fitted with a straight line (magenta), which is unacceptable. (right) The same as the left panel, but derived separately from the hard (red) and soft (green) phases referring to figure 5.19 (bottom).

angle of `pexmon[0]`.

As presented in figure 5.21 (top right), the fit has been acceptable with $\chi^2/\mathrm{d.o.f.} = 118.8/87$. However, The solid angle in the hard phase is unphysically large as $(5.3 \pm 0.8)\pi$, which is required by the data to explain the Fe line intensity. Therefore, we replaced `pexmon` by a reflection model by an ionized matter, `reflionx` (§2.2.2), of which the emissivity around the Fe line is higher than that by a cold matter. This modification is considered appropriate, because X-ray spectra of Ark 564 are known to exhibit a soft excess, which is likely to be contributed by such an ionized reflection (Kara et al. 2017). Figure 5.21 (bottom left) shows the fit with the ionized reflection model, which is even more successful with $\chi^2/\mathrm{d.o.f.} = 96.0/86$. The variable PL is softer with $\Gamma = 2.41 \pm 0.04$ than in the other objects, and the reflection component is not so relativistic with $r_{\rm in} = 98 r_{\rm g}$ (lower limit is $20 r_{\rm g}$). The inner radius implies a hard lag by $r_{\rm in}/c \sim 1$ ks, which is consistent with that confirmed in the soft phase by Kara et al. (2017). The ionization parameter of the reflector is $\log \xi = 2.72 \pm 0.02$, and the solid angles is physically reasonable with $(3.2 \pm 0.8)\pi$ and $(1.4 \pm 0.6)\pi$ in the hard and soft phases, respectively. Ark 564 also has such a large solid angle as Mrk 766.

To examine whether the reflection is variable between the two phases, we next fitted it

with the same model but the absolute fluxes of the reflection in both phases are constrained to be common. The fit result, shown in figure 5.21 (bottom right), has also been acceptable but worse with $\chi^2/\mathrm{d.o.f.} = 106.6/87$. Therefore, the reflection in Ark 564 is favored to vary between the hard and soft phases.

Finally, we again examined the data for possible presence of another primary PL, in the same way as for Mrk 766 (§5.3.3). The upper limit of the hard PL flux in 10–20 keV has been obtained as 1.89×10^{-13} erg cm^{-2} s^{-1}, which is 8.5% of that of the soft PL.

In the two high-η NLS1s, we have found the three features of their reflection. One is the rather broad Fe line with $r_{\rm in} = (30\text{–}100) r_{\rm g}$. Another is such fast variation of the reflection component as the soft PL. The other is the relatively large solid angle of $\gtrsim 2.0\pi$. All of them suggest that the accretion disk extends to rather small radii when the accretion rate is high.

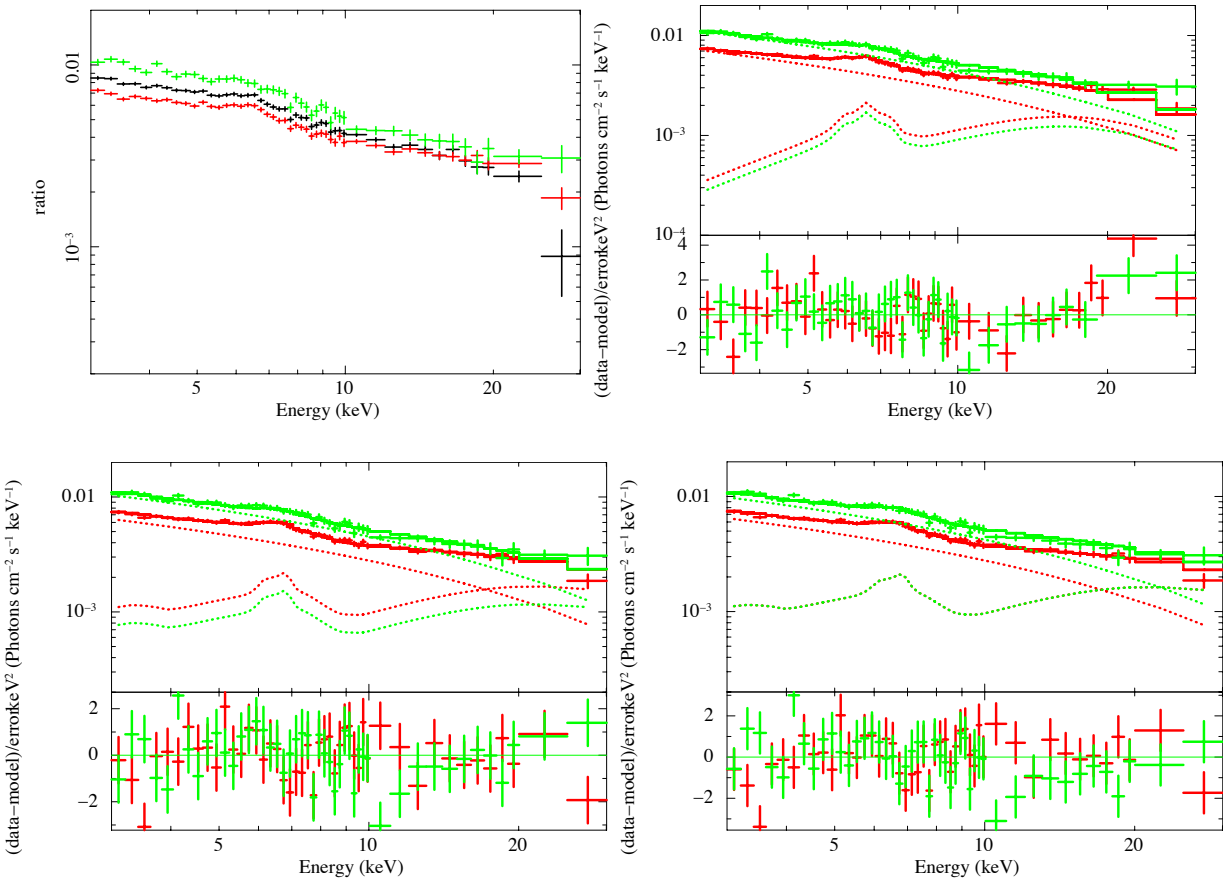

Figure 5.21: (top left) The time-averaged (black) spectrum of Ark 564, and the spectra in the hard (red) and soft (green) phases, in the same form as in figure 5.4. (top right) The spectra of the hard (red) and soft (green) phases, fitted with a model consisting of a PL and relativistic reflection by a neutral matter. (bottom left) The same as the top right but the reflecting material is assumed to be ionized. (bottom right) The same as the bottom left but the absolute fluxes of the reflection are constrained to be common.

5.5 NGC 4051

5.5.1 Description of the object

NGC 4051 is a well investigated NLS1 with $M_{\rm BH} = 1.7 \times 10^6 M_\odot$ (Denney et al. 2009), $z = 0.002336$ (Verheijen & Sancisi 2001), and a relatively low accretion rate of $\eta \sim 0.01$. It is known to exhibit violent X-ray variability and complex variable absorption features by ionized gasses (e.g. Lobban et al. 2011). Therefore, we must be cautious about the variability of the absorption. As described in §4.2, this object was observed five times in 2013 and 2014 for a total net exposure of 172 ks.

5.5.2 Light curves

Figure 5.22 shows background-subtracted light curves of NGC 4051 and hardness ratios, obtained in all observation (2013/06/17a, 2013/06/07b, 2013/10/09a, 2013/10/09b, and 2014/02/16). The 3–10 keV count rate drastically varied by a factor of ~ 2 in ~ 10 ks. The 10–50 keV rate, in contrast, varied considerably less than in 3–10 keV. As a result, the hardness ratio more intensely varied in each observation than in the other NLS1s.

Figure 5.23 shows the soft vs. hard CCP of the observations. Unlike the case of Swift J2127.4+5654 (figure 5.3) or Mrk 766 (figure 5.16), the CCP is considerably curved. This implies that the spectral variability cannot be explained by only flux changes of a single variable component. Therefore, not only the intensity, but also the spectral shape must be changing if the variability is carried by a single component. Alternatively, the source variability is carried by multiple components that vary (e.g. in intensity) under a tightly correlated manner. If we adopt the former picture because of its simplicity, the variable component is considered to become softer as the source gets brighter.

5.5.3 Spectra

Figure 5.24 shows FPMA+FPMB spectra of the five observations. Like in Swift J2127.4+5654, the spectra consist of a PL-like continuum, an Fe K line at 6.4 keV, and a hard X-ray hump at $\gtrsim 20$ keV. A behavior differing from the previous objects is that the spectra considerably hardenes when the source is fainter. This agrees with the implication of the CCP, i.e., the steepening of its slope toward lower flux, and suggests such possibilities as increasing low-energy absorption towards lower luminosity, or changes in the obscured fraction in terms of the partial absorption configuration (§2.2.3).

Although the CCP non-linearity somewhat invalidate the difference spectrum method, it would still be valuable to extract *differential* shapes of the variable component(s). We hence divided all the observations into the high and low phases as defined in §4.2.2. Figure 5.25 shows the spectra in the high and low phases and their spectral differences in the individual observations. The spectral difference on 2013/10/09a is consistent with zero because of its poor statistics. The difference spectra on 2013/06/17b and 2014/02/16 have nearly the same shape, and are reproduced by a $\Gamma = 2.2$ PL. That on 2013/10/09b is explained by a somewhat harder PL with $\Gamma \sim 2.0$, and bending at < 5 keV. Therefore, the difference spectrum again has an approximately PL shape with $\Gamma = 2.2$ in energies above ~ 5 keV, but its flux at < 5 keV becomes suppressed when the source is fainter (on 2013/10/09b). This indicates that this object exhibits changes of absorbers, as reported on other occasions (e.g. Lobban et al. 2011). The *NuSTAR* data, whose energy range is 3–79 keV, is not suitable for examination of the absorption features, because data below ~ 3 keV are needed for this purpose. Therefore, we use *Suzaku* data, which covers 0.5–45 keV, for further analysis of NGC 4051. Details are described in §6.

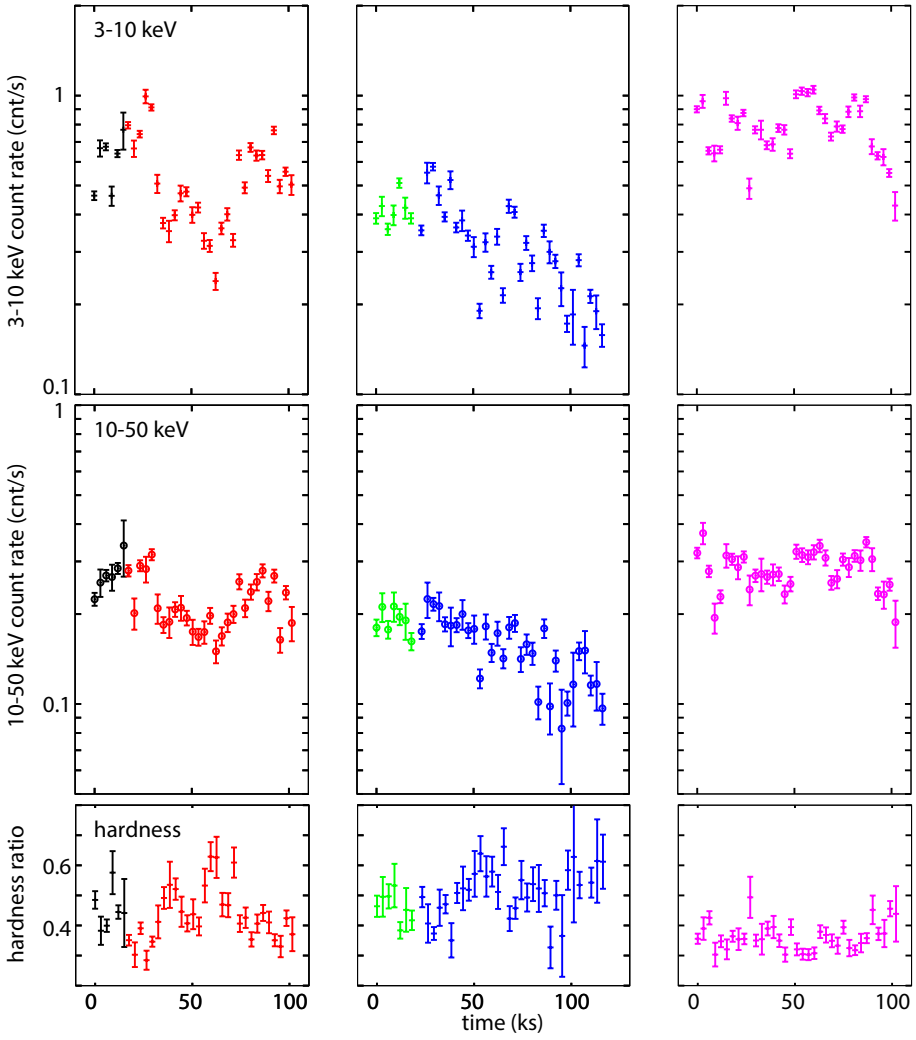

Figure 5.22: (top) Background-subtracted 3–10 keV light curves of NGC 4051 obtained with *NuSTAR*. One data bin is 3 ks. (middle) The same as the top panel but in 10–50 keV. (bottom) Hardness ratios between 3–10 keV and 10–50 keV. The data were obtained on 2013/06/17a (black), 2013/06/17b (red), 2013/10/09a (green), 2013/10/09b (blue), and 2014/02/16 (magenta).

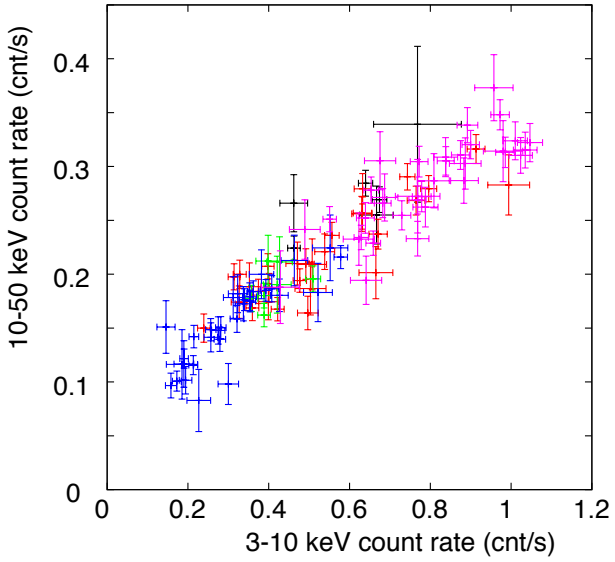

Figure 5.23: A CCP of NGC 4051 between 3–10 keV and 10–50 keV. The colors are same as that in figure 5.22.

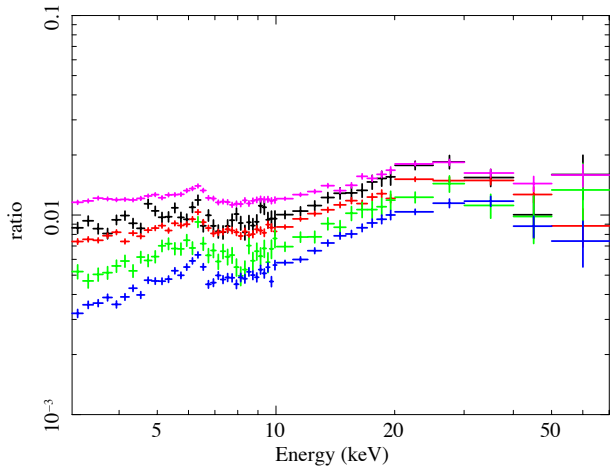

Figure 5.24: The time-averaged spectra of NGC 4051, in the form of their ratios to a $\Gamma = 2$ PL, with the same colors as in figure 5.22.

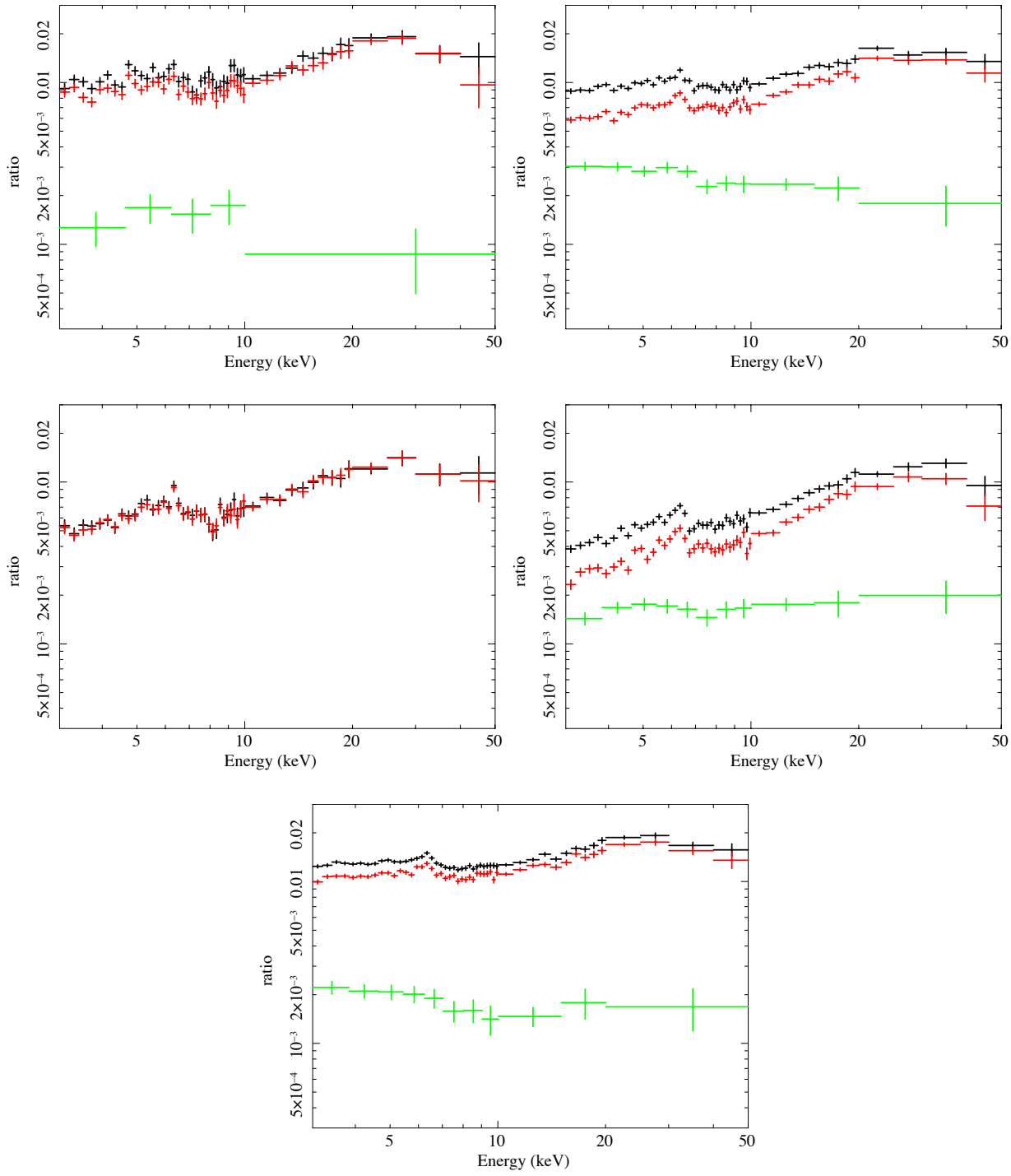

Figure 5.25: The spectra in the high (black) and low (red) phases, and difference spectra between them (green), shown in the same form as figure 5.24.

Chapter 6

NGC 4051: *Suzaku* DATA ANALYSIS

6.1 Light Curves and Spectra

Given the results in §5.5, we continue the study of NGC 4051, using the *Suzaku* data which afford information in much softer energies (down to ~ 0.5 keV) than *NuSTAR*, even though the sensitivity above ~ 10 keV is somewhat poorer than *NuSTAR*. In the three *Suzaku* observations to be described below, NGC 4051 had comparable fluxes to those in the *NuSTAR* observations.

Suzaku observations of NGC 4051 were conducted three times on 2005/11/10, 2008/11/06 (2008a), and 2008/11/23 (2008b) with net exposures of 120 ks, 275 ks, and 78 ks, respectively. Figure 6.1 shows background-subtracted light curves obtained on these occasions with *Suzaku* XIS FI (§3.2.3) and HXD-PIN (§3.2.4). Because of their high statistics and variability, the XIS data are shown with 500 s bins. The HXD-PIN data with lower statistics are shown with 10 ks bins. The 3–10 keV count rate changed by a factor of ~ 2 within ~ 10 ks like in the *NuSTAR* observations (§5.5), and the average count rate in 2005 was about one fifth of those in 2008. The hard X-ray count rates were less variable. The hardness between 3–10 keV and 15–45 keV were rather constant in each observation, but was systematically higher in 2005 when the object was dimmer.

Figure 6.2 shows time-averaged spectra of the individual observations. In energies above ~ 2 keV, they consist of a PL-like continuum, a strong Fe K line, and a hard X-ray excess. These spectral shapes at > 2 keV, together with a prominent slope change in 2–5 keV, are quite similar to those obtained with *NuSTAR* (figure 5.24), and the spectrum in 2005 is as hard as that with *NuSTAR* on 2013/10/09. In addition, an outstanding feature that was outside the *NuSTAR* energy range is the sharp spectral upturn below ~ 1.5 keV; this

contributes to soft excess (§2.1.3). In the spectrum in 2005, particularly, Fe L absorption features are seen at $\sim$ 0.8 keV, which suggests the presence of an ionized absorber with $\log \xi \sim 2$ as shown in figure 2.19b.

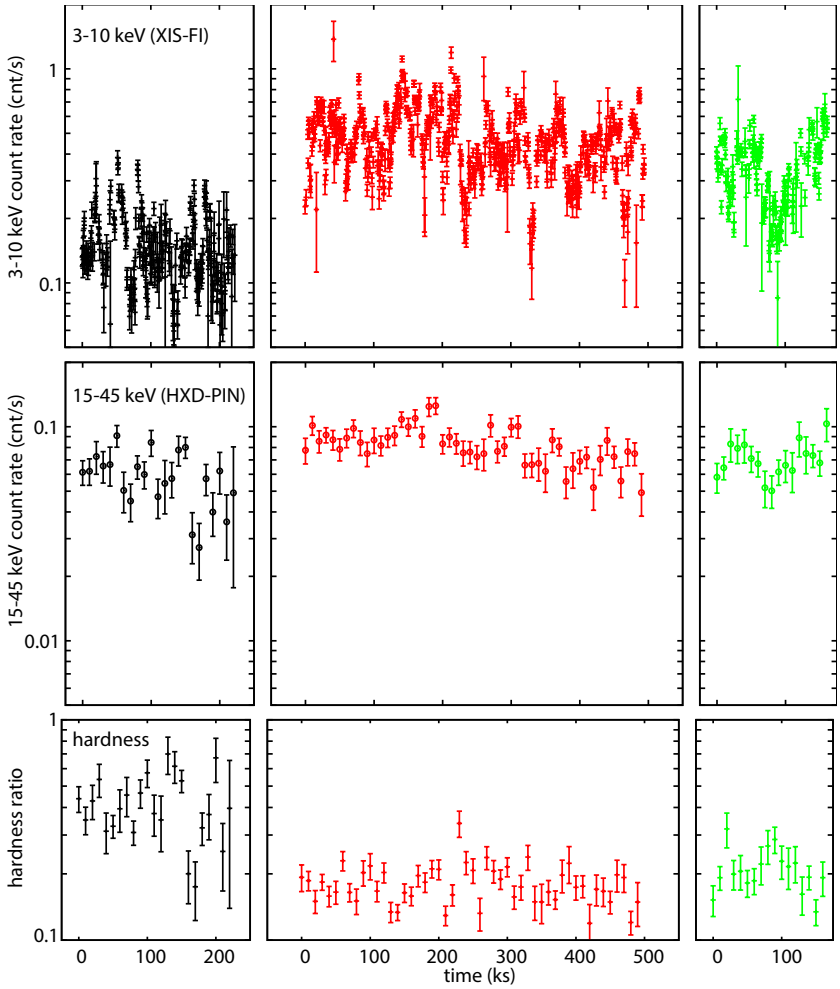

Figure 6.1: (top) Background-subtracted 3–10 keV light curves of NGC 4051, obtained with XIS-FI onboard *Suzaku* in 2005, 2008a (red), and 2008b (green). One data bin is 500 s. (middle) The same as the top panel but in the 15–45 keV with HXD-PIN. One data bin is 10 ks. (bottom) Hardness ratios between 3–10 keV and 15–45 keV, with 10 ks binning.

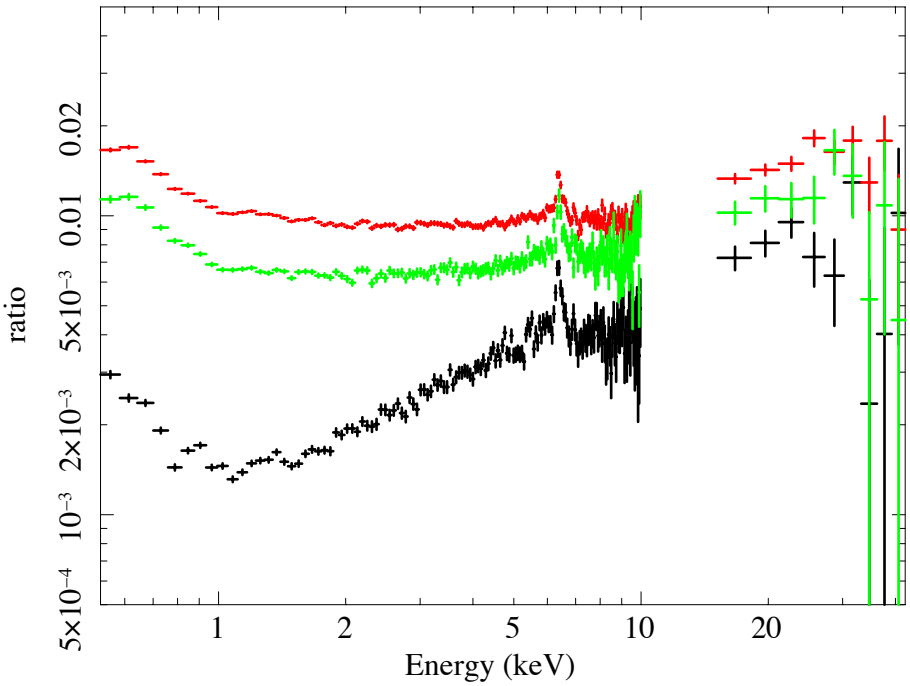

Figure 6.2: The time-averaged spectra of NGC 4051 obtained with *Suzaku* in 2005 (black), 2008a (red), and 2008b (green). The data below 10 keV were obtained with the XIS, and those above 15 keV with the HXD.

6.2 Difference spectrum analysis of the *Suzaku* data

The CCP of NGC 4051 obtained with *NuSTAR* (figure 5.23) was somewhat curved. Previous studies using the same *Suzaku* data of NGC 4051, as we utilize here, revealed that such non-linear effects are not seen between any pair of energy bands (Noda 2013; Terashima et al. 2009). To confirm these reports, and to compare the three *Suzaku* data sets, we have produced two kinds of CCPs from the XIS data; one between 0.5–1 keV and 1–2 keV (i.e., the softest end), and the other between 3–5 keV and 5–10 keV. The derived CCPs, with the data sets specified by colors, are shown in figure 6.3 superposed. The higher-band three CCPs (right panel) are all quite linear, without offset or slope differences among the data sets. The lower-band CCPs (left panel) are also approximately linear, but the slope in 2005 (black points), 2.03 ± 0.08 as indicated by a gray line, is flatter than that in 2008 (green and red data points), 2.26 ± 0.04 as represented by an orange line. Therefore, through the three observations, the variable component of this NLS1 retained its shape in > 3 keV, but

changed the shape in < 1 keV. These suggest that X-ray absorption, possibly by ionized absorbers, is playing an important role.

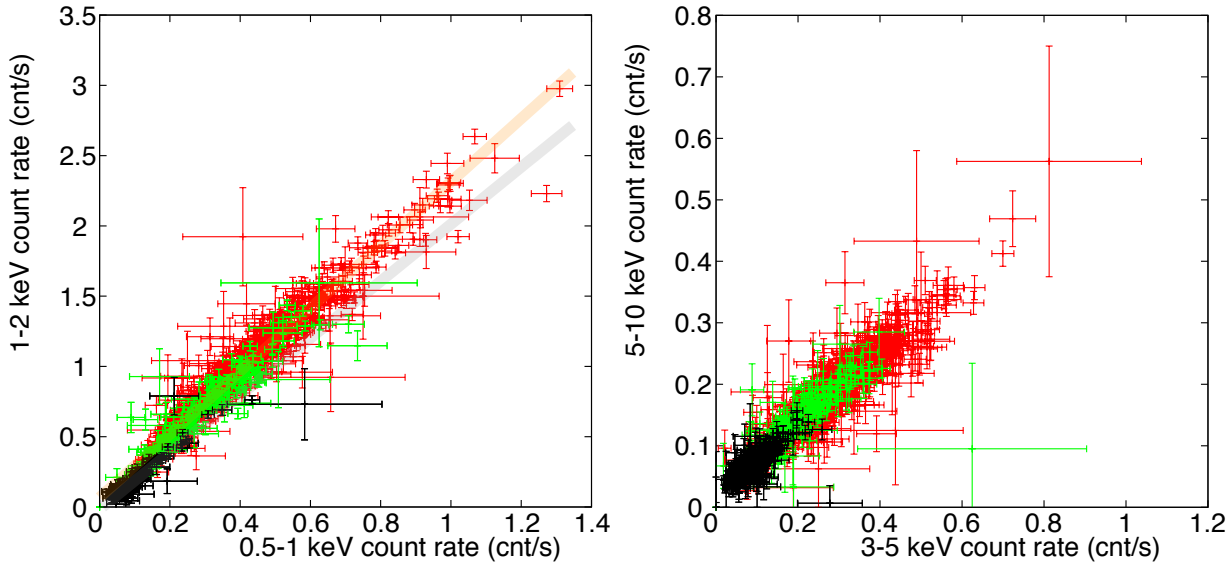

Figure 6.3: (left) CCPs between the 0.5–1 keV and 1–2 keV bands of *Suzaku* data in 2005 (black), 2008a (red), and 2008b (green). Those in 2005 and in 2008 are fitted with straight lines colored with gray and orange, respectively. (right) The same as the left panel but between 3–5 keV and 5–10 keV.

Figure 6.4 shows difference spectra between the high and low phases in the individual *Suzaku* observations, derived in the same way as for Swift J2127.4+5654 (§5.1.4). Each difference spectrum has a shape similar to that observed with *NuSTAR* at a comparable luminosity. That in 2005 exhibits strong bending below 5 keV, together with the deep Fe L features, like in the time-averaged spectrum. Those in 2008 are close to a PL except the soft excess seen below ~ 1 keV. To avoid the complexity of the spectrum below ~ 1 keV, we tentatively fitted the time-averaged spectra in 2008a and 2008b in 1–45 keV by a PL with the same Γ. However, as shown in figure 6.4 (right), the fit was unacceptable with $\chi^2/\mathrm{d.o.f.} = 188.0/111$ because of an excess in 5–10 keV, which is considered to arise from an ionized absorber with $\log \xi \sim 3$ as shown in figure 2.19b. In this way, the study of NGC 4051 requires us to fully consider the effects of ionized absorption, even in the 2008 spectra which appear relatively simpler.

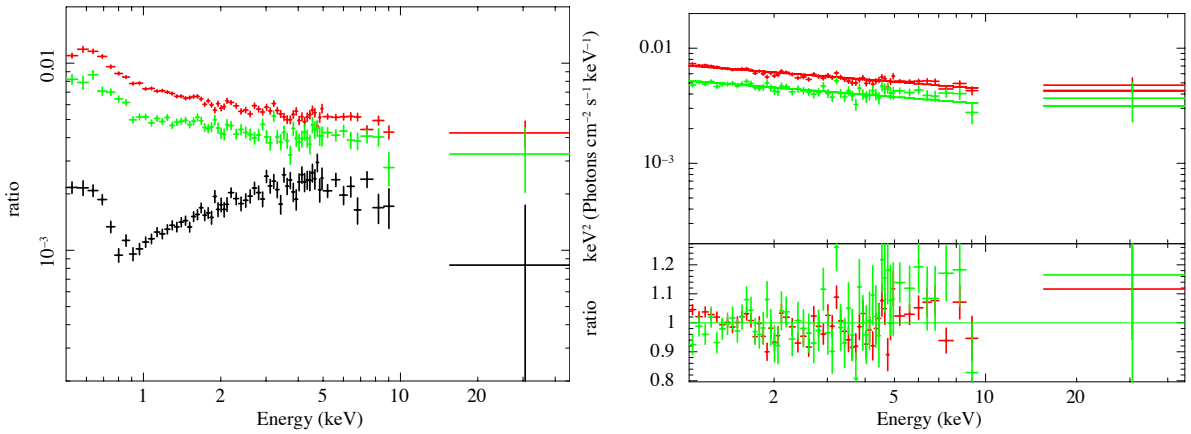

Figure 6.4: (left) Difference spectra between the high and low phases in the *Suzaku* observations in 2005 (black), 2008a (red), and 2008b (green). They are shown in the same style as for the *NuSTAR* spectra. (right) The difference spectra in 2008a and 2008b in νF_ν form, fitted in 1–45 keV with a PL with a common Γ.

6.3 Spectral fitting to the 2005 data

Because the spectrum in the 2005 observation (figure 6.4 black) is likely to be absorbed strongly by an ionized gas with $\log \xi \sim 2$, we fitted an absorbed PL to the difference spectrum in 2005. In the following analyses, the interstellar absorption with $N_{\rm H} = 1.2 \times 10^{20}$ cm^{-2} (Kalberla et al. 2005) is taken into account. Figure 6.5 shows the fit, which has been acceptable with χ^2/d. o. f. $= 61.5/59$. The fit result implies that a PL with $\Gamma = 2.17 \pm 0.06$ is absorbed by an ionized gas with $N_{\rm H} = (3.5 \pm 0.6) \times 10^{22}$ cm^{-2}, $\log \xi = 1.98^{+0.09}_{-0.32}$, and the covering factor of $f_{\rm c} = 0.90 \pm 0.07$. The main variable PL is thus relatively soft, like in the other NLS1s studied. The reason why the difference spectrum in 2005 (black in figure 6.4 left) appears very hard is solely because it is strongly absorbed by the ionized gas.

To simultaneously fit the spectra in the high and low phases in 2005, we first used a model consisting of the soft PL with $\Gamma = 2.17$ (fixed) as determined with the difference spectrum, another harder PL with $\Gamma \sim 1.5$ as we found from Swift J2127.4+5654, and a distant reflection component, expressed as `phabs*(zxipcf[0]*powerlaw[0]+zxipcf[0′]*powerlaw[1]+pexmon)`, where the two PLs are subjected to ionized absorption, `zxipcf`. The components tagged with `[0]` and `[0′]` are required to have the same $N_{\rm H}$ and $\log \xi$, but allowed to have different $f_{\rm c}$. The abundance of the reflector was fixed at 1 solar. Between the high- and low-phase spectra, only normalization of `powerlaw[0]` was allowed to take individual values. Figure 6.6 shows the fit in the 1–45 keV band with the model. Because of some response uncertain-

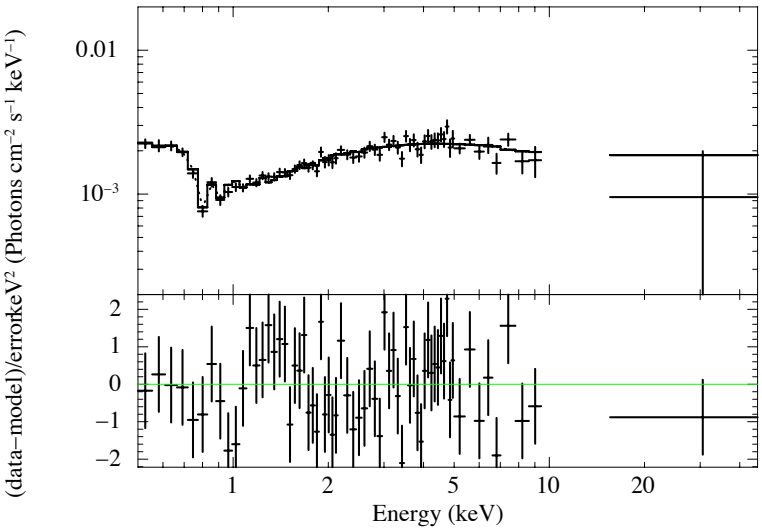

Figure 6.5: The difference spectrum in 2005 fitted with a PL absorbed by an ionized gas.

Table 6.1: Emission (four from the top) and absorption (the other two) lines taken into account.

energy	line ID
0.6 keV	O VII
0.90 keV	Ne IX
1.35 keV	Mg XI
6.6 keV	Fe XXV
6.8 keV	Fe XXIV (outflow with 4600 km s^{-1})
7.2 keV	Fe XXV (outflow with 10000 km s^{-1})

ties, the 1.8–1.9 keV range was excluded. The fit was however completely unacceptable with χ^2/d. o. f. $= 403.1/134$, and the residuals require fine tunes of absorption modeling, emission and absorption lines, and the soft excess component. The residuals in 5–10 keV requires another ionized absorption, `zxipcf[1]`, with $\log \xi \sim 3$ (see figure 2.19b). In addition, we took into account emission and absorption lines listed in table 6.1, after Terashima et al. (2009) and Lobban et al. (2011). Finally, we adopted a thermal Comptonization model, `comptt` (Titarchuk 1994), to account for the soft excess as adopted in Noda et al. (2011b, 2013a). The seed photon temperature of `comptt` was fixed at 32 eV, which is the disk temperature at $6r_g$ of NGC 4051 with $\eta = 0.1$ (figure 2.14). The line features and `comptt` were added as stationary components.

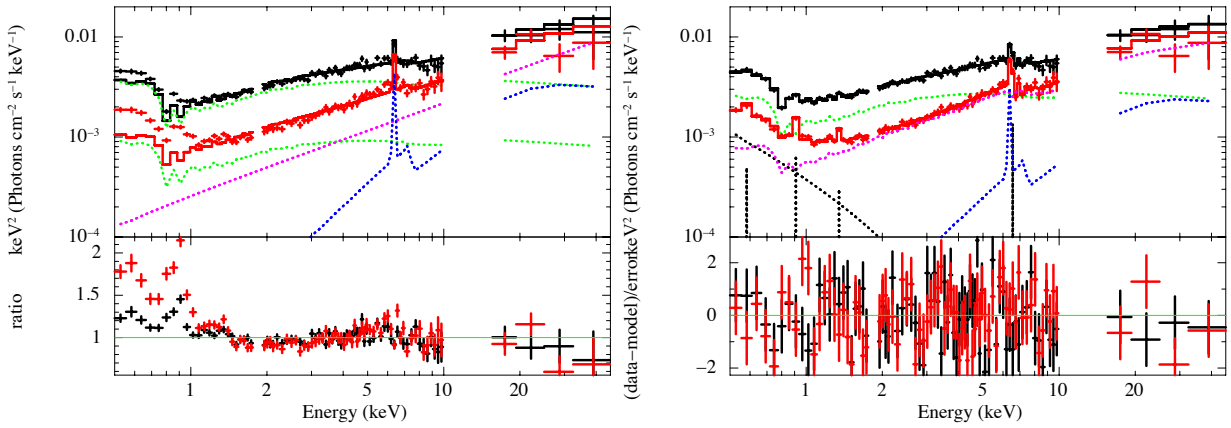

Figure 6.6: (left) The spectra in the high (black) and low (red) phases in 2005 fitted simultaneously with a model consisting of a soft PL (green), a hard PL (magenta), and a reflection component (blue). (right) The same as the left panel but using an improved model which incorporates `comptt` and absorption/emission lines listed in table 6.1. The two PLs are absorbed by one (left panel) or two (right panel) ionized gas(ses).

With the model improved in this way, the fit has become acceptable with $\chi^2/\mathrm{d.o.f.} = 166.7/135$, as shown in the right panel of figure 6.6. Unlike in Swift J2127.4+5654, the soft PL with $\Gamma = 2.17$ disappears in the low phase, while it contributes to about two thirds of the X-rays in the high phase. Its flux changed by a factor of > 6. These presence and absence of the soft PL provide the major cause of the large change in the ~ 2 to ~ 7 keV slope, from 2005 to 2008 (figure 6.2). The other PL has $\Gamma = 1.61^{+0.06}_{-0.21}$, which is distinct from that of the soft PL. Therefore, this harder PL cannot be a partially absorbed part of the soft PL, but must be another primary component. When the hard PL is replaced by a relativistic reflection, the solid angle of the reflector becomes unphysically large as $> 7\pi$ because this component has much contribution to the spectra. In this way, the spectrum of NGC 4051 in 2005 is also considered to harbor the two distinct primary PLs, like Swift J2127.4+5654.

These PLs are absorbed by the two discrete ionized gasses, which are the same between the high and low phases. Figure 6.7 shows a block diagram representing the best-fit model, and table 6.2 shows the best-fit parameters of `zxipcf[0]` and `[1]`. The former is low ionized and relatively thin, whereas the latter is highly-ionized thick gas. Both PLs are absorbed by `zxipcf[0]` with a consistent f_c, while `zxipcf[1]` covered only the hard PL.

The Comptonization representing the soft excess has been found to have an electron temperature of 0.70 keV and $\tau = 6.1$. These are slightly similar to the parameters (0.49 keV

Table 6.2: The best-fit parameters of the ionized absorber in 2005 and 2008.

`zxipcf`	2005 `[0]`	2005 `[1]`	2008a `[0]`	2008a `[1]`	2008b `[0]`	2008b `[1]`
$N_{\rm H}$ (10^{22} cm^{-2})	(3.9 ± 0.6)	(60 ± 30)	3.3 ± 0.2	290 ± 70		
$\log \xi$	$1.96^{+0.09}_{-0.32}$	3.0 ± 0.3	1.96 ± 0.26	2.88 ± 0.05		
$f_{\rm c}$ (soft PL)	0.85 ± 0.07	0	$0.12^{+0.12}_{-0.04}$	0.4 ± 0.1	0.24 ± 0.04	$0.57^{+0.04}_{-0.09}$
$f_{\rm c}$ (hard PL)	0.6 ± 0.3	0.6 ± 0.3	$0.4^{+0.5}_{-0.2}$	0.6 ± 0.1	1 (> 0.6)	$0.66^{+0.09}_{-0.13}$

and $\tau = 17$) which Noda et al. (2011b) found for the soft excess of Mrk 509. The solid angle of the reflector is physically reasonable at $\sim 2.0\pi$, when both PLs are assumed to participate in the reflection. In this way, the fit results are physically appropriate.

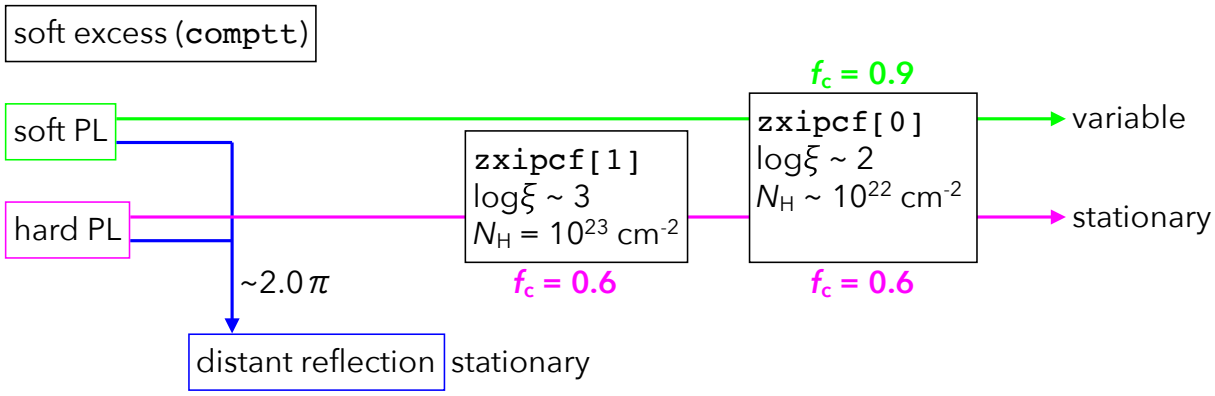

Figure 6.7: A block diagram representing the best-fit model for the *Suzaku* spectrum in 2005.

6.4 Spectral fitting to the 2008 data

Because the difference spectra in 2008 do not exhibit the low-energy drop at $\lesssim 3$ keV unlike in 2005 (figure 6.4), they are considered to be much less subject to the $\log \xi \sim 2$ ionized absorption. Instead, the difference spectra in 2008 exhibit absorption features with $\log \xi \sim 3$ as explained in §6.2. We first conducted fitting to the difference spectra in 2008a with the same model, `zxipcf*powerlaw`, as used for the 2005 data. However, the fit was unsuccessful with $\chi^2/{\rm d.o.f.} = 124.3/73$, because `zxipcf` cannot simultaneously explain the soft excess and the $\log \xi \sim 3$ features. Therefore, we fitted the data in the 1–45 keV range with the same model to examine residuals of the soft excess. Figure 6.8 (top) shows the fit which is acceptable with $\chi^2/{\rm d.o.f.} = 83.3/65$. The residual below 1 keV suggests that

`comptt` also varies in 2008a. Hence, we again fitted the 0.5–45 keV difference spectra with a model, `zxipcf*powerlaw+comptt`. The fit is shown in figure 6.8 (bottom left), and has been successful with χ^2/d. o. f. $= 87.9/70$. The PL has $\Gamma = 2.26 \pm 0.05$, consistent with that in 2005, but the ionized absorber with $\log \xi = 2.8$ and $N_{\rm H} = 1 \times 10^{24}$ cm^{-2} is rather close to `zxipcf[1]` in §6.3 than `zxipcf[0]`, as expected.

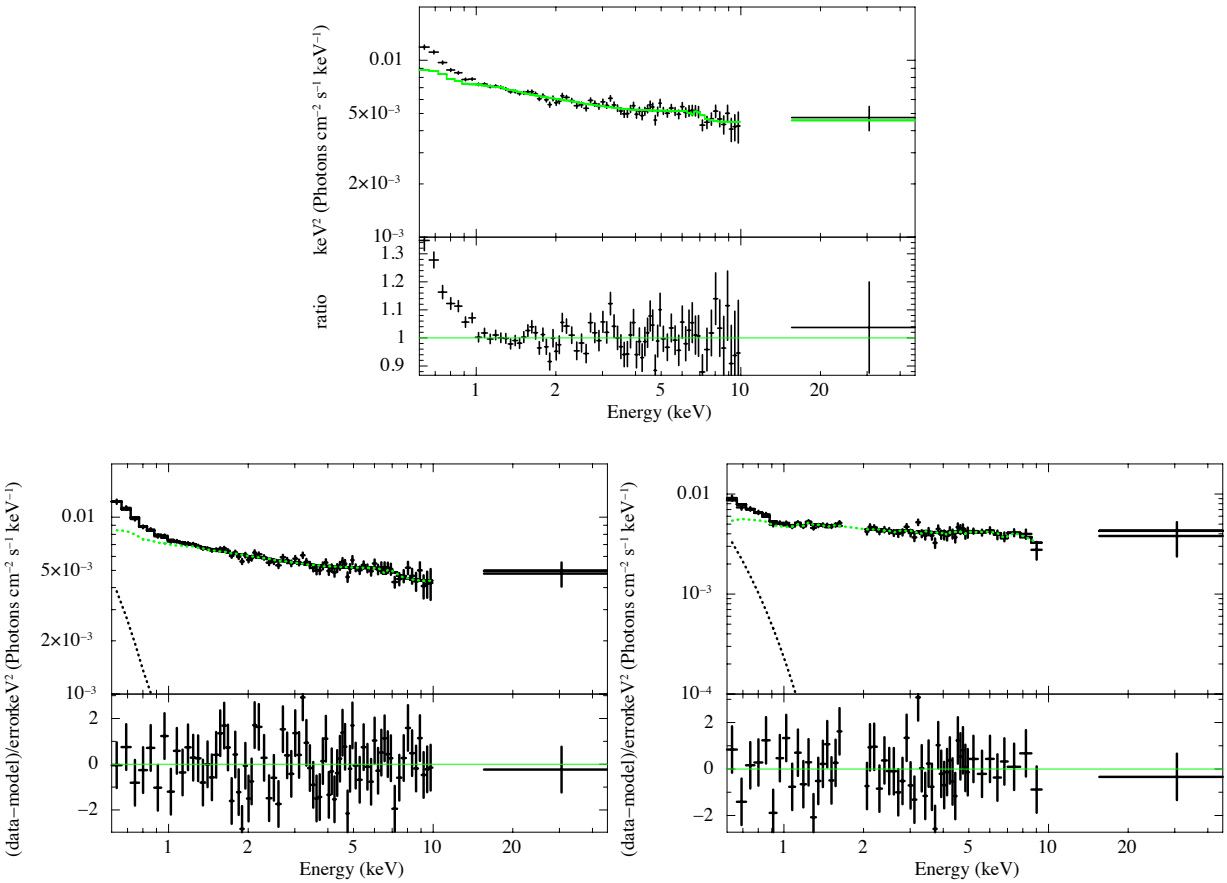

Figure 6.8: (top) The difference spectra in 2008a fitted with `zxipcf*powerlaw` (green). (bottom left) The same as the top panel but using an improved model incorporating `comptt` (black). (bottom right) The same as the bottom left panel but in 2008b.

Finally, we conducted the simultaneous fitting to the high- and low-phases spectra in 2008a with the same model as in 2005, but `comptt` was constrained to vary synchronized with the soft PL. As shown in figure 6.9 (left), the spectra have been successfully reproduced with χ^2/d. o. f. $= 179.9/149$. The hard PL has $\Gamma = 1.54 \pm 0.12$, which is consistent with that in 2005. As shown in table 6.2, ξ of each ionized absorber is also consistent between

2005 and 2008a. The parameters of `comptt` have not been well constrained.

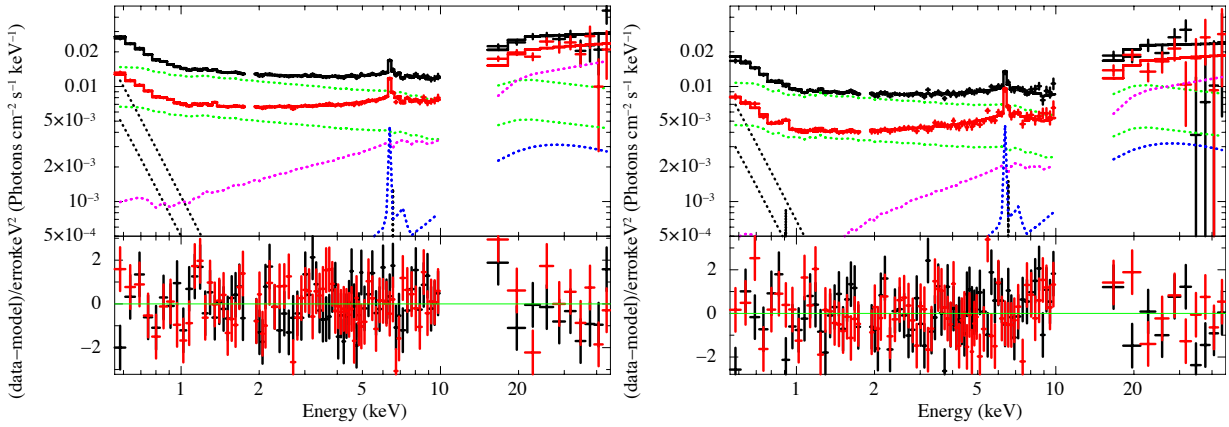

Figure 6.9: The same as the right panel of figure 6.6 but of the 2008a (left) and 2008b (right) data.

The 2008b data have also been analyzed with the same manner as in 2008a. The difference spectrum (figure 6.8 bottom right) and the high- and low-phase spectra (figure 6.9 right) have been successfully reproduced by the same models with the same parameters, except f_c of the ionized gasses and the normalizations of all the components.

6.5 Summary on NGC 4051

The spectra of the three observations of NGC 4051 are successfully explained by the model including the two primary PLs as Swift J2127.4+5654. The soft PL with $\Gamma = 2.2$ carries most of the flux variations in time scales of ~ 10 ks, while the hard PL with $\Gamma = 1.5$ is stationary in such a short time scale. From 2005 to 2008, the former increased its normalization by a factor of ~ 10, while the latter is less variable, and changed by a factor of ~ 2.

The primary PLs are subjected to two ionized absorption. One is thin ($N_{\rm H} \sim 10^{22}$ cm^{-2}) and low ionized ($\log \xi = 2.0$), and the other is thick ($N_{\rm H} \sim 10^{23}$ cm^{-2}) and highly ionized ($\log \xi = 3.0$). When the source is faint in 2005, the former dominantly absorbs the soft PL, and the thin absorber less covers the soft PL in 2008. This can be interpreted that the soft PL brightening highly photo-ionized the thin absorber, and it cannot be distinguished from the $\log \xi = 3.0$ absorber. As the source flux increases by a factor of ~ 3, $N_{\rm H}$ of the highly-ionized absorber becomes thicker by a factor of 4.8 ± 2.7. Therefore, this absorber is considered to be driven by the total emission of NGC 4051.

Chapter 7

DISCUSSION

7.1 Spectral Components in NLS1s

Utilizing time variations and the differential spectroscopy, we have confirmed in §5 and §6 that X-ray spectra of some NLS1s consists of two distinct primary components in the same way as Seyfert 1s (e.g. Noda 2013).

7.1.1 The soft PL

In §5 and §6, we found that the four NLS1s, Swift J2127.4+5654, Mrk 766, Ark 564, and NGC 4051 are all highly variable, and that their X-ray variability is predominantly carried by a soft primary PL, which appears as color-conserved variations in their CCP. The soft PL exhibits high and fast flux variations, reaching a factor of ~ 2 within ~ 10 ks. Their spectral slope is $\Gamma = 2.1$–2.4, which is consistent with those of Seyfert 1s (Noda 2013). The result implies that the corona emitting the soft PL of NLS1s is essentially in the same physical state as those of Seyfert 1s. Therefore, the well known fact that NLS1s exhibit significantly softer spectra than Seyfert 1s can be explained by the dominance of the soft PL in their spectra.

By using the *NuSTAR* data, which cover a wide range of 3–79 keV, a cutoff was seen at 50 keV and 20 keV in the spectra of Swift J2127.4+5654 and Ark 564, respectively. These cutoffs provide evidence that the soft PL is generated via thermal Comptonization in a hot "corona". We calculated the coronal optical depth (§2.2.1) of these objects as $\tau = 1.5$ in Swift J2127.4+5654, and $\tau = 2.0$ in Ark 564. These values are relatively thicker than a typical value of Seyfert 1s, $\tau = 1.0$, which is indicated by $\Gamma = 2.0$ and $E_{\rm c} = 100$ keV. In short, the soft-PL-emitting corona in an NLS1 is likely to be cooler and thicker than those

of Seyfert 1s.

7.1.2 The hard PL

In the X-ray spectra of Swift J2127.4+5654 and NGC 4051, we discovered the harder primary PL, which is stationary or less variable compared to the soft PL. Because the hard PL in Swift J2127.4+5654 is also required to have a cutoff at $E_{\rm c} \sim 50$ keV, the harder primary is also considered to arise from thermal Comptonization. This component has $\Gamma = 1.3$ ($\tau = 3.2$) in Swift J2127.4+5654, and $\tau = 1.6$ in NGC 4051, which are similar to those of Seyfert 1s (Noda 2013). On the other hand, their absorption features are different from Seyfert 1s; the hard PL of Swift J2127.4+5654 exhibits stronger neutral absorption with $N_{\rm H} = 8.3 \times 10^{23}$ cm^{-2} than those of Seyfert 1s ($N_{\rm H} \sim 2 \times 10^{23}$ cm^{-2}), and that of NGC 4051is absorbed by two ionized absorbers with $\log \xi \sim 2.0$ and $\log \xi \sim 3.0$.

7.1.3 Fluxes of the soft and hard PLs

The *NuSTAR* data of the two NLS1s with high accretion rates, Mrk 766 and Ark 564, did not show evidence of the hard PL, and yielded its upper limits (§5.3, §5.4). This strengthen the discovery by Noda (2013), that the hard PL is dominant among low-η objects. For a further examination, figure 7.1 shows flux ratios of the hard PL to the soft PL in 6–10 keV, against the Eddington ratio η (§2.6). To compare our results with those by Noda (2013), η was calculated using the same bolometric correction factor of 10 in 3–10 keV. Because the absorption of the hard PL of Swift J2127.4+5654 is not negligible even in the 6–10 keV band, the hard PL flux was calculated after removing the absorption. On this figure, NLS1 and Seyfert 1 behave in the same manner, and they consistently indicate that the hard PL and the soft PL dominate the spectrum at $\eta < 0.01$ and $\eta > 0.01$, respectively. In a sense, this suggests a kind of state transition of AGNs, as first suggested by Noda (2013). In particular, Mrk 766 and Ark 564 provide valuable data points (even though upper limits) at the highest-η region.

Figure 7.2 shows absolute 6–10 keV fluxes. There, the soft-PL flux is seen to increase more steeply, towards larger η, than that of the hard PL. However, the scatter is large, and a systematic difference is seen in between NLS1s and Seyfert 1s, probably because of their difference in $M_{\rm BH}$. Therefore, in figure 7.3, we have scaled the two PL fluxes to the Eddington luminosity $L_{\rm Edd}$ (§2.1.6), so that the ordinate now means the fraction of η contributed by each PL. Now, NLS1s and Seyfert 1s behave essentially in the same way. Furthermore, we can identify the following three luminosity regimes.

1. $\eta < 0.01$: The hard-PL flux dominates, and increases approximated as $\propto \eta$. The soft-PL flux has a minor contribution, but it increases steeply with η.

2. $0.01 < \eta < 0.1$: The two PLs co-exist, with their fluxes both increasing as $\propto \eta$.

3. $0.1 < \eta$: The hard-PL flux becomes saturated at a value of 0.03–$0.1 L_{\rm Edd}$. The soft PL becomes dominant, and its flux increases as $\propto \eta$.

In short, this result provides the first evidence that AGNs also exhibit a phenomenon that is analogous to the state transition seen among black hole binaries (e.g. Tananbaum et al. 1972).

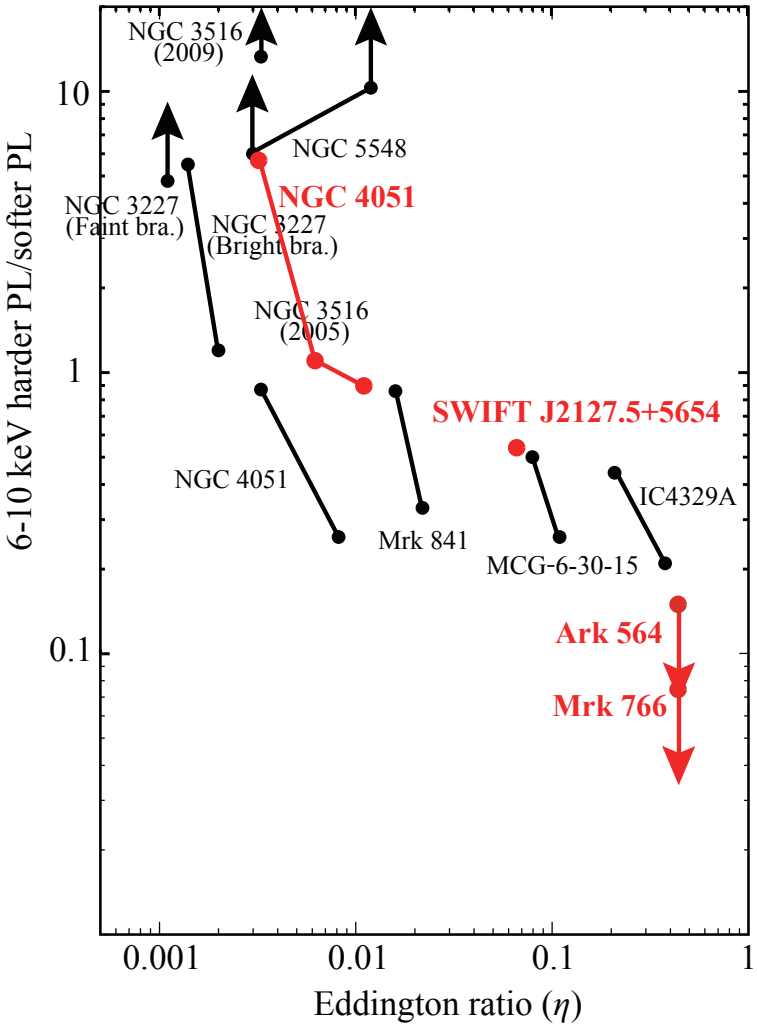

Figure 7.1: Flux ratios of the hard PL to the soft PL calculated in 6–10 keV. The results by the present thesis (red) are overlaid on those by Noda (2013) (black).

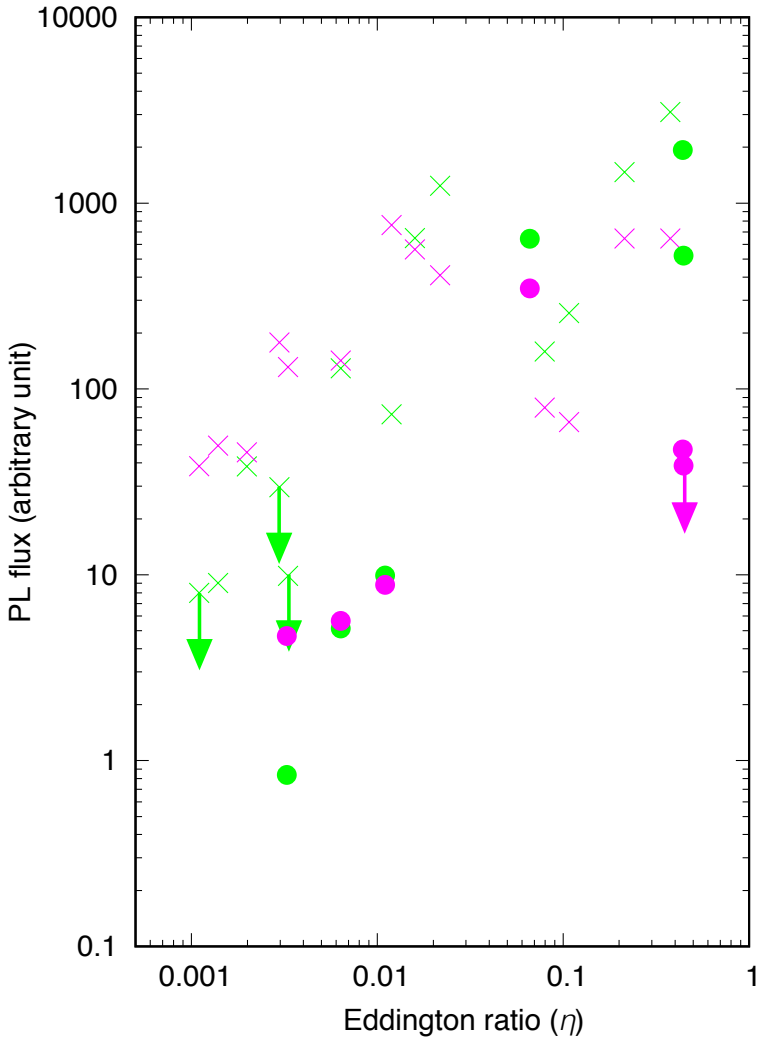

Figure 7.2: Absolute 6–10 keV fluxes of the soft (green) and hard (magenta) PLs of the Seyfert 1s (×) and NLS1s (•), made from figure 7.1.

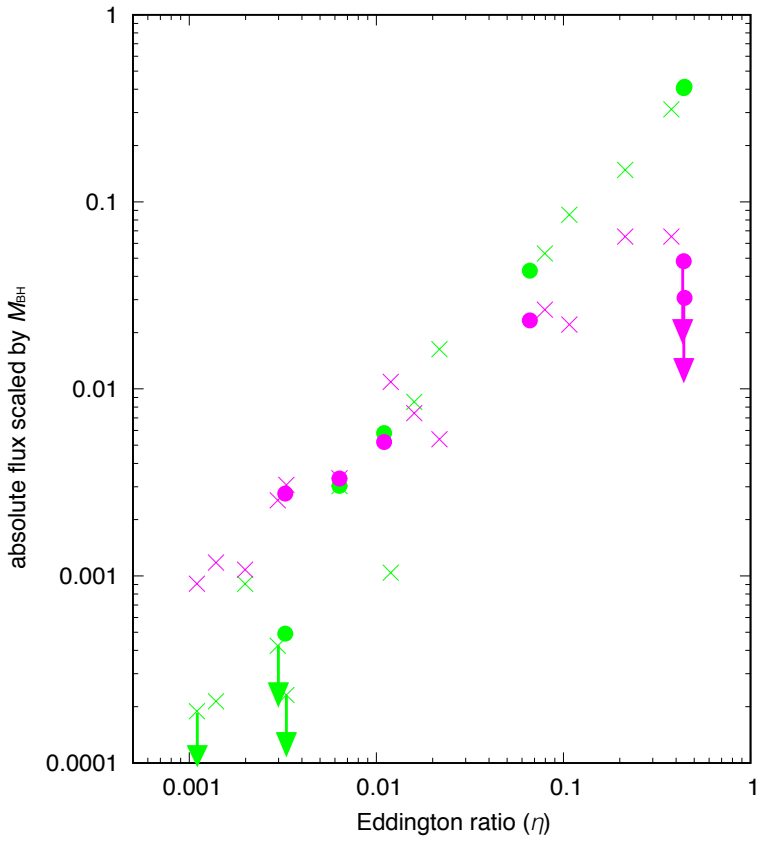

Figure 7.3: The same as figure 7.2, but the soft-PL and hard-PL fluxes are scaled by $M_{\rm BH}$. The sum of the soft (green) and hard (magenta) PLs equals η.

7.1.4 Reflection components

Like in many Seyfert 1s, the NLS1s in our sample with low accretion rates of $\eta \lesssim 0.1$ exhibit the stationary narrow Fe K line, which is considered to arise via reflection by distant neutral materials, such as the dusty torus. On the other hand, the reflection of the two high-η sources, Mrk 766 and Ark 564, is characterized by relatively fast variability, a rather large solid angle, and relatively broad Fe K line. As explained in §5.4.3, the reflection components of the latter objects are considered to have significant contribution from materials located near the SMBHs, including in particular the accretion disk extending inside. However, their $r_{\rm in} = 30$–$100 r_{\rm g}$ is not so small as reported by some AGN studies (e.g. Nandra et al. 2007) that assumes only a single PL to model the continuum to be subtracted.

When $r_{\rm in}$ is thus decreases towards higher η, the hard PL is expected to become fainter because of the inevitable reduction of RIAF region which is thought to locate at $\lesssim r_{\rm in}$, i.e., inside the disk. Therefore, the reflection properties of the high-η NLS1s agree with the absence of the hard PL. Because the reflection produced by the soft PL in such AGNs has a large solid angle ($\sim 2\pi$), the corona emitting the soft PL (soft corona) is considered to be located near the accretion disk. On the other hand, the corona emitting the hard PL (hard corona) is likely to be detached from the disk, and hence the disk subtends the hard corona with a much smaller solid angle. For the reason, the distant reflection generated by the hard PL is dominant in NLS1s with $\eta \lesssim 0.1$.

In contrast to the overall trend, that the reflection is dominant at a high accretion rate, the solid angle of the reflector of Ark 564 (§5.4.3) decreases when the soft PL brightens. To explain this behavior remains our future task.

7.1.5 The other models

Instead of the hard PL, the relativistic reflection (§2.2.2) and the partial covering absorption (§2.2.3) have often been adopted (§1) to explain X-ray spectra of AGNs. We briefly discuss these models. According to "light bending" view (§2.2.2), the relativistic reflection can vary independently of the illuminating primary. Therefore, we cannot rule out this picture based on time variations. However, if we tried to explain the X-ray spectra of Swift J2127.4+5654 with this modeling, the fit requires the Fe abundance of 0.5 solar (§5.1.6, Marinucci et al. 2014), which seems to be unrealistically low. In addition, the data of NGC 4051 require unphysically large solid angle of the reflector as $> 7\pi$ (§6.3). These anomalies arise because the hard X-ray hump of these NLS1s (as well as of many Seyfert 1s) are so strong that the relativistic reflection is required to be too strong (NGC 4051), or to over-predict the

associated Fe-K line.

In the scenario invoking partial covering absorption, changes of the covering factor f_c is regarded as the cause of the variations of hardness ratio. The small variations of hard X-rays independent of those of soft ones are explained by assuming a negative correlation between the intensity of the primary component and f_c. However, the partial covering absorption cannot easily explain the 6 ks hard lag (§5.2). In fact, this view requires that an intensity increase of the soft PL primary should be followed, in 6 ks, by a correlated increase in f_c. This is difficult to explain, because an increase of the primary should enhance (after some delay) the ionization of the partial absorber, and would make f_c lower. Furthermore, the presence of the 6 ks lag when the spectrum is soft (§5.2) cannot be easily explained by this view. In summary, the present data are not in favor of the partial absorption scenario, either.

7.2 Time Variability of the Soft and Hard PLs

7.2.1 Time scales

We detected variations from both PLs in Swift J2127.4+5654. To quantitatively evaluate their time scales, one convenient method may be so-called variability function (e.g. Maejima et al. 1984), defined as

$$f(t_b) = \frac{\sqrt{V-\sigma}}{x(t_b))}, \tag{7.1}$$

where t_b is the time-bin width, V is the total data variance, $x(t_b)$ is the average background-subtracted count rate, and σ is Poisson-error. It tells us how many percent of the mean count rate is varying (after Poisson error subtraction). When the data variation can be regarded as a white noise, its variability function is proportional to $t_b^{-1/2}$.

Figure 7.4 shows the variability functions calculated from the 3–10 keV count rate of Swift J2127.4+5654. They have similar shapes, and are rather flat at $t_b < 40$ ks, are almost proportional to $t_b^{-1/2}$ above ~ 40 ks, and drop possibly because of over-subtraction of the Poisson errors. The characteristics are similar to those of solar-mass black holes (Ogawara et al. 1977).

From the characteristic time scale of $t_c \sim 40$ ks, we can estimate the size scale of the corona, via three types of velocities. One is the light speed, c, which gives the size scale of $ct_c \sim 500 r_g$. Another is the sound speed of $\sim 0.3c$ in the corona with $T_e \sim 50$ keV, which gives $\sim 160 r_g$. The other is Keplerian velocity, $v = \sqrt{GM_{BH}/r}$ (§2.1.5). Under a condition of $vt_c = r$, the typical size scale can be obtained as $r \sim 70 r_g$. In the following section, we

examine which size scale can best explain the observational evidence.

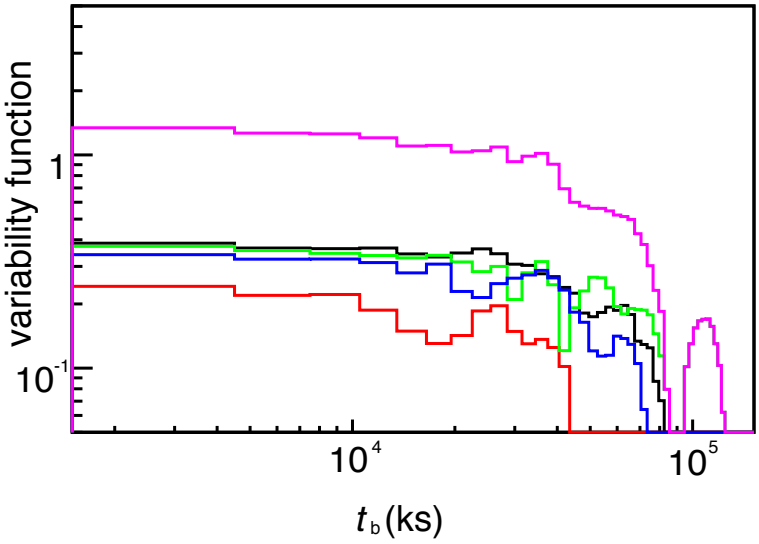

Figure 7.4: Variability functions of the 3–10 keV count rate of Swift J2127.4+5654 in 2012/11/04 (black), 11/05 (red), 11/06 (green), 11/08 (blue), and the sum of them (magenta).

7.2.2 Delays between the soft and hard PLs

From Swift J2127.4+5654, we detected not only the hard PL variations, but also the occasional time delay of the hard PL to the soft PL by $\sim$ 6 ks. We first examine which interpretation in §5.2.1 can explain the observational evidence. Because we have identified the varying hard component in Swift J2127.4+5654 not as a reflection but as the hard PL (§5.1), we can exclude the possibility of a variable reflection. Inverse Compton scattering can explain the time scale of $\sim$ 6 ks by considering photons scattered several times in a corona with the size of $\sim 20 r_{\rm g} = c \times (1.5$ ks). However, it cannot explain appearing and vanishing of the delay, although a delay could be slightly shorter or longer, but should be always seen around 6 ks. Therefore, we are left with the last possibility, that the delay represents time scales of dynamics of accreting materials.

Because the flux variations of each primary PL are considered to be caused by variations of its energy source, the 6 ks delay is regarded as a time interval required for materials to fall from the position near the soft corona to that near the hard corona; the soft corona is 6 ks upstream to the hard corona, like the patchy corona in figure 2.15.

The radial velocity of an accreting material is represented as $gv_{\rm ff}$, where $v_{\rm ff} = \sqrt{GM_{\rm BH}/r}$ is free-fall velocity at the distance of r, and $0 < g \leq 1$ is a numerical factor. In a RIAF, g is close to unity, while g is much smaller with $g < 10^{-3}$ in a standard accretion disk. Figure 7.5 shows the position of the hard PL calculated from the soft corona position and the accreting time of 6 ks, assuming the radial velocity of $gv_{\rm ff}$. The area enclosed by the lines of $g = 0$ and $g = 1$ are physically permitted. Therefore, the distance between the two coronae are estimated as $\lesssim 20r_{\rm g}$.

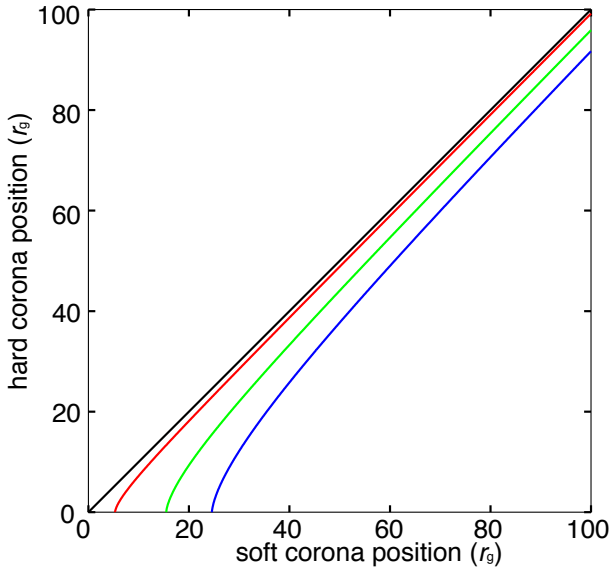

Figure 7.5: The hard corona position calculated from the soft corona position and accreting time of 6 ks, assuming $g = 0$ (black), 0.1 (red), 0.5 (green), and 1 (blue).

Now, we can answer which of the three sizes, namely, $500r_{\rm g}$, $160r_{\rm g}$, and $70r_{\rm g}$ suggested in §7.2.2 is most appropriate as the size of the soft corona. If it were as large as $500r_{\rm g}$ or $160r_{\rm g}$, it would be very difficult to place the two coronae with the suggested separation of $\lesssim 20r_{\rm g}$. Therefore, we conclude that the soft PL has a typical size scale of $70r_{\rm g}$, and its variation time scale is likely to reflect the dynamical time scale.

7.3 A Possible Geometry

Now, we have come to the stage of proposing a possible geometry of the AGN central engine, to explain the overall observational evidence in natural and consistent way. Figure 7.6 shows the proposed geometry, which has been arrived through the following considerations.

- The inner radius is small with $r_{\rm in} = 30$–$100 r_{\rm g}$ in the high-η NLS1s, and considered to be larger in low-η ones. We assume $r_{\rm in} = 60 r_{\rm g}$.
- The emission region of the hard PL is considered to be the RIAF, which is located inside the accretion disk.
- The soft corona is located upstream to the RIAF by $\lesssim 20 r_{\rm g}$, and its size is $\sim 70 r_{\rm g}$.
- The solid angle of view from the soft corona to the disk must be $\sim 2\pi$.

Assuming the location of the soft and hard corona at $70 r_{\rm g}$ and $60 r_{\rm g}$, respectively, the 6 ks delay suggests $g \sim 1.0$ on average (§7.2.2). Such a high g suggests that the two coronae are connected by an optically-thin flow as suggested for Cyg X-1 (Makishima et al. 2008) rather than the underlying accretion disk. In the case of the black hole binary Cyg X-1, it is considered that the accretion disk is covered with a corona, of which covering fraction varies (Makishima et al. 2008). In the same way, the soft corona in an AGN is considered to be optically thin.

The absence of the 6 ks delay in the hard phase also can be explained by the covering corona, which is considered to be highly inhomogeneous to have opening holes. Furthermore, the coronal opening is assumed to vary spontaneously, for some unspecified reasons, even when accretion rate is kept constant. In the softer phase of Swift J2127.4+5654, the corona sufficiently cover the disk to connect the soft and hard coronae, as shown in figure 7.6 (a). In the harder phase, the covering fraction decreases, so that the soft corona cannot reach the hard corona intercepted by the holes, as shown in figure 7.6 (b).

Finally, we discuss the origin of the neutral absorber of the hard PL, which is seen in Swift J2127.4+5654 (§5.1.5, §5.1.6) but not in NGC 4051 (§6.3, §6.4). A candidate for such an absorber would be a dense gas, called failed wind (Murray et al. 1995). When accreting gasses have sufficient energy to escape from the SMBH, they outflow from the AGN. The failed wind is made of gasses that was not energetic enough to escape, and is located near the accretion disk as illustrated in figure 7.6. Numerical simulations support the presence of it (Proga et al. 2000; Proga & Kallman 2004). The gas is considered to be dense enough to provide $N_{\rm H} \sim 8 \times 10^{23}$ cm^{-2} which is required by the data (§5.1.6). The hard primary from the inner region is considered to be strongly absorbed by the failed wind, while the soft one will be able to avoid the absorption as understood from the geometry. The absence of Fe lines in the hard PL informs us about the geometry of the absorber. The absorber is considered not to cover the X-ray sources but to be distributed on the line of sight. When the intensity of Fe Kα line is smaller than 10% of the continuum at 6.4 keV, which is the

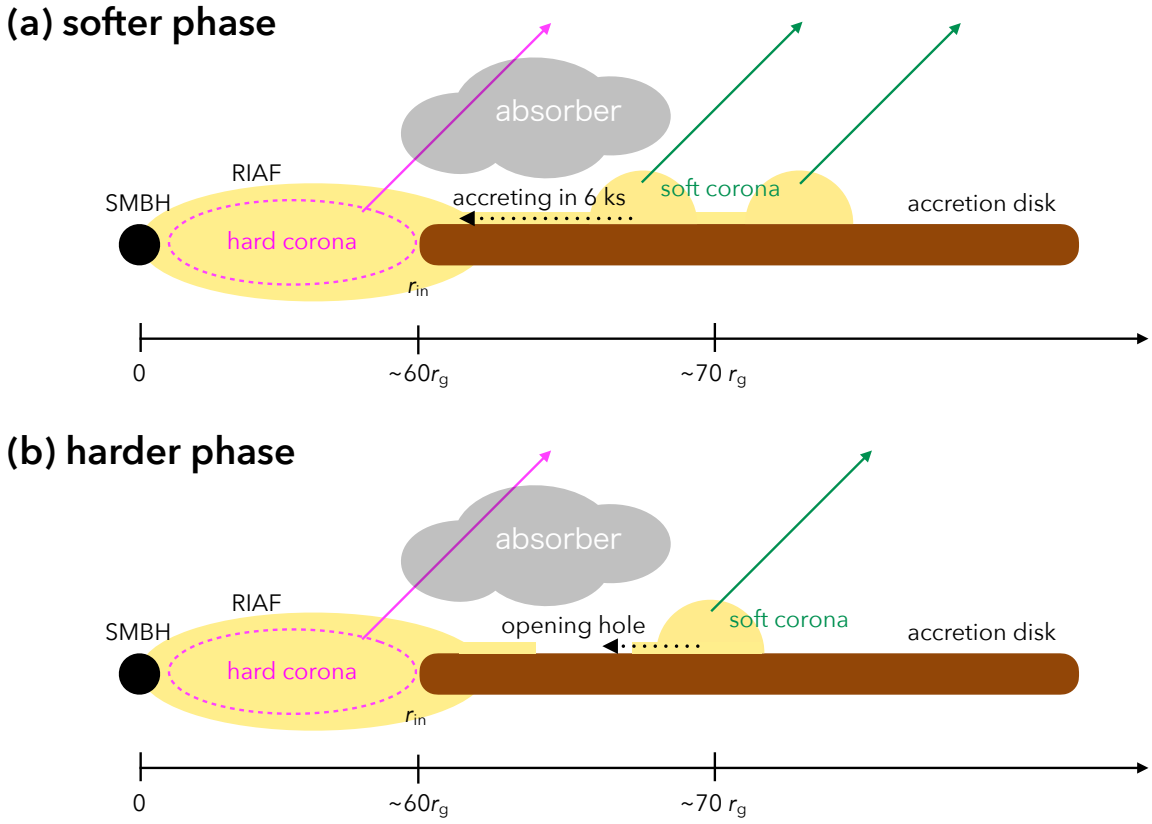

Figure 7.6: A possible geometry of the AGN central engine. (a) When the soft PL is strong. (b) When the soft PL is weak. the two PLs vary independently.

statistical error of the difference spectrum [B] in figure 5.10, the equivalent width is $\sim$ 75 eV. Because such a cold thick matter with the solid angle of 2π makes an Fe Kα line with the equivalent width of $\sim$ 150 eV George & Fabian (1991), the absorber is considered to have the solid angle of $\lesssim 1.0\pi$.

7.4 Implications for the Nature of NLS1s

The present study allow us not only to understand the AGN central engine, but also to address the basic question as to NLS1s: why the broad-line component of their optical emission lines (particularly Hβ) less broadened than those of Seyfert 1s? The origin of the unusually narrow lines has not still understood (Liu et al. 2016).

One simple idea would be to attribute this property to relatively low SMBH mass of NLS1s. However, this idea would not hold, as understood by considering the simplest case of spherically symmetric accretion. Under this condition, the mass accretion rate at a distance r from the SMBH is expressed as $\dot{M} = 4\pi r^2 n v_{\rm ff}$, where n is the gas density. By eliminating n with equation 2.11, and employing the ionization parameter ξ defined there, the equation is rewritten as $\dot{M} = 4\pi v_{\rm ff} L/\xi$. Further using the radiation efficiency $\zeta \equiv L/\dot{M}c^2$ as defined in equation 2.4, we finally obtain

$$v_{\rm ff} = \frac{\xi}{4\pi\zeta c^2}. \tag{7.2}$$

The BLRs of AGNs are considered to have similar ξ, to emit optical emission lines (e.g. Baskin et al. 2014). Therefore, BLRs have a constant velocity independent of $M_{\rm BH}$, as long as ζ and geometry are the same. As a result, the line width of the BLR is not considered to depend on $M_{\rm BH}$. In other words, $r/r_{\rm g}$ keeps constant at $(c/v_{\rm ff})^2$.

Although we assumed a constant ζ above, this parameter enable us to look for an alternative scenario of the narrower width. We hence propose an explanation based on our results of the present thesis related to ζ. In general, NLS1s have higher accretion rates than Seyfert 1s (§2.1.2). When the accretion rate is high, the soft primary with high ζ becomes dominant, while the hard primary, which has a lower ζ (§7.1.3), is faint. From equation 7.2, the high ζ in NLS1s is considered to lead to low $v_{\rm ff}$, and hence narrow line width.

7.5 Future Prospects

In the present thesis, we have constructed a uniform picture of multi-zone Comptonization in AGNs including the high-accreting NLS1s, in which the soft corona covers the accretion disk. Since a similar picture was presented for the black hole binary Cyg X-1 (Makishima et al. 2008), an immediate task would be to compare AGNs and black hole binaries that have comparable η, and discuss them in a unified manner.

How does the soft corona on the accretion disk emerge, and accrete to the SMBH? One possibility would be that the corona is produced by magnetic reconnection (e.g. Di Matteo 1998). Therefore, a future collaboration with researchers specialized in magnetohydrodynamics simulations may be an important step.

The X-ray Astronomy Recovery Mission (XARM), expected to be launched in 2021, will enable spectroscopy with the high energy resolution of 5 eV at 6 keV. It will enable us to discriminate among various Fe-K features, including a narrow Fe-K line, a broad Fe line, Fe-K edge, and Fe absorption lines. Therefore, we can reduce the degeneracy among the

three alternative interpretations of AGN spectra (§1). In addition, XARM can be used to study dynamics (Doppler shifts) of the absorber affecting the hard PL, and examine whether it can be identified with a failed wind (§7.3).

Chapter 8

CONCLUSION

In the present thesis, we observationally investigated X-ray emission from four NLS1s, through timing spectroscopic studies of the wide-band X-ray data, acquired with *NuSTAR* and *Suzaku*. The following results have been obtained.

1. Using the difference spectrum method, the X-ray spectra of the four NLS1s have been successfully decomposed into a highly-variable soft PL with $\Gamma \sim 2.2$, a less-variable hard PL with $\Gamma \sim 1.5$ with significant absorption, and a reflection component accompanied by an Fe K line. The NLS1s, as well as Seyfert 1s, harbor two distinct PLs, of which shapes are similar to those of Seyfert 1s. The two PL components are both considered as primary emission.

2. When the accretion rate increases beyond the Eddington ratio of $\eta \sim 0.1$, the hard-PL luminosity reaches the highest limit of ~ 0.05 times the Eddington limit, and becomes saturated. On the other hand, the soft-PL luminosity increases steeply up to $\eta \sim 0.1$; at $\eta > 0.1$, it becomes to dominate the primary X-ray emission.

3. In NLS1s with the high accretion rates of $\eta \sim 0.4$, the inner disk radius decreases to $r_{\rm in} = (30\text{–}100) r_{\rm g}$, as determined by weak Doppler broadening of Fe-K lines. As a result, the reflection component starts to follow the variation (on ~ 10 ks) of the soft-PL primary, and/or becomes ionized.

4. As in Seyfert 1s, the hard PL of NLS1s is considered to arise via thermal Comptonization from a radiatively inefficient accretion flow (RIAF) region, which is an inflated hot flow inside $r_{\rm in}$. In contrast, the soft PL is likely to arise when the disk photons (usually in ultraviolet range) are Compton scattered by patchy hot coronae just above

and beneath the disk. The mass inflow from these patchy coronae to the RIAF region sometimes produce a delay, by several ksec, of the hard-PL variations behind those of the soft PL.

5. Because NLS1s generally have higher accretion rate, the soft PL, which is the radiatively efficient primary X-ray, is dominant. Therefore, materials in NLS1s are efficiently ionized by the emission, so that their BLR is more distant from the SMBH. As a result, the emission lines from the BLR becomes narrower.

Overall, we have successfully utilized NLS1s to reinforce the new AGN paradigm developed by Noda (2013) and Noda et al. (2011a,b, 2013a,b, 2014), and conversely, obtained a new explanation of NLS1s as radiatively efficient AGNs.

References

Abdo, A. A., Ackermann, M., Agudo, I., et al. 2010, ApJ, 716, 30

Alonso-Herrero, A., Ramos Almeida, C., Mason, R., et al. 2011, ApJ, 736, 82

Antonucci, R. 1993, ARA&A, 31, 473

Antonucci, R. R. J., & Miller, J. S. 1985, ApJ, 297, 621

Awaki, H., Koyama, K., Inoue, H., & Halpern, J. P. 1991, PASJ, 43, 195

Awaki, H., Koyama, K., Kunieda, H., & Tawara, Y. 1990, Nature, 346, 544

Barth, A. J., Boizelle, B. D., Darling, J., et al. 2016, ApJL, 822, L28

Baskin, A., Laor, A., & Stern, J. 2014, MNRAS, 438, 604

Beckmann, V., Soldi, S., Ricci, C., et al. 2009, A&A, 505, 417

Begelman, M. C., Blandford, R. D., & Rees, M. J. 1984, Reviews of Modern Physics, 56, 255

Bentz, M. C., & Katz, S. 2015, PASP, 127, 67

Blandford, R. D., & McKee, C. F. 1982, ApJ, 255, 419

Blandford, R. D., & Znajek, R. L. 1977, MNRAS, 179, 433

Boldt, E. 1987, Phys. Rep., 146, 215

Botte, V., Ciroi, S., Rafanelli, P., & Di Mille, F. 2004, AJ, 127, 3168

Cerruti, M., Ponti, G., Boisson, C., et al. 2011, A&A, 535, A113

Colgate, S. A. 1967, ApJ, 150, 163

Davis, T. A., Bureau, M., Cappellari, M., Sarzi, M., & Blitz, L. 2013, Nature, 494, 328

Denney, K. D., Watson, L. C., Peterson, B. M., et al. 2009, ApJ, 702, 1353

Di Matteo, T. 1998, MNRAS, 299, L15

Dove, J. B., Wilms, J., & Begelman, M. C. 1997, ApJ, 487, 747

Dressler, A., & Richstone, D. O. 1988, ApJ, 324, 701

Fabian, A. C., Iwasawa, K., Reynolds, C. S., & Young, A. J. 2000, PASP, 112, 1145

Ford, H. C., Harms, R. J., Tsvetanov, Z. I., et al. 1994, ApJL, 435, L27

Fukazawa, Y., Mizuno, T., Watanabe, S., et al. 2009, PASJ, 61, S17

García-Burillo, S., Combes, F., Usero, A., et al. 2014, A&A, 567, A125

Gebhardt, K., Bender, R., Bower, G., et al. 2000, ApJL, 539, L13

George, I. M., & Fabian, A. C. 1991, MNRAS, 249, 352

Ghez, A. M., Salim, S., Weinberg, N. N., et al. 2008, ApJ, 689, 1044

Giacchè, S., Gilli, R., & Titarchuk, L. 2014, A&A, 562, A44

Giustini, M., Turner, T. J., Reeves, J. N., et al. 2015, A&A, 577, A8

Haardt, F., Maraschi, L., & Ghisellini, G. 1994, ApJL, 432, L95

Hagino, K., Odaka, H., Done, C., et al. 2016, MNRAS, 461, 3954

Harms, R. J., Ford, H. C., Tsvetanov, Z. I., et al. 1994, ApJL, 435, L35

Harrison, C. 2014, PhD thesis, Durham University

Harrison, F. A., Craig, W. W., Christensen, F. E., et al. 2013, ApJ, 770, 103

Heckman, T. M. 1980, A&A, 87, 152

Holt, S. S., Mushotzky, R. F., Boldt, E. A., et al. 1980, ApJL, 241, L13

Hoyle, F., & Fowler, W. A. 1963, Nature, 197, 533

Huchra, J. P., Vogeley, M. S., & Geller, M. J. 1999, ApJS, 121, 287

Hutchings, J. B., Crampton, D., & Campbell, B. 1984, ApJ, 280, 41

Ishisaki, Y., Maeda, Y., Fujimoto, R., et al. 2007, PASJ, 59, 113

Iyomoto, N., Makishima, K., Matsushita, K., et al. 1998a, ApJ, 503, 168

Iyomoto, N., Makishima, K., Tashiro, M., et al. 1998b, ApJL, 503, L31

Kalberla, P. M. W., Burton, W. B., Hartmann, D., et al. 2005, A&A, 440, 775

Kara, E., Fabian, A. C., Cackett, E. M., et al. 2013, MNRAS, 434, 1129

Kara, E., García, J. A., Lohfink, A., et al. 2017, MNRAS, 468, 3489

Kara, E., Zoghbi, A., Marinucci, A., et al. 2015, MNRAS, 446, 737

Kelley, R. L., Mitsuda, K., Allen, C. A., et al. 2007, PASJ, 59, 77

Khachikyan, É. Y., & Weedman, D. W. 1971, Astrophysics, 7, 231

Kitaguchi, T., Grefenstette, B. W., Harrison, F. A., et al. 2011, in Proc. SPIE, Vol. 8145, Society of Photo-Optical Instrumentation Engineers (SPIE) Conference Series, 814507

Kitaguchi, T., Bhalerao, V., Cook, W. R., et al. 2014, in Proc. SPIE, Vol. 9144, Space Telescopes and Instrumentation 2014: Ultraviolet to Gamma Ray, 91441R

Koyama, K., Awaki, H., Iwasawa, K., & Ward, M. J. 1992, ApJL, 399, L129

Koyama, K., Inoue, H., Tanaka, Y., et al. 1989, PASJ, 41, 731

Koyama, K., Tsunemi, H., Dotani, T., et al. 2007, PASJ, 59, 23

Krolik, J. H., & Begelman, M. C. 1988, ApJ, 329, 702

Laor, A. 1991, ApJ, 376, 90

Liebmann, A. C., Haba, Y., Kunieda, H., et al. 2014, ApJ, 780, 35

Liu, X., Yang, P., Supriyanto, R., & Zhang, Z. 2016, International Journal of Astronomy and Astrophysics, 6, 166

Lobban, A. P., Reeves, J. N., Miller, L., et al. 2011, MNRAS, 414, 1965

Lodato, G., & Bertin, G. 2003, A&A, 398, 517

López-Gonzaga, N., Burtscher, L., Tristram, K. R. W., Meisenheimer, K., & Schartmann, M. 2016, A&A, 591, A47

Lovelace, R. V. E. 1976, Nature, 262, 649

Lusso, E., Comastri, A., Simmons, B. D., et al. 2012, MNRAS, 425, 623

Lynden-Bell, D. 1978, Phys. Scr., 17, 185

Maejima, Y., Makishima, K., Matsuoka, M., et al. 1984, ApJ, 285, 712

Magorrian, J., Tremaine, S., Richstone, D., et al. 1998, AJ, 115, 2285

Makishima, K., Ishida, M., Ohashi, T., et al. 1989, PASJ, 41, 531

Makishima, K., Fujimoto, R., Ishisaki, Y., et al. 1994, PASJ, 46, L77

Makishima, K., Takahashi, H., Yamada, S., et al. 2008, PASJ, 60, 585

Malizia, A., Bassani, L., Bazzano, A., et al. 2012, MNRAS, 426, 1750

Malizia, A., Bassani, L., Bird, A. J., et al. 2008, MNRAS, 389, 1360

Maoz, D., Markowitz, A., Edelson, R., & Nandra, K. 2002, AJ, 124, 1988

Marinucci, A., Matt, G., Kara, E., et al. 2014, MNRAS, 440, 2347

Mathur, S. 2000, MNRAS, 314, L17

Miniutti, G., & Fabian, A. C. 2004, MNRAS, 349, 1435

Miniutti, G., Fabian, A. C., Anabuki, N., et al. 2007, PASJ, 59, 315

Mitsuda, K., Inoue, H., Koyama, K., et al. 1984, PASJ, 36, 741

Mitsuda, K., Bautz, M., Inoue, H., et al. 2007, PASJ, 59, S1

Miyakawa, T., Ebisawa, K., Terashima, Y., et al. 2009, PASJ, 61, 1355

Miyake, K., Noda, H., Yamada, S., Makishima, K., & Nakazawa, K. 2016, PASJ, 68, S28

Miyoshi, M., Moran, J., Herrnstein, J., et al. 1995, Nature, 373, 127

Murray, N., Chiang, J., Grossman, S. A., & Voit, G. M. 1995, ApJ, 451, 498

Nandra, K., O'Neill, P. M., George, I. M., & Reeves, J. N. 2007, MNRAS, 382, 194

Nenkova, M., Ivezić, Ž., & Elitzur, M. 2002, ApJL, 570, L9

Noda, H. 2013, PhD thesis, The University of Tokyo

Noda, H., Makishima, K., Nakazawa, K., et al. 2013a, PASJ, 65, 4

Noda, H., Makishima, K., Nakazawa, K., & Yamada, S. 2013b, ApJ, 771, 100

Noda, H., Makishima, K., Uehara, Y., Yamada, S., & Nakazawa, K. 2011a, PASJ, 63, 449

Noda, H., Makishima, K., Yamada, S., et al. 2014, ApJ, 794, 2

—. 2011b, PASJ, 63, S925

Noda, H., Minezaki, T., Watanabe, M., et al. 2016, ApJ, 828, 78

Oda, M., Gorenstein, P., Gursky, H., et al. 1971, ApJL, 166, L1

Ogawara, Y., Doi, K., Matsuoka, M., Miyamoto, S., & Oda, M. 1977, Nature, 270, 154

Osterbrock, D. E., & Pogge, R. W. 1985, ApJ, 297, 166

Panessa, F., de Rosa, A., Bassani, L., et al. 2011, MNRAS, 417, 2426

Parker, M. L., Fabian, A. C., Matt, G., et al. 2015, MNRAS, 447, 72

Petrov, R. G., Millour, F., Lagarde, S., et al. 2012, in Proc. SPIE, Vol. 8445, Optical and Infrared Interferometry III, 84450W

Proga, D., & Kallman, T. R. 2004, ApJ, 616, 688

Proga, D., Stone, J. M., & Kallman, T. R. 2000, ApJ, 543, 686

Rees, M. J. 1984, ARA&A, 22, 471

Reeves, J., Done, C., Pounds, K., et al. 2008, MNRAS, 385, L108

Reynolds, C. S., & Nowak, M. A. 2003, Phys. Rep., 377, 389

Roche, P. F., Aitken, D. K., Smith, C. H., & Ward, M. J. 1991, MNRAS, 248, 606

Ross, R. R., & Fabian, A. C. 2005, MNRAS, 358, 211

Sazonov, S., Revnivtsev, M., Krivonos, R., Churazov, E., & Sunyaev, R. 2007, A&A, 462, 57

Schmidt, M. 1963, Nature, 197, 1040

Schramm, M., & Silverman, J. D. 2013, ApJ, 767, 13

Serlemitsos, P. J., Soong, Y., Chan, K.-W., et al. 2007, PASJ, 59, S9

Seyfert, C. K. 1943, ApJ, 97, 28

Shakura, N. I., & Sunyaev, R. A. 1973, A&A, 24, 337

—. 1976, MNRAS, 175, 613

Shemmer, O., Romano, P., Bertram, R., et al. 2001, ApJ, 561, 162

Smith, B. J., Kleinmann, S. G., Huchra, J. P., & Low, F. J. 1987, ApJ, 318, 161

Takahashi, T., Abe, K., Endo, M., et al. 2007, PASJ, 59, 35

Tanaka, Y., Nandra, K., Fabian, A. C., et al. 1995, Nature, 375, 659

Tananbaum, H., Gursky, H., Kellogg, E., Giacconi, R., & Jones, C. 1972, ApJL, 177, L5

Taylor, R. D., Uttley, P., & McHardy, I. M. 2003, MNRAS, 342, L31

Terashima, Y., Gallo, L. C., Inoue, H., et al. 2009, PASJ, 61, S299

Titarchuk, L. 1994, ApJ, 434, 570

Tueller, J., Barthelmy, S., Burrows, D., et al. 2005, The Astronomer's Telegram, 669

Unno, W., & Fujimoto, M.-K. 1974, PASJ, 26, 137

Urry, C. M., & Padovani, P. 1995, PASP, 107, 803

van der Marel, R. P. 1994, MNRAS, 270, 271

Verheijen, M. A. W., & Sancisi, R. 2001, A&A, 370, 765

Walton, D. J., Risaliti, G., Harrison, F. A., et al. 2014, ApJ, 788, 76

Woltjer, L. 1959, ApJ, 130, 38

Zdziarski, A. A., Johnson, W. N., & Magdziarz, P. 1996, MNRAS, 283, 193

Zhou, X.-L., & Zhang, S.-N. 2010, ApJL, 713, L11

Życki, P. T., Done, C., & Smith, D. A. 1999, MNRAS, 309, 561

Acknowledgement

First of all, I would like to express my sincere gratitude to Prof. Kazuo Makishima. I decided to learn astrophysics since I looked up to him. He taught me how to consider physically, conduct research steadily, and present research results. His deep knowledge of black holes, detectors, and basic physics was very helpful to my works. I could not complete the thesis without his supports. In my life to come, I will make use of many things I learned from Makishima sensei.

I also appreciate two great senior researchers. Dr. Hirofumi Noda taught me basic knowledge, background, and frontiers of AGN researches. His admirable results had a significant impact on my research, and his cooperation encouraged me to work on the big mystery of AGNs. Dr. Shin'ya Yamada has a wide perspective and knowledge of black hole systems. He gave me a lot of useful advice, which makes me motivated to further consider and discuss from various viewpoints.

I thanks to Lecturer Kazuhiro Nakazawa, who gave me many valuable comments. Especially in experiments of a detector onboard *Hitomi* satellite, he supported and leaded us. Thanks to all labo members, I had a really good and meaningful school life. Discussion with them deepen my understanding, and chatter with them enriched my life. I wish their continued success in their works.

Finally, I want to thank to my father, mother, brothers, and my wife. They support me in any case, and have made me what I am today.